The Astrophysical Journal, 837:96 (51pp), 2017 March 1 https://doi.org/10.3847/1538-4357/aa5cad

The Rotation–activity Correlations in K and M Dwarfs. II. New Constraints on the Dynamo Mechanisms in Late-K and M Dwarfs before and at the Transition to Complete Convection*

E. R. Houdebine[1,2,3], D. J. Mullan[4], B. Bercu[5], F. Paletou[2,3], and M. Gebran[6]
[1] Armagh Observatory, College Hill, BT61 9DG Armagh, UK; eric_houdebine@yahoo.fr
[2] Université de Toulouse, UPS-Observatoire Midi-Pyrénées, IRAP, Toulouse, France
[3] CNRS, Institut de Recherche en Astrophysique et Planétologie, 14 av. E. Belin, F-31400 Toulouse, France
[4] Department of Physics and Astronomy, University of Delaware, Newark, DE 19716, USA; mullan@udel.edu
[5] Université de Bordeaux, Institut de Mathématiques, UMR 5251, 351 cours de la libération, F-33405 Talence cedex, France; Bernard.Bercu@math.u-bordeaux1.fr
[6] Department of Physics & Astronomy, Notre Dame University-Louaize, PO Box 72, Zouk Mikaël, Lebanon
Received 2015 May 4; revised 2017 January 7; accepted 2017 January 25; published 2017 March 7

Abstract

We study the rotation–activity correlations (RACs) in a sample of stars from spectral type dK4 to dM4. We study RACs using chromospheric data and coronal data. We study the Ca II line surface fluxes-$P/\sin i$ RACs. We fit the RACs with linear homoscedastic and heteroscedastic regression models. We find that these RACs differ substantially from one spectral sub-type to another. For dM3 and dM4 stars, we find that the RACs cannot be described by a simple model, but instead that there may exist two distinct RAC behaviors for the low-activity and the high-activity stellar sub-samples, respectively. Although these results are preliminary and will need confirmation, the data suggest that these distinct RACs may be associated with different dynamo regimes. We also study $R'_{\rm HK}$ as a function of the Rossby number R_0. We find (i) for dK4 stars, $R'_{\rm HK}$ as a function of R_0 agrees well with previous results for F-G-K stars and (ii) in dK6, dM2, dM3, and dM4 stars, at a given R_0, the values of $R'_{\rm HK}$ lie at a factor of 3, 10, 20, and 90, respectively, below the F-G-K RAC. Our results suggest a significant decrease in the efficiency of the dynamo mechanism(s) as regards chromospheric heating before and at dM3, i.e., before and at the transition to complete convection. We also show that the ratio of coronal heating to chromospheric heating $L_{\rm X}/L_{\rm HK}$ increases by a factor of 100 between dK4 and dM4 stars.

Key words: stars: activity – stars: chromospheres – stars: coronae – stars: late-type – stars: low-mass – stars: magnetic field

Supporting material: machine-readable tables

1. Introduction

In the present paper, we have two principal goals. First, we present data that have a bearing on the existence of correlations between rotation and activity (RACs) in our sample of stars. Second, we ask if the empirical correlations can be interpreted in the context of stellar dynamo theories (which attempt to predict the properties of the magnetic fields that are generated in a star with a prescribed structure and rotation). The second goal is admittedly a challenging one: the basic mechanisms underlying stellar dynamo theory are being continuously improved as computer resources permit inclusion of more realistic physical effects. Rather than attempting to provide a comprehensive discussion of these complexities, we simplify our discussion by restricting attention to certain broad classes of dynamos. Here, we briefly outline the distinction between these classes. Whatever the source of the magnetic field, the observational consequences of such a field in a star is expected to be the same: dissipation of mechanical energy associated with magnetic processes leads to enhanced emission (relative to what is generated by the photosphere) from the chromosphere (in spectral lines such as Ca II H and K or H_α) and from the corona (in X-ray continuum). In this paper, these enhanced emissions arising from magnetic effects in the stellar atmosphere are considered to be generic indicators of what we refer to as "magnetic activity," or more briefly, "activity." We seek to quantify how (an observational quantity that is associated with) "activity" in low-mass dwarfs is correlated with (an observational quantity that is associated with) "rotation." In order to set the stage for interpreting our result, we first need to define certain terms that are related to dynamo models.

1.1. Three Classes of Dynamo Models

Models of dynamos in the Sun and stars are typically based on "mean-field electrodynamics" (MFE): the fluid flow and the magnetic field are separated into mean ($\langle u\rangle$, $\langle B\rangle$) and turbulent (u', B') components (e.g., Racine et al. 2011). Although the mean values of u' and B' are by definition zero, the mean value of their cross-product does *not* reduce to zero, but instead produces a non-zero turbulent MFE, E. The essence of MFE is to express the (vector) E in terms of the large-scale (vector) magnetic field $\langle B\rangle$ by means of a tensor expansion in the mean field plus its gradients. The leading order term in this expansion $E_i = \alpha_{ij}\langle B_j\rangle$ is called the "α-effect." Parker (1955) first suggested that the α-effect might arise because cyclonic convective turbulence can systematically twist a large-scale magnetic field, and in the process, regenerate a large-scale poloidal field. All of the dynamos we consider here rely on the α-effect, as well as on (at least) one more factor.

* Based on observations available at Observatoire de Haute Provence and the European Southern Observatory databases and on *Hipparcos* parallax measurements.

In order to construct a mean-field dynamo model, $\langle B \rangle$ is written as the sum of poloidal and toroidal components, and $\langle u \rangle$ is assumed to be directed purely in the azimuthal direction ϕ, and to be axisymmetric, i.e., the angular velocity Ω can be a function of r and θ, but not of ϕ. With these assumptions, the induction equation for the time-varying magnetic field can be separated into two equations, one for the poloidal field, the other for the toroidal field. Source terms (S_p, S_t) appear in both equations, and the dominant source terms determine the dynamo class. For the poloidal equation, S_p is a single term, namely, the ϕ component of E, i.e., the α-effect. For the toroidal equation, S_t contains two terms: (i) a spatial gradient of Ω and (ii) a spatial gradient of E.

Three classes of mean-field dynamos are defined as follows: (a) α–Ω dynamo, in which only term (i) is retained in the toroidal equation; (b) α^2 dynamo, in which only term (ii) is retained in the toroidal equation; (c) α^2–Ω dynamo, in which terms (i) and (ii) are both retained in the toroidal equation.

1.2. Stellar Internal Structure as It Relates to Dynamo Activity

Models of dwarf stars of spectral type F, G, K, and early M possess a radiative core and a convective envelope. In such stars, magnetic fields can be generated by an α–Ω dynamo (also referred to as an interface dynamo, or shell dynamo, Parker 1975).[7] The strongest toroidal magnetic fields in these stars are expected to be produced in the vicinity of the interface ("tachocline") between the radiative core and the convective envelope, where the differential rotation is the strongest. In stars that are massive enough to contain such an interface, and where, therefore, the possibility of an "interface dynamo" (ID) exists, data pertaining to enhanced emission from such stars in chromospheric spectral lines and/or in coronal X-rays reveal clearly that there is a strong correlation between rotation and activity indicators (e.g., Pallavicini et al. 1981; Wright et al. 2011), i.e., the Rotation–Activity Correlation (RAC) has a slope with a numerical value that is definitely non-zero.

However, since Limber (1958) derived models of cool main-sequence stars with lower and lower masses, it has been widely believed by stellar evolution modelers that interfaces do not exist in all low-mass stars. An anonymous referee has pointed out that "there has been no definitive evidence validating this theoretical prediction." In principle, asteroseismology of M dwarfs might eventually provide p-mode frequencies with enough precision that (by analogy with helioseismological data) signatures of the interface could be identified. But although theoretical models have been calculated for such stars (see Rodriguez-Lopez et al. 2014), no empirical data on reliable p-mode periods in M dwarfs are yet available. Despite the lack of definitive evidence at the present time, we shall adopt the widely held belief that stars on the main sequence undergo a transition to complete convection (TTCC) at a certain spectral type. According to models, main-sequence stars with masses that are less than a critical value of about 0.30–0.35 $M_\odot$ are completely convective. Such stars should have no tachocline whatsoever on the main-sequence. And yet the empirical evidence shows that stars with masses less than 0.30–0.35 $M_\odot$ also show enhanced emission in chromospheric lines and in X-ray continuum. Since we have attributed such enhanced emission in warmer stars to magnetic activity, then it seems natural also to ascribe the enhanced emissions in completely convective stars to magnetic activity. Such activity must rely on a non-interface type of dynamo, possibly an α^2 dynamo (distributive dynamo; DD), maintained by convective turbulence alone (e.g., Roberts & Stix 1972; Rosner 1980; Chabrier & Kuker 2006; Dobler et al. 2006).

It is important to note that the existence of complete convection in a star does not mean that the star is necessarily completely convective at all stages of its main-sequence phase of evolution. For example, Feiden & Dotter (2013) report that a 0.3 $M_\odot$ model arrives on the main sequence with a radiative zone sandwiched between two convective zones: the models suggest that such a "sandwich" structure exists for several gigayears before the model becomes completely convective (see also Rodriguez-Lopez et al. 2014). However, at lower masses, 0.25 $M_\odot$, stellar models *are* completely convective at all ages (see Rodriguez-Lopez et al. 2014). Thus, when we use the label "completely convective" for stars of masses in the intermediate range (0.25–0.3) $M_\odot$, the label involves not merely a question of the mass of the model, but also of the age of the model. This complication may cause some ambiguity when we attempt to interpret RACs in the vicinity of the TTCC.

For simplicity, it would be convenient if a given star could be assigned to having either an ID or a DD. But we recognize that such a simplified approach cannot be the whole story: in cool stars where an interface exists, the inevitable presence of a deep convective envelope gives rise to the possibility that ID and DD may both be operating (e.g., Brandenburg & Subramanian 2005; Brown et al. 2010).

In order to distinguish between the observational properties of ID and DD, Durney et al. (1993) pointed out some differences between ID and DD. First, the magnetic field created by an ID should depend strongly on rotation whereas the magnetic field created by a DD should not. In terms of the notation to be used in the present paper, this would lead one to expect that in an ID star, the RAC should have a slope that is definitely non-zero, whereas in a DD star, the RAC slope should be essentially zero. Second, although IDs can produce activity cycles in the large-scale field it was not clear (in 1993) how DD could ever give rise to a cycle.

Since 1993, the second feature has been called into question. For example, Stefani & Gerberth (2003) have demonstrated that cyclic behavior is possible in α^2 dynamo models provided that the following condition is satisfied: the α-effect needs to have radial gradients that are sufficiently steep, including changes in the algebraic sign.

Moreover, recent modeling suggests that the third class of dynamo models (α^2–Ω) might be a better description of the solar dynamo (where there is certainly an interface) than an α–Ω dynamo (e.g., Lawson et al. 2015). From the perspective of a change from an α–Ω dynamo to an α^2–Ω dynamo, perhaps in completely convective stars, we might also encounter a change from an α^2 dynamo to an α^2–Ω dynamo. If this happens, then we might find that rather than seeing a zero slope for the RAC in a completely convective star, the inclusion of Ω in the dynamo model could lead to a non-zero RAC slope.

1.3. Observational Evidence for the TTCC?

A long-standing problem has been the search for an observational signature of the putative transition between different types of dynamos at the TTCC. There have been

[7] For a quantitative evaluation of such a dynamo in mid-K to early-M stars with known rotation periods, see Mullan et al. (2015).

several attempts to detect a change in magnetic activity diagnostics (e.g., Mullan & MacDonald 2001) or magnetic field topologies (e.g., Donati et al. 2008; Morin et al. 2008, 2010; Phan-Bao et al. 2009; Stassun et al. 2011) in the vicinity of the TTCC. None of these studies have identified unambiguous and definitive signatures of significant changes in magnetic activity at the TTCC. However, in a recent paper, West et al. (2015) have reported on a study of RACs in two groups of dwarfs: M1–M4 and M5–M8. West et al. (2015) found that the RAC in M1–M4 stars has a somewhat different slope than the RAC in M5–M8 stars (see Section 4 for a more detailed discussion). One interpretation of this behavior is that something changes as regards the dynamo between M4 and M5. We will return to a discussion of this interpretation (as well as an alternative interpretation) in Section 4.

In order to address the TTCC-dynamo-transition topic meaningfully, we first need to identify at what spectral type the TTCC occurs. Limber (1958) states that "in that part of the main sequence where the inner radiative region ... is becoming vanishingly small," the corresponding spectral type is M3V-M4V. Subsequently, Dorman et al. (1989) placed the TTCC at $M \sim 0.25\,M_{\odot}$, which corresponds to the spectral subtype dM4. Even more recently, Chabrier & Baraffe (1997) predict that the TTCC occurs at $M \sim 0.35\,M_{\odot}$, which corresponds to the spectral subtype dM2. Therefore, it appears that the TTCC may lie somewhere in the range between subtypes dM2 and dM4, corresponding to masses of 0.25–0.4 $M_{\odot}$ (Stassun et al. 2011). The theoretical mass limit at the TTCC has been found to shift toward slightly smaller masses if different boundary conditions are used for the stellar models (Mullan et al. 2015). (Even larger shifts of the TTCC toward lower masses were, at one time, proposed by Mullan & MacDonald (2001) if interior magnetic fields were to be as large as 10^{7-8} G. If fields as large as that were to exist inside stars, the definition of a "fully convective star" could become more ambiguous: the onset of complete convection would then depend not only on the mass and age of a star, but would also depend on how strong its magnetic field is. However, we may not in fact need to worry about this ambiguity: Browning et al. (2016) have recently argued that such strong fields would be unstable.

In standard main-sequence models, the radius of a model scales almost linearly with mass: therefore, the TTCC is expected to lie in the radius range of roughly 0.25–0.4 $R_{\odot}$. According to the radius–$T_{\rm eff}$ calibration of Houdebine et al. (2017) this radius range yields an effective temperature range of 3200–3500 K for the TTCC.

In this paper, we examine the topic of a possible dynamo transition at the TTCC using a more extensive and more fine-grained data set than has previously been available for study.

1.4. Dynamos: Unsaturated and Saturated

Empirically, evidence for rotationally driven dynamos in cool stars first emerged when researchers plotted the strength of chromospheric emission versus stellar rotation (e.g., see Kraft 1967, Vaughan et al. 1981, Soderblom 1982, Vogt et al. 1983, Noyes et al. 1984, Marcy & Chen 1992, Patten & Simon 1996, Fekel 1997, Delfosse et al. 1998, Jeffries et al. 2000, Pizzolato et al. 2003, Mohanty & Basri 2003, Browning et al. 2010, Wright et al. 2011, Rebassa-Mansergas et al. 2013, West et al. 2015).

The key signature is the following: emission in chromospheric spectral lines is observed to be stronger in stars with faster rotation speed v_r (or shorter rotation period P; e.g., Vaughan et al. 1981). This is defined as a "RAC." The existence of an RAC is consistent with the expectations that (i) the faster the rotation is, the stronger are the magnetic fields that can be generated (e.g., Mullan et al. 2015), and (ii) stronger fields are associated with stronger chromospheric heating (Skumanich et al. 1975) and with stronger coronal heating (e.g., Mullan 2009). Thus, if chromospheric emission intensity is plotted as a function of P, it is found that over a certain range of periods, the RAC has a clearly *negative* slope.

However, as more data are accumulated, it emerges that the negative slope of the RAC does *not* extend indefinitely to shorter and shorter P. Instead, when P becomes shorter than a certain value P_c, no further increase in emission occurs: for $P \leqslant P_c$, the RAC becomes flat (e.g., Vilhu 1984), with a slope of zero. By definition, in the flattened portion of the RAC, increasing rotation does *not* result in increased chromospheric/coronal emission. For solar type stars, the transition to a flat curve occurs for $P \approx 3$ days. Vilhu suggested the term "saturated" to refer to such conditions. Similarly, Wright et al. (2011) found that the saturation regime occurs at about $R_0 \simeq 0.8$. Reiners et al. (2009) found that saturation occurs at the critical Rossby number $R_0 \simeq 0.1$. We shall compare these values to those we obtain for our stellar samples below. Pizzolato et al. (2003) found that saturation occurs from a period of about ≈2 days in solar type stars to about ≈10 days in M dwarfs. Rebassa-Mansergas et al. (2013) found that stars with $v \sin i \geqslant 5$ km s^{-1} are all in the saturated regime. This yields a rotation period of ≈3 days for stars at the spectral type dM3 (see Paper I). Therefore, we shall consider that saturation occurs for periods of about ≈3 days or $R_0 \simeq 0.5$. Since in our stellar samples we have stars with shorter rotation periods or R_0, we shall consider below that these stars likely lie in the saturated regime.

Vilhu suggested that "saturation" might be due to a complete coverage of the star's surface by magnetic fields. Another explanation of "saturation" was offered by Mullan (1984) in terms of the maximum possible flux of mechanical energy that can be generated by convection. In the present paper, we shall not attempt to identify the physical process that leads to saturation. Instead, we shall adopt a purely empirical approach, and we shall refer to the flat portion of an RAC as "saturated." In the same vein, we shall refer to an RAC with a statistically significant negative slope as "unsaturated." To the extent that an RAC owes its existence to the operation of a dynamo of some kind, we can say that the dynamo reveals itself in two regimes: saturated and unsaturated. The properties of the two different dynamo regimes we find below (see Section 3.8.1) for the low and high-activity sub-samples, respectively, cannot be due to effects of the chromospheric response to non-thermal heating mechanisms. In fact, there does not seem to be any definitive evidence that the influence of a magnetic field in a stellar atmosphere ever attains a saturated level. In support of this claim, we note that the response of stellar chromospheres to non-thermal heating mechanisms is continuous and monotonically increasing from basal chromospheres to flaring chromospheres (e.g., Houdebine 1992; Houdebine & Doyle 1994a, 1994b; Houdebine et al. 1995; Houdebine & Stempels 1997; Houdebine 2009a, 2009b, 2010a, 2010b). Therefore, the two different types of RACs we find below for the low and high-activity stars, respectively, highlight the different properties of the dynamo mechanisms in these two types of stars.

It seems to us that, in order to study the properties of stellar dynamos most profitably, it would be preferable to concentrate as much as possible on stars in the unsaturated regime. The reason for this claim is that, when conditions are saturated, extra factors come into play that may obscure some physical properties that are directly associated with dynamo action. In view of Vilhu's identification of a critical period P_c, it seems that the slowest rotators have the best chance of being in the unsaturated regime. For that reason, we consider it worthwhile to push the spectroscopic measurements of stellar rotation toward the smallest possible values of $v \sin i$ that can be reliably measured.

In general, since slow rotation means less chromospheric heating, we expect that the slowest rotators in our data set will be low-activity stars that are classified as dK and dM (i.e., those that by definition show no emission in the Balmer lines), while the fastest rotators will be highly active stars that are classified as dKe and dMe (i.e., those where, by definition, the Balmer lines have an emission core). In what follows, we shall be especially interested in determining the (negative) slope of the RAC for low-activity stars (e.g., see Figure 13 below).

1.5. Extending our Previous Work

One reason for the present study has emerged from recent work by Houdebine & Mullan (2015; hereafter HM): they found that another diagnostic of magnetic fields, namely, the efficiency of magnetic braking (which manifests itself in the rotational velocity), undergoes a detectable change at spectral sub-type dM3. Basing their analysis on a new data set of precise rotational velocities, HM found that the mean rotation period of M3 stars is abnormally large compared to those of the adjoining spectral types dM2 and dM4. This indicates that the dM3 stars have been slowed down more than the stars in the immediately adjacent sub-types dM2 and dM4. This excess slowing at dM3 may be associated with a change in magnetic properties of the stars at dM3. Specifically, HM suggested that the change might be associated with an earlier report (Mullan et al. 2006) that the lengths of flaring magnetic loops undergo a significant increase at spectral type dM3.

In the present paper, we extend the work of HM in two distinct ways. First, we expand the database of precise rotational properties of K and M dwarfs of various sub-types. Second, we expand and analyze a separate database, which deals with the second physical parameter that enters into the RAC: the radiative properties that are associated with magnetic "activity" in our sample of rotating stars. Our goal here is to use the activity data to construct RACs. Moreover, we quantify the RACs in two different parts of the stellar atmosphere: the chromosphere (using the Ca II lines) and the corona (using L_X). The present study is based on a larger sample of stars, and a finer grid of spectral sub-types, than have been used previously in constructing RACs for K and M stars. Our goal is to explore whether the unusual rotational signature reported by HM at dM3 is accompanied by unusual behavior in the activity indicators of either chromosphere or corona or both, either as regards the intensity of the radiation, or as regards the slopes of the RACs.

A key physical factor, which is known to be well correlated with chromospheric emission and coronal emission, has to do with magnetic fields on the stellar surface (e.g., Skumanich et al. 1975; Schrijver et al. 1989). The existence of RACs may be interpreted as an indication that the surface magnetic field intensities are correlated with the stellar rotation rate. This relationship is to be expected on the basis of standard dynamo theory (e.g., Parker 1979; Krause & Radler 1980; Mullan et al. 2015). However, most of the observational investigations cited above suffer from two inadequacies: (i) they included only a few stars that are rotating slowly enough to be in the unsaturated regime and (ii) the targets included stars that were spread out over a broad range of spectral types. In this paper, we attempt to remedy both of these inadequacies.

1.6. Aspects of the Data Used in the Present Study

In an effort to extend the RACs to slow rotators among late-type dwarfs, we have been reporting, over the past several years, improved spectroscopic measurements of rotational broadening $v \sin i$ in stars of spectral sub-types dK4 (Houdebine 2011a, Paper XVI thereafter), dK6 (Houdebine et al. 2016, Paper I), dM2 (Houdebine 2008, Paper VIII; Houdebine 2010a, Paper XIV), dM3 (HM), and dM4 (Houdebine 2012a, Paper XVII; Paper I).

Combining our (previous) rotational measures with our measures of the Ca II line equivalent widths (EWs), we have already reported RACs for dK4 (Houdebine 2011a, Paper XVI), dM2 (Houdebine 2011b, Paper XV), and dM4 stars (Houdebine 2012b, Paper XVIII), for slow and rapid rotators alike. In those earlier papers, we proposed empirical RACs that included large samples of slow rotators. We found that, for later spectral types, it is crucial to examine a fine grid of spectral sub-types. Specifically, we found that the RACs vary significantly among dK4 –dM4 stars: the RACs were found to have different gradients and different saturation levels (Papers XV, XVIII, and the present study). The previous data, combined with the present study, now provide us with large enough data sets in each spectral sub-type that we can investigate with improved confidence the differences (if any) between the RACs in five different spectral sub-types. In view of the results reported in HM, it is notable that the present study enables us to study the RACs in the vicinity of the TTCC.

When we consider slow rotators, our data confirm that the mean rotation periods of stars in the range dK4–dM4, in general, decrease with decreasing effective temperature (see HM and Paper I). However, we also find that something unusual happens in the rotation rates between dM2 and dM4. The overall trend toward decreasing rotation period as we go from dK4 to dM4 is interrupted at spectral sub-type dM3: at that sub-type, the mean rotation period increases to a local peak, such that the mean rotational period at dM3 is longer than the overall trend between dK4 and dM4 would have predicted (HM). But when we extend our investigation to include fast rotators among the dK4–dM4 stars, we find the following overall trend: the mean rotation period tends to increase slightly from dK4 to dM4. But once again, at dM3, we find an exception: the mean rotation period of fast rotators at dM3 is locally significantly longer than the overall trend would have predicted (HM). HM interpret these abnormally long rotation periods at sub-type dM3 as possibly being associated with the occurrence of increasing coronal loop lengths (previously reported by Mullan et al. 2006 in a study of flare stars). The mean rotation period of the slow rotators is an important constraint on the temporal history of the dynamo mechanisms and magnetic braking mechanisms (HM, Paper I).

1.7. Studying RACs in Various Formats

An important aspect of the present paper is that we wish to investigate the RACs in various formats. In the first place, we construct RACs separately for the chromosphere and the corona. Moreover, we explore correlations between various observations of the "activity" and various aspects of "rotation." As an example, we will examine, for the H and K lines of Ca II, a plot of the quantity R'_{HK} as a function of the Rossby number R_0. We also plot the Ca II surface flux as a function of $P/\sin i$. We use these different formats in an attempt to improve our chances of identifying changes (if any) in the dynamo regime in the vicinity of the TTCC. We shall find that changes near the TTCC are more readily detectable in some RACs than in others. This may explain why the empirical detection of the TTCC has been elusive in the past.

2. Selection of Spectroscopic Data

Stepień (1989, 1993, 1994) has reported that RACs exhibit certain differences at different spectral types. As an extension of this finding, we have found, in previous studies (Paper XVIII, HM) and also in the present study, that it is important in constructing RACs to select samples of stars with $T_{\rm eff}$ values that are confined within a narrow range. There are two principal reasons for this, one related to the choice of an optimal set of photospheric absorption lines, and the second related to our analysis of chromospheric emission lines. As regards the choice of photospheric lines, we have already discussed the first of the above reasons at length in Paper I in the context of optimizing the measurement of rotational velocities at each spectral subtype between dK4 and dM4. In the present paper, we turn now to the second reason.

In the context of chromospheric analysis, it is important to deal with stars with closely similar $T_{\rm eff}$ when we are attempting to quantify the EW of the chromospheric lines (Ca II resonance doublet and H_α) with as much precision as possible. These lines inevitably include some contributions from the background photospheric continuum and from the temperature minimum region (e.g., Cram & Mullan 1979; Houdebine & Doyle 1994c; Houdebine & Stempels 1997; Paper XV). Initially, our samples of stars had been selected for the purpose of chromospheric modeling studies (e.g., Houdebine & Stempels 1997; Houdebine 2009b, Paper XII; Houdebine 2010b, Paper IX) and ,in these studies, the selection of stars with closely similar spectral types was essential in order to develop reliable grids of semi-empirical model chromospheres, each of which would be superposed on a particular photospheric model.

Based on our previous papers, we have found that the most suitable initial selection parameter when we wish to identify a homogeneous sample of K or M dwarfs belonging to a specific sub-type is the (R–I) color: this color is sensitive to $T_{\rm eff}$, but less so to metallicity (e.g., Leggett 1992; Ramirez & Melendez 2005; Mann et al. 2015). Moreover, broad-band colors of high precision are widely available in the literature for many of the cool dwarfs that are of interest to us.

As an example of how we selected data for our RAC studies, we now describe how we gathered the relevant data for a sample of dK6 stars. We selected a sample of 419 late K dwarfs on the basis of (R–I) measurements available in the literature. For example, our sample of dK6 stars contains stars with $(R–I)_C$ (i.e., (R–I) color in the Cousins system) in the range [0.684; 0.816], which also corresponds to $(R–I)_K$ ((R–I) in the Kron system) in the range [0.503; 0.613] according to the transformation formulae of Leggett (1992) (see Leggett 1992 for more information on the Cousins and Kron photometric systems). According to Kenyon & Hartmann (1995), this range of colors is centered on $(R–I)_C = 0.75$, i.e., the spectral type dK7. However, when we compiled and derived effective temperatures (see Paper I) for this sample of late-K dwarfs, we found, on average, higher temperatures than what would be expected from the $(R–I)_C$–$T_{\rm eff}$ tabulation of Kenyon & Hartmann (1995) (see Paper I). Our dK6 stellar sample contains stars that have similar $(R–I)_C$ colors and the same effective temperatures to within ±110 K (see Paper I). We refer to HM for a discussion of corresponding data for our sample of dM3 stars.

The literature provided us with a starting list of a large number (419) of late-K dwarfs. Searching through databases at the European Southern Observatory (ESO) and Observatoire de Haute Provence (OHP), we identified spectra of 112 different stars that are suitable for our purposes. The final list of 105 stars for which the available spectra would allow us to determine reliable rotational data (i.e., $v \sin i$ values) in our sample of late-K dwarfs has already been provided in Paper I. For the present paper, we found spectra that would allow us to make reliable measurements of the EWs of Ca II and H_α for a sub-sample of only 89 late-K dwarfs. It is the combination of reliable rotations (Paper I) and reliable EWs of chromospheric lines that enable us to undertake, in the present paper, the study of the RAC in our sub-sample of dK6 dwarfs.

The spectra that we use for determining the Ca II and H_α EWs in the present study of dK4–dM4 stars came from three different échelle spectrographs; HARPS (High Accuracy Radial velocity Planet Search, ESO), SOPHIE (OHP), and FEROS (The Fiber-fed Extended Range Optical Spectrograph). We included the SOPHIE observations obtained in the high efficiency mode in our sample. The modes in which the spectra were obtained are indicated in Table 1 together with the corresponding signal-to-noise ratio (S/N). For further details of the spectrographs, see HM.

As a second example of how we selected pertinent data for our spectral sub-samples, we consider here briefly our sample of dM3 stars. As described in HM, we started off with a list of 381 dM3 objects based on (R–I) data in the literature. Searching through the same databases as above, we found suitable observations, which allowed us to determine reliable $v \sin i$ values for 86 different dM3 stars. A subsequent search of the available spectra in the above databases allowed us to obtain reliable measurements of the EWs of Ca II and H_α for a sub-sample of only 59 M3 dwarfs for our chromospheric RAC (excluding probable spectroscopic binaries and low $\sin i$ stars).

2.1. Biases in Our Stellar Samples

The stars in our samples include all stars from all observing programs that have been carried out with HARPS and SOPHIE for stars belonging to the following spectral sub-types: dK4, dK6, dM2, and dM3. For dM4 stars, we compiled all measurements of $v \sin i$ available in the literature (see Paper I). For the dK6 and dM3 samples, we also supplemented our own measurements with measurements available in the literature, notably for active stars (see Paper I).

In the HARPS and SOPHIE databases, many of the spectra were obtained in connection with planet-search programs. In such programs, observers tend to avoid stars with high levels of

Table 1
Parameters of our Homoscedastic and Heteroscedastic Regression Models

Homoscedastic Least Square Fits

			$F_{\mathrm{Ca\,II}} = b \times (P/\sin i)^a$			
Spectral Type	a	b	Correlation Coefficient	χ^2	No. Stars	Statistical Significance
dK4+dK4e	-0.756 ± 0.05	$1.57 \pm 0.34\ 10^6$	0.884	0.032	34	>99.9%
dK6+dK6e	-0.81 ± 0.06	$1.95 \pm 0.34\ 10^6$	0.876	0.021	55	>99.9%
dM2+dM2e	-1.481 ± 0.068	$1.89 \pm 0.85\ 10^6$	0.949	0.018	66	>99.9%
dM3+dM3e	-2.08 ± 0.19	$1.52 \pm 1.00\ 10^7$	0.735	0.118	59	>99.9%
dM4+dM4e	-2.526 ± 0.20	$7.94 \pm 2.05\ 10^5$	0.861	0.090	58	>99.9%

			$F_{\mathrm{Ca\,II}} = b \times (P/\sin i)^a$			
Spectral Type	a	b	Correlation Coefficient	χ^2	No. Stars	Statistical Significance
dK4	-0.624 ± 0.11	$9.33 \pm 3.16\ 10^5$	0.744	0.031	30	>99.9%
dK6	-0.520 ± 0.11	$7.94 \pm 2.18\ 10^5$	0.706	0.013	40	>99.9%
dM2	-0.891 ± 0.12	$4.17 \pm 1.15\ 10^5$	0.708	0.013	54	>99.9%
dM3	-0.93 ± 0.22	$3.09 \pm 1.58\ 10^5$	0.516	0.027	50	>99.9%
dM4	-0.91 ± 0.39	$3.80 \pm 1.89\ 10^4$	0.374	0.057	35	96%

			$F_{\mathrm{Ca\,II}} = b \times (P/\sin i)^a$			
Spectral Type	a	b	Correlation Coefficient	χ^2	No. Stars	Statistical Significance
dK4e	-1.880 ± 0.55	$9.55 \pm 5.18\ 10^6$	0.924	0.014	4	99.7%
dK6e	-1.364 ± 0.16	$3.97 \pm 0.74\ 10^6$	0.961	0.006	9	90%
dM2e	-1.819 ± 0.14	$3.40 \pm 0.51\ 10^6$	0.959	0.009	11	>99.9%
dM3e	-1.165 ± 0.52	$2.19 \pm 1.58\ 10^6$	0.675	0.060	8	99.5%
dM3e+Sat.	-0.37 ± 0.11	$3.16 \pm 0.59\ 10^5$	0.704	0.050	16	99.7%
dM4e	-0.960 ± 0.30	$2.30 \pm 0.59\ 10^5$	0.592	0.025	23	92%
dM4e+Sat.	-0.47 ± 0.08	$1.26 \pm 0.08\ 10^5$	0.720	0.020	34	99.9%

			$\mathrm{EW}_{\mathrm{Ca\,II}} = a \times \mathrm{EW}_{\mathrm{H}_\alpha} + b$			
Spectral Type	a	b	Correlation Coefficient	χ^2	No. Stars	Statistical Significance
dM3e	2.90 ± 0.05	1.14 ± 0.125	0.9994	0.023	6	>99.9%
dM4e	1.909 ± 0.18	-1.035 ± 0.58	0.877	2.2	35	>99.9%

			$\mathrm{EW}_{\mathrm{Ca\,II}} = b \times S_{\mathrm{HK}}^a$			
Spectral Type	a	b	Correlation Coefficient	χ^2	No. Stars	Statistical Significance
dM4+dM4e	1.20 ± 0.07	-0.31 ± 0.04	0.970	0.024	22	>99.9%

			$L_{\mathrm{X}} = a \times L_{\mathrm{Ca\,II}} + b$			
Spectral Type	a	b	Correlation Coefficient	χ^2	No. Stars	Statistical Significance
dK4+dK4e	1.54 ± 0.29	-15.34 ± 8.2	0.859	0.17	13	>99.9%
dK6+dK6e	1.57 ± 0.21	-16.1 ± 5.9	0.321	0.11	16	<10%
dM2+dM2e	1.57 ± 0.17	-15.0 ± 4.6	0.878	0.24	28	>99.9%
dM3+dM3e	1.74 ± 0.11	-19.1 ± 3.0	0.952	0.09	28	>99.9%
dM4+dM4e	1.37 ± 0.12	-8.6 ± 3.2	0.882	0.18	42	>99.9%

Heteroscedastic Least Square Fits

			$F_{\mathrm{Ca\,II}} = b \times (P/\sin i)^a$			
Spectral Type	a	b	Correlation Coefficient	χ^2	No. Stars	Statistical Significance
dK4+dK4e	-0.8140 ± 0.059	$1.916 \pm 0.32\ 10^6$	⋯	0.033	34	>99.9%
dK6+dK6e	-1.0469 ± 0.042	$3.402 \pm 0.021\ 10^6$	⋯	0.093	55	>99.9%
dM2+dM2e	-1.5754 ± 0.058	$2.312 \pm 0.276\ 10^6$	⋯	0.028	66	>99.9%
dM3+dM3e	-2.0201 ± 0.11	$1.169 \pm 0.476\ 10^7$	⋯	0.091	59	>99.9%
dM4+dM4e	-2.5644 ± 0.19	$8.38 \pm 2.05\ 10^5$	⋯	0.211	58	>99.9%

			$F_{\mathrm{Ca\,II}} = b \times (P/\sin i)^a$			
Spectral Type	a	b	Correlation Coefficient	χ^2	No. Stars	Statistical Significance
dK4	-0.568 ± 0.084	$7.66 \pm 1.89\ 10^5$	⋯	0.034	30	>99.9%
dK6	-0.531 ± 0.12	$8.23 \pm 2.23\ 10^5$	⋯	0.017	41	>99.9%
dM2	-0.709 ± 0.14	$2.68 \pm 0.77\ 10^5$	⋯	0.046	54	>99.9%
dM3	-0.837 ± 0.20	$2.33 \pm 1.10\ 10^5$	⋯	0.039	50	>99.9%
dM4	-0.825 ± 0.35	$3.08 \pm 1.25\ 10^4$	⋯	1.966	35	96%

Table 1
(Continued)

Spectral Type	$F_{\mathrm{Ca\,II}} = b \times (P/\sin i)^a$ a	b	Correlation Coefficient	χ^2	No. Stars	Statistical Significance
dK4e	-1.877 ± 0.51	$9.73 \pm 5.07\ 10^6$	⋯	0.038	4	99.7%
dK6e	-1.402 ± 0.43	$4.20 \pm 3.52\ 10^6$	⋯	0.023	9	90%
dM2e	-1.793 ± 0.14	$3.28 \pm 0.54\ 10^6$	⋯	0.014	11	>99.9%
dM3e	-1.041 ± 0.58	$1.60 \pm 1.20\ 10^6$	⋯	0.133	8	99.5%
dM4e	-0.951 ± 0.31	$2.27 \pm 0.58\ 10^5$	⋯	0.077	23	92%

magnetic activity. Therefore our spectral samples are likely to be biased in general toward low-activity stars, i.e., stars that are in the unsaturated portions of the RACs. For reasons outlined above (see Section 1.1), we consider this bias to be an advantage in the present study. The biases in our samples may contribute somewhat to the density of the sampling at different parts of the RAC, but this is not expected to cause significant discrepancies as regards the overall RACs. Note that, for the dM4 and dK6 samples, the sampling of the RACs should be more complete as regards the measures of $P/\sin i$ (because we included other measures of $v \sin i$ from the literature, see Paper I).

3. The RACs in Late-K and M Dwarfs

In this section, we first (Section 3.1) evaluate the surface fluxes in the continuum in the vicinity of the Ca II resonance doublet by using our estimates of T_{eff} and also by using the synthetic spectra of de Laverny et al. (2012).

Then we construct the RACs of M and K dwarfs using a variety of approaches: some approaches may facilitate the extraction of information that is more difficult to extract by means of other approaches. In all of the approaches, we plot a quantity related to "activity" as the ordinate, and a quantity related to "rotation" as the abscissa.

Our first approach (Sections 3.2–3.6) specifies the "activity" of a star in terms of the surface fluxes of chromospheric lines. Combining these surface flux results with our results for $P/\sin i$ (Paper I), we construct a set of RACs for M and K dwarfs belonging to various spectral sub-types (see Figures 2, 3, 5, 8, and 12). We first analyze the RAC for K4 and K6 dwarfs. Then we re-visit the RAC in M2 dwarfs that was first investigated in Paper XV. We then analyze the RAC in M3 dwarfs for which $v \sin i$ measures were reported in HM and for which we present new measurements of the chromospheric line EWs here. We also revisit the RAC in M4 dwarfs that was studied in Paper XVIII with the new values of the stellar parameters determined in Paper I. Finally, we compare the RACs for five spectral K and M subtypes, dK4, dK6, dM2, dM3, and dM4, and draw conclusions about the differential variations of the RAC from mid-K dwarfs to M4 dwarfs.

We emphasize that our RACs are plotted as a function of the projected rotation period $P/\sin i$ and not the rotation period P. The average $\sin i$ is 0.6. Then, in order to recover the RACs as a function of P, one must multiply our RACs by a factor of 1.67. The scatter due to variable $\sin i$ is included in our correlations. Nevertheless, we show that one can obtain reasonably good empirical RACs in spite of these uncertainties and the uncertainties on our measures.

In Sections 3.7 and 3.8, we present an overview of the systematic properties of the RACs in all of our sub-types, first as regards the slopes of the RACs (Section 3.7), and then as regards the absolute values of the chromospheric emission levels (Section 3.8).

In Section 3.9, we switch to a different approach to constructing RACs. As regards rotation, we switch to the Rossby number. As regards chromospheric activity, we switch to a quantity that expresses the output power in the H and K lines of Ca II as a fraction of the star's output power (L_{bol}) (Figure 15).

Switching our attention to the corona (Section 3.10), we construct a different type of RAC for our targets, this time referring to conditions in the corona, rather than the chromosphere. The coronal RAC is obtained by plotting $L_{\mathrm{X}}/L_{\mathrm{bol}}$ as a function of the Rossby number (Figure 16). Comparing "activity" in chromosphere and corona (Section 3.11; Figures 17 and 18) can provide information as to how any given M dwarf star partitions its deposition of mechanical energy between chromosphere and corona. To quantify this partition, in Section 3.11 we examine the correlations between L_{X} and L_{HK} (see Figures 17 and 18).

In the final Section 3.12, we summarize the properties of the various RACs that our data have enabled us to construct.

3.1. The Mean Fluxes in the Vicinity of the Ca II Resonance Doublet

In order to evaluate the efficiency of the dynamo mechanism(s) as a function of spectral type in M and K dwarfs, it seems preferable to inter-compare the RACs calibrated in terms of absolute energy fluxes, rather than confining our attention to the values of the EW. (Nevertheless, the EW have proven useful in terms of surface magnetic fields: see Mullan et al. 2015.) In order to convert from EW to energy fluxes, we calculated the surface fluxes in the continuum in the vicinity of the Ca II lines from the theoretical model atmospheres of de Laverny et al. (2012) and Palacios et al. (2010)[8] for $\log(g) = 5.0$, $[\mathrm{M/H}] = 0.0$ and $\alpha = 0.0$. We found that, in M2, M3, and M4 dwarfs, for our observations, the continuum at about 3950 Å represents a good evaluation of the background continuum flux for the Ca II lines. But there are significant discrepancies between the observations and the models of de Laverny et al. (2012). We show a spectrum of a dM2 star (Gl 205) in Figure 1 together with the model of de Laverny et al. (2012) for an effective temperature of 3500 K. We normalized these two spectra at 1 for the continuum flux at 3950 Å. As one can see in this figure, there are large differences in the continuum fluxes at 3910 and 4000 Å between the model and the observation. We believe these differences are due to missing opacities in the models. We also show, in the lower panel of Figure 1, the spectrum of Gl 570A together with the model for an effective temperature of

[8] http://npollux.lupm.univ-montp2.fr/ or ftp://ftp.oca.eu/pub/laverny/DEPOT/AMBRE_Grid_Flux/

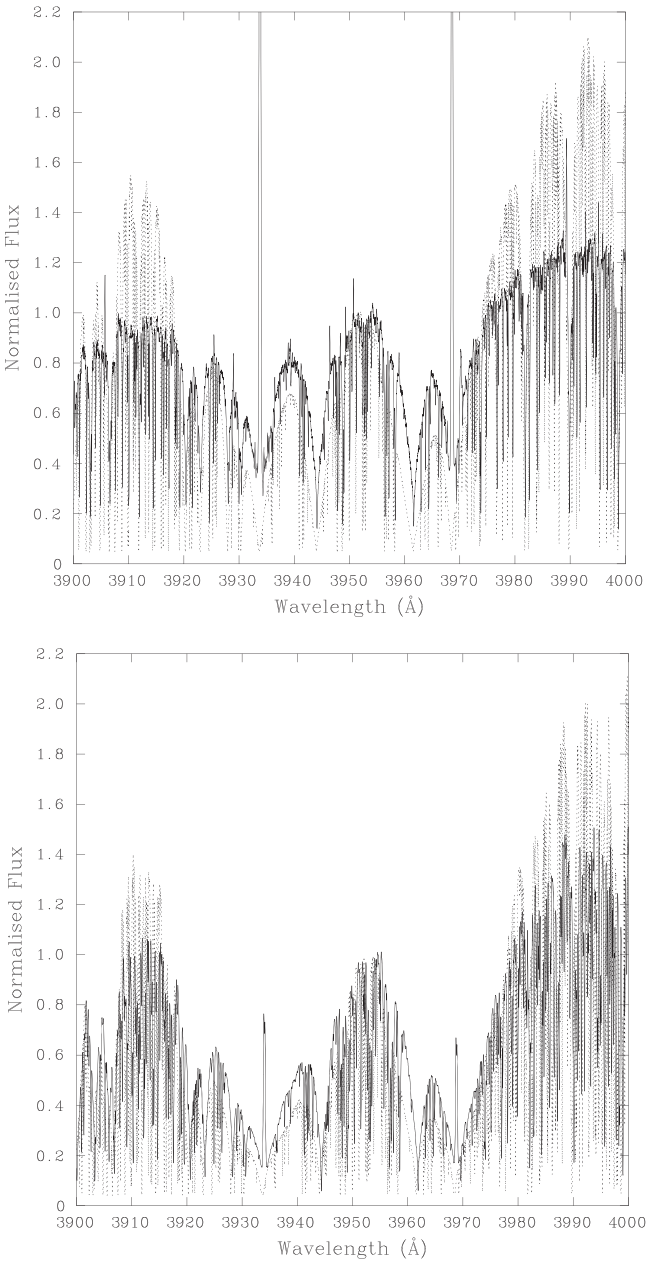

Figure 1. Upper panel: the observed spectrum of Gl 205 (dM2, solid line) together with the theoretical spectrum of de Laverny et al. (2012) for an effective temperature of 3500 K (dotted line). Note substantial disagreements between the observations and the model. Lower panel: the observed spectrum of Gl 570A (dK4, solid line) together with the model for an effective temperature of 4500 K (dotted line). Here again there are significant differences between the model and observations. All the spectra are normalized for the continuum flux at about 3950 Å, i.e., between the H & K line centers.

4500 K. Here again we note important differences: in the spectrum of Gl 570A, the continuum flux at 3950 Å is not a good estimate of the continuum flux in the vicinity of the Ca II lines. In this case, one has to interpolate between the fluxes at 3910 and 4000 Å. Therefore, for our estimates of the theoretical surface fluxes in the vicinity of the Ca II lines for M2, M3, and M4 dwarfs, we took the average of the flux at 3950 Å and the value interpolated between 3910 and 4000 Å. For K6 and K4 dwarfs, we used the value interpolated between 3910 and 4000 Å.

Using this approach, we found that the mean surface fluxes in the continuum in the vicinity of the Ca II lines are: 5.51×10^5, 2.18×10^5, 4.53×10^4, 2.72×10^4, and 1.74×10^4 erg s^{-1} cm^{-2} Å^{-1} for dK4, dK6, dM2, dM3, and dM4 stars, respectively. The strong decline (factor of ∼30) in surface flux in the violet with decreasing $T_{\rm eff}$ from dK4 to dM4 is apparent in these numbers. Using these figures, we are now in a position to examine quantitatively how the surface fluxes in the Ca II lines behave as a function of $P/\sin i$. In the subsequent sections, the Ca II surface fluxes were computed for each star according to its effective temperature. We expect that the models give estimates of the continuum surface fluxes with a precision of the order of 40%. As mentioned above, this figure is far below the factor of ∼30 in the continuum surface fluxes in the violet with decreasing $T_{\rm eff}$ from dK4 to dM4. Therefore, the decline in the Ca II surface fluxes that we observe below (see Figure 14) in the RACs from dK4 to dM4 is highly significant.

3.2. The RAC in K4 Dwarfs

In this subsection, we re-investigate the RACs in our sample of dK4 stars, which were first investigated in Houdebine (2012b, Paper XVIII). We reiterate that the RACs are of fundamental importance in order to constrain an essential parameter of the dynamo mechanism(s): the role played by rotation. In our previous studies (e.g., Papers VII, XIV, XVI, XVII, HM), we reported on our results for $v \sin i$ and $P/\sin i$ for stars of low-activity level (i.e., slow rotators) for the spectral sub-types dK4, dM2, dM3, and dM4. In Paper I, we have reported similar rotational data for dK6 stars. Combining these rotational data with the surface fluxes of chromospheric lines in dK and dM stars provides a unique opportunity to investigate the RACs in a fine-grained sample of M and K dwarfs, which are sub-divided across five closely spaced, but distinct, spectral sub-types.

In Figure 2, we show the RAC that we have obtained for our dK4 stars. In previously published studies of RACs in cool dwarfs, the majority of the results were reported in terms of homoscedastic linear least square fits (LSF) in order to fit their observations. In the present study, we propose different approaches. First, we perform homoscedastic linear and quadratic least square fits to our samples of low+high-activity stars (dK+dKe or dM+dMe). Second, we perform heteroscedastic linear and quadratic least square fits (LSF that account for measurement errors, see the Appendix) to our samples of low+high-activity stars. Third, we also compute homoscedastic and heteroscedastic linear least square fits to two particular sub-sets of our data, namely, stars in which activity is at a low level (dK, dM) and at a high level (dKe, dMe), respectively. We inter-compare the results of these fits for various spectral sub-types in turn in this subsection and in the following subsections. As we shall see, these various fits allow us to account for the complexity of our data sets. In our least-square fits, we do not include in general the suspected low $\sin i$ stars, lower limits, or spectroscopic binaries. However, in the present sub-section, for dK4 stars, it appears that some of the lower limit measurements do correlate with the other measurements of dK4 stars. Therefore, we included some of these measurements in our correlations (we did not include obvious outliers).

The heteroscedastic linear least-squares fit to the data in Figure 2 is shown by the solid line. The equation for the solid

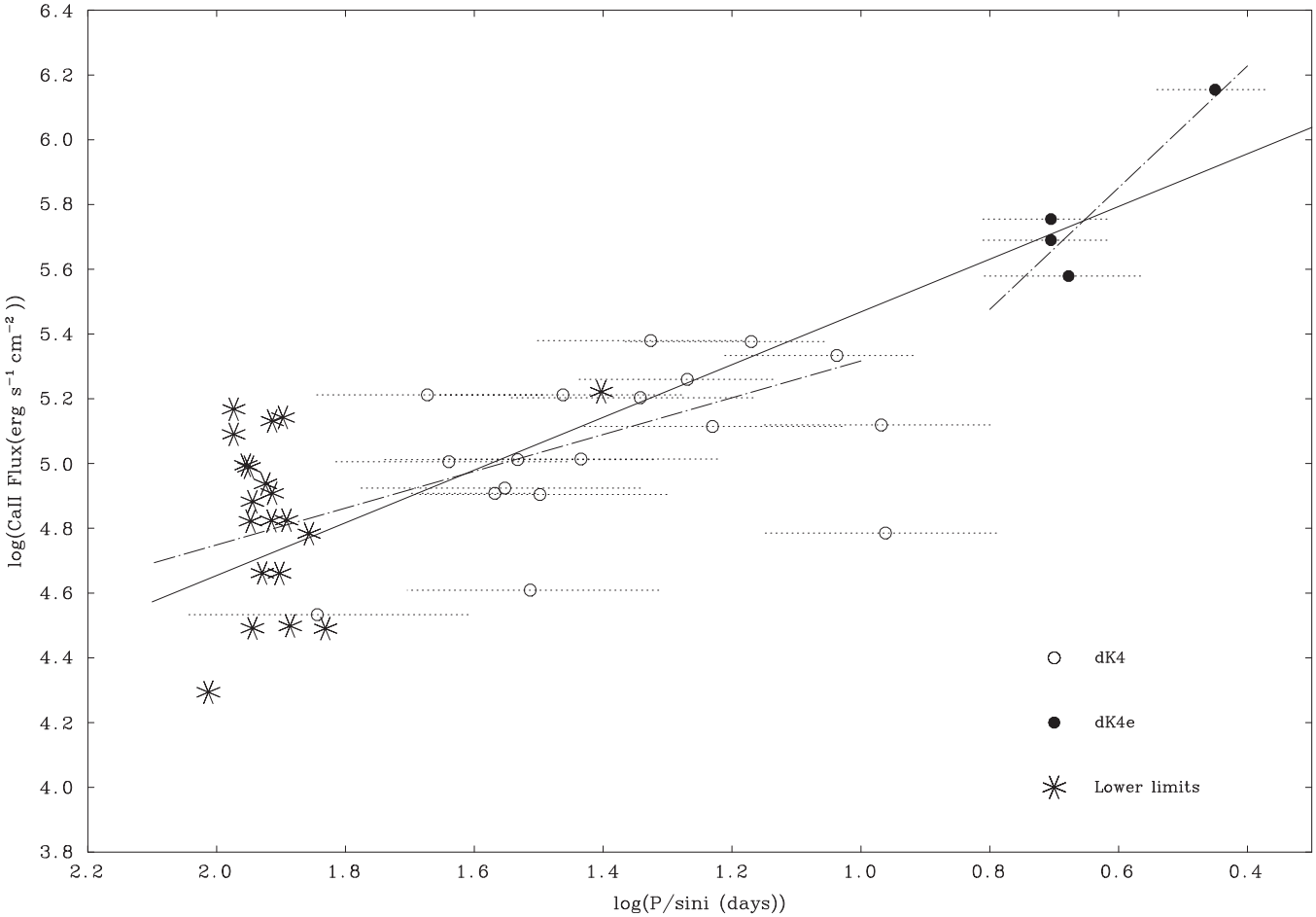

Figure 2. Correlation between the mean surface flux of the Ca II resonance doublet and $\log(P/\sin i)$ for stars with spectral sub-type dK4. We overplot the heteroscedastic linear least square fit (LSF; solid line). We also plot the heteroscedastic linear LSF separately to the low activity and to the high-activity stellar sub-samples (see the two distinct straight dotted-dashed lines).

line in Figure 2 is as follows:

$$F_{\mathrm{Ca\,II}} = 1.916 \pm 0.32 \times 10^6 \times (P/\sin i)^{-0.8140 \pm 0.059}. \quad (1)$$

The χ^2 for the fit in Equation (1) is only 0.033 for our sample of 34 dK4+dK4e stars. The statistical significance of this fit is 99.9% (see Table 1). (Results of all least-squares fits for this and subsequent spectral sub-types can be found in Table 1.)

The homoscedastic linear least-squares fit yields similar results:

$$F_{\mathrm{Ca\,II}} = 1.57 \pm 0.34 \times 10^6 \times (P/\sin i)^{-0.756 \pm 0.05}. \quad (2)$$

The χ^2 for this fit is 0.032 for 34 dK4+dK4e stars. The correlation coefficient for this fit is found to be 0.884 and the statistical significance of the correlation is at least 99.9% (see Table 1). Therefore, these two fits are highly statistically significant. The reason for studying heteroscedastic fits in addition to the homoscedastic fits is that our $P/\sin i$ measurements have large errors and these errors vary as a function of the values of $P/\sin i$ (rapid rotators have smaller errors than slow rotators). The presence of these variable errors may yield heteroscedastic fits that are in some regards different from the homoscedastic fits. We shall see examples of this statement in some of the following subsections.

Two aspects of the fits in Equations (1) and (2) will be referred to in the subsequent discussion. First, the exponent of $P/\sin i$ will be referred to as the "RAC slope" in a plot of $\log(F_{\mathrm{Ca\,II}})$ versus $\log(P/\sin i)$. Systematic changes in the numerical value of the RAC slope will lead us to an important conclusion of the present paper. Second, the numerical coefficient closest to the equals sign is a measure of the absolute level of the chromospheric emission among the stars in the sample. Systematic changes in the numerical value of the coefficient will also be an important conclusion of this paper.

So far in this sub-section, we have done an analysis of all of our dK4 stars, i.e., we have combined both the dK4 stars and the dK4e stars into a single sample. Now we split our sample up into two groups (dK4 in one, dK4e in the second), and analyze each group separately. Specifically, we now apply heteroscedastic and homoscedastic linear LSF to the sub-samples of only the low-activity stars (dK4) and then repeat the exercise including only the high-activity stars (dK4e) (see Table 1). The reason for performing these separate fits is that we found that the linear fits did not reproduce both the low-activity and high-activity sub-samples well; this result led us to wonder if these two samples might contain different dynamo modes. If it turns out that indeed different dynamo modes are at work in slow rotators and fast rotators, then separate analyses of the data sets is warranted. We find that the linear heteroscedastic LSF to the dK4 low-activity stars yield:

$$F_{\mathrm{Ca\,II}} = 7.66 \pm 1.89 \times 10^5 \times (P/\sin i)^{-0.568 \pm 0.084}. \quad (3)$$

The χ^2 for this fit is 0.034 for our sample of 30 dK4 stars and the statistical significance of the correlation is at least 99.9%

(see Table 1). This fit is shown as the straight dotted-dashed line in Figure 2. For the homoscedastic fit, we obtain:

$$F_{\mathrm{Ca\,II}} = 9.33 \pm 3.16 \times 10^5 \times (P/\sin i)^{-0.624\pm0.11}. \quad (4)$$

The χ^2 for this fit is only 0.031 for 30 dK4 stars, the correlation coefficient is 0.744 and the statistical significance is at least 99.9% (see Table 1). Therefore, both of these fits (homo and hetero) are highly statistically significant in spite of the scatter in the data. We note that the differences between the homoscedastic and the heteroscedastic fits fall within the uncertainties of the parameters of the fits.

The linear heteroscedastic LSF to the dK4e high-activity stars yield:

$$F_{\mathrm{Ca\,II}} = 9.73 \pm 5.07 \times 10^6 \times (P/\sin i)^{-1.877\pm0.51}. \quad (5)$$

The χ^2 for this fit is 0.038 for four dK4e stars and the statistical significance is 99.7% (see Table 1). This fit is shown as the upper dotted-dashed straight line in Figure 2. We must admit that our dK4e sample contains only four stars and that therefore the RAC for dK4e stars is not well constrained. However, as we shall see in the subsequent sub-sections, we find that this RAC is consistent with the trend of the high-activity star RACs at other spectral types.

An important feature of our results emerges when we compare Equations (1) and (3), and when we compare Equations (2), (4), and (5): whether we consider homo- or heteroscedastic results, we find that the gradient of the RAC for the low-activity stars alone (−0.57, −0.64) is shallower in magnitude than that of the combined sample of low+high-activity stars (−0.81, −0.76), and that the gradient of the RAC for the high-activity stars alone (−1.88, −1.877) is larger in magnitude than that of the combined sample of low+high-activity stars (−0.81, −0.76). We shall find that this occurs systematically between the low-activity sub-samples and the full samples for all five of our spectral sub-types (see Table 1 and Sections 3.3–3.6). The effect is more pronounced as the spectral type increases (see also Section 3.7). For the high-activity sub-samples, we shall find that the slope is steeper than that of the combined samples for dK4, dK6, and dM2 stars, but that it reverses for the dM3 and dM4 stars (at the TTCC and beyond) and becomes shallower than that of the combined samples. As a consequence, the linear fits to the combined samples of low+high-activity stars tend to overestimate the slope in the low-activity sub-samples, and underestimate the slopes in the high-activity stars sub-samples for dK4, dK6, and dM2 stars. Therefore, we also performed homoscedastic and heteroscedastic quadratic LSF to our samples of low+high-activity stars for our five spectral sub-types. The quadratic fits allow us to reproduce both the shallower gradient of the linear LSF among the low-activity stars as well as the higher fluxes among the high-activity stars. This shows that the quadratic fit may give a better description of the data than the linear fit for the combined samples of low+high-activity stars. However, according to an anonymous referee comment, the quadratic fits may not be significantly different from the results of the linear fits. To argue on this point, the referee performed a simulation on sub-samples of dM and dMe stars with random errors typical of those we find in this study. The referee found also a shallower slope among his sub-sample of slow rotators. Given the evidence at hand, the signatures identified as possible evidences supporting the case for a quadratic fits are most probably due to random errors working in combination with a fairly narrow $\log(P/\sin i)$ domain as compared to those errors. Therefore, although the slopes of the high-activity sub-samples in dK4, dK6, and dM2 are in favor of a quadratic description of the data, we cannot yet conclude that quadratic fits represent definitely a better representation of the full data sets. We can also note that the χ^2s are comparable between linear and quadratic fits. More data will be required to conclude.

As an anonymous referee rightly pointed to, if the data are localized to a domain that is only two to three times as large as a typical error bar, random measurement errors can easily randomize the data and weaken the slope of any true correlation. However, this point is not statistically correct. If the distribution of the errors is Gaussian (which we assume here), then the correct parameter to compare to the RAC domain R is $\delta = \frac{\langle \mathrm{error} \rangle}{\sqrt{n}}$ where n is the number of measures. The value of $\frac{R}{\delta}$ is 17.2 for our low-activity dK4 star sample, which is far larger than the values of 2–3 mentioned above. It appears that $\frac{R}{\delta}$ lies in the range 17–40 for our low-activity and high-activity RACs. The confidence levels of a given LSF depend not only on the mean error but also on the number of measures. Therefore, our LSFs should be established to a fairly high level of confidence, which is confirmed by the high statistical significances that we obtained for our least square fits (see Table 1). Nevertheless, the simulation of the referee is of interest to us. We take this important point into account and we emphasize here the preliminary character of our results. Undoubtedly, these interesting results should be confirmed with additional data, obtained preferably with a higher resolution spectrograph for the slow rotators such as ESPRESSO (ESO, $R = 220{,}000$). Therefore, in the following sub-sections and Section 3.7, our results on the separate fits to the sub-samples of low and high-activity stars should be considered with caution and are only preliminary. They should be confirmed with larger stellar samples.

3.3. The RAC in K6 Dwarfs

In this subsection, we discuss the results for our sample of dK6 stars. For the sake of consistency with previous measurements in this series of papers, and to avoid duplication in describing the method, we refer the reader to Papers VI and XV to see how we evaluate the EW for the Ca II resonance doublet and the H_α line. In Table 2, we list the EW we have obtained for the Ca II resonance doublet and for the H_α line for our dK6 stars.

We note that our dK6 stellar sample contains only one star with H_α definitely in emission (i.e., a dK6e star): Gl 517 (EQ Vir), with the fastest rotation ($v \sin i = 9.77\,\mathrm{km\,s^{-1}}$, $P/\sin i = 3.05$ days, see Paper I). Our dK6 sample also includes one star of "intermediate" activity with H_α neither in emission nor absorption (i.e., a dK6(e) star): Gl 208 (Table 2). As regards EQ Vir, this star has been classified in the literature as a dK5 star. In fact, Gl 517 is a BY Dra star with colors that vary with time (depending on spot coverage).

Our observations contain many slow rotators but very few fast rotators (dKe stars). Therefore, in order to complete our sample and have a better defined RAC for dK6 stars, in Paper I we compiled $v \sin i$ and $P \sin i$ measures from the literature. We found 43 additional $v \sin i$ and $P/\sin i$ measures, which brings our total compilation of measures to 150.

We also retrieved some FEROS spectra from the ESO Archive for Gl 142, Gl 885A, Gl 900, and HIP 113597. The measures of the Ca II EW for these stars are given in Table 2.

Table 2
Equivalent Width (EW, in Units of Å) of the Ca II Resonance Doublet and H_α Line for Our Sample of dK6 Stars

		HARPS			SOPHIE									
Star	No. meas.	Ca II H EW (Å)	Ca II K EW (Å)	H_α EW (Å)	Ca II H EW (Å)	Ca II K EW (Å)	H_α EW (Å)	K/H Ratio	⟨Ca II⟩ EW (Å)	Ca II Flux (10^5 erg s^{-1} cm^{-2})	Ca II Flux[a] (10^5 erg s^{-1} cm^{-2})	No.. meas.	S/N HARPS @5000	S/N SOPHIE @5000
GJ 1056	9	−0.61 ± 0.01	−0.68 ± 0.01	0.643 ± 0.020	⋯	⋯	⋯	1.11	−0.645	2.052		9	151	⋯
GJ 1066	3	−0.91 ± 0.10	−1.01 ± 0.10	0.605 ± 0.020	⋯	⋯	⋯	1.11	−0.96	3.295		3	64	⋯
GJ 1067	3	⋯	⋯	⋯	−0.79 ± 0.10	−1.11 ± 0.10	0.554 ± 0.020	1.41	−0.95	3.171		3	⋯	119
Gl 1177A	⋯	⋯	⋯	⋯	⋯	⋯	⋯	⋯	−1.919	4.525		⋯	⋯	⋯
GJ 1248	3	⋯	⋯	0.239 ± 0.020	⋯	⋯	⋯	⋯	⋯	⋯		3	29	⋯
GJ 1267	1	−1.01 ± 0.15	−1.08 ± 0.15	0.518 ± 0.020	⋯	⋯	⋯	1.07	−1.045	1.755	2.944	1	38	⋯
GJ 1279	2	−0.79 ± 0.01	−0.87 ± 0.01	0.638 ± 0.020	⋯	⋯	⋯	1.10	−0.83	2.849		2	177	⋯
GJ 3072	3	−0.92 ± 0.03	−1.05 ± 0.03	0.585 ± 0.020	⋯	⋯	⋯	1.14	−0.985	1.501	3.132	3	66	⋯
GJ 3411	1	⋯	⋯	⋯	⋯	⋯	⋯	⋯	−1.463	2.598		⋯	⋯	⋯
GJ 3494	3	−0.97 ± 0.05	−1.27 ± 0.05	0.517 ± 0.020	⋯	⋯	⋯	1.31	−1.12	2.905		3	64	⋯
GJ 3551	5	−0.19 ± 0.03	−0.17 ± 0.03	0.659 ± 0.020	⋯	⋯	⋯	0.89	−0.18	0.402	0.553	5	91	⋯
GJ 3996	6	−1.51 ± 0.03	−1.65 ± 0.03	0.498 ± 0.020	⋯	⋯	⋯	1.09	−1.58	2.527	3.491	6	113	⋯
GJ 4140	3	−0.94 ± 0.03	−1.07 ± 0.03	0.544 ± 0.020	⋯	⋯	⋯	1.14	−1.005	1.840	7.050	3	78	⋯
GJ 9250	2	⋯	⋯	⋯	⋯	⋯	⋯	⋯	−1.212	2.934		⋯	⋯	⋯
GJ 9299	8	−0.82 ± 0.01	−0.91 ± 0.01	0.618 ± 0.020	⋯	⋯	⋯	1.11	−0.865	2.033		8	134	⋯
GJ 9667	3	⋯	⋯	⋯	−0.55 ± 0.10	−0.77 ± 0.10	0.625 ± 0.020	1.40	−0.66	1.394	3.788	1	⋯	59HE
GJ 9714	8	−0.76 ± 0.01	−0.84 ± 0.01	0.612 ± 0.020	⋯	⋯	⋯	1.11	−0.80	2.345		8	137	⋯
GJ 9827	2	−0.50 ± 0.03	−0.63 ± 0.03	0.647 ± 0.020	⋯	⋯	⋯	1.26	−0.565	1.217	2.097	2	54	⋯
Gl 14	2	⋯	⋯	⋯	−1.00 ± 0.10	−1.61 ± 0.10	0.534 ± 0.020	1.61	−1.305	2.564	3.747	2	⋯	76
Gl 17.1	10	−0.86 ± 0.03	−0.98 ± 0.03	0.553 ± 0.020	⋯	⋯	⋯	1.14	−0.92	0.601		⋯	⋯	⋯
Gl 40A	2	−0.83 ± 0.10	−0.92 ± 0.10	0.583 ± 0.020	⋯	⋯	⋯	1.11	−0.875	2.228		2	59	⋯
Gl 45	4	−0.68 ± 0.02	−0.79 ± 0.02	0.633 ± 0.020	⋯	⋯	⋯	1.16	−0.735	1.687	3.999	4	100	⋯
Gl 50	4	−0.31 ± 0.03	−0.37 ± 0.03	0.648 ± 0.020	⋯	⋯	⋯	1.19	−0.34	0.761	1.299	4	79	⋯
Gl 52	3	⋯	⋯	⋯	−0.31 ± 0.10	−0.49 ± 0.10	0.597 ± 0.020	1.58	−0.40	0.820	1.555	3	⋯	89
Gl 57	5	−0.32 ± 0.05	−0.35 ± 0.05	0.454 ± 0.020	⋯	⋯	⋯	1.09	−0.335	0.491	16.04	5	100	⋯
Gl 105.5	1	⋯	⋯	⋯	⋯	⋯	0.673 ± 0.020	⋯	−0.437	0.996		1	⋯	65HE
Gl 112.1	1	⋯	⋯	⋯	⋯	⋯	⋯	⋯	−1.627	3.532		⋯	⋯	⋯
Gl 116	1	⋯	⋯	⋯	−0.37 ± 0.05	−0.44 ± 0.05	0.474 ± 0.020	1.19	−0.355	0.586	7.377	6	⋯	124
Gl 142[b]	1	−1.16 ± 0.05	−1.53 ± 0.05	⋯	⋯	⋯	⋯	1.32	−1.345	2.372		⋯	⋯	⋯
Gl 143.1	6	−1.41 ± 0.05	−1.57 ± 0.05	0.534 ± 0.020	⋯	⋯	⋯	1.11	−1.49	2.271	3.319	6	109	⋯
Gl 146	46	−0.67 ± 0.01	−0.75 ± 0.01	0.638 ± 0.020	⋯	⋯	⋯	1.12	−0.71	1.529	2.418	46	279	⋯
Gl 153A	2	⋯	⋯	⋯	−0.43 ± 0.10	−0.56 ± 0.10	0.606 ± 0.020	1.30	−0.495	1.118	3.277	2	⋯	72
Gl 156	2	−0.83 ± 0.10	−0.99 ± 0.10	0.629 ± 0.020	⋯	⋯	⋯	1.19	−0.91	1.635	2.430	2	52	⋯
Gl 162.2	14	−0.88 ± 0.03	−0.96 ± 0.03	0.605 ± 0.020	⋯	⋯	⋯	1.09	−0.92	3.014		14	153	⋯
Gl 182	1	−7.65 ± 0.05	−8.33 ± 0.05	−1.26 ± 0.030	⋯	⋯	⋯	1.09	−7.99	20.3	⋯	1	115[3]	-
Gl 186AB	3	−0.27 ± 0.05	−0.38 ± 0.05	0.651 ± 0.020	⋯	⋯	⋯	1.41	−0.325	0.733	1.486	3	84	⋯
Gl 191	30	−0.10 ± 0.01	−0.12 ± 0.01	0.258 ± 0.020	⋯	⋯	⋯	1.20	−0.11	0.033		⋯	⋯	⋯
Gl 208	19,19	−2.49 ± 0.05	−3.03 ± 0.05	0.082 ± 0.020	−4.29 ± 0.05	-6.24 ± 0.02	−0.291 ± 0.020	1.22	−4.01	4.859	11.52	19, 19	135	309
Gl 221	65	−0.60 ± 0.05	−0.71 ± 0.05	0.637 ± 0.020	⋯	⋯	⋯	1.18	−0.655	1.174	1.953	65	337	⋯
Gl 256	1	⋯	⋯	⋯	⋯	⋯	⋯	⋯	−1.296	4.083		⋯	⋯	⋯
Gl 322	3	⋯	⋯	⋯	−0.96 ± 0.15	−1.42 ± 0.15	0.519 ± 0.020	1.48	−1.19	2.806		3	⋯	83
Gl 369	2	−0.48 ± 0.05	−0.57 ± 0.05	0.417 ± 0.020	⋯	⋯	⋯	1.19	−0.525	0.385		2	45	⋯
Gl 389.1	11	−0.39 ± 0.01	−0.42 ± 0.01	0.668 ± 0.020	⋯	⋯	⋯	1.08	−0.405	0.872	1.284	11	147	⋯
Gl 397	2	⋯	⋯	⋯	⋯	⋯	⋯	⋯	−1.005	1.827		⋯	⋯	⋯
Gl 401	7	−0.55 ± 0.01	−0.72 ± 0.01	0.422 ± 0.020	⋯	⋯	⋯	1.31	−0.635	0.415		7	90	⋯
Gl 412.3	6	−0.39 ± 0.03	−0.47 ± 0.03	0.649 ± 0.020	⋯	⋯	⋯	1.21	−0.43	1.024		6	146	⋯
Gl 414A	8	⋯	⋯	⋯	−0.66 ± 0.10	−0.98 ± 0.10	0.619 ± 0.020	1.48	−0.82	1.646	2.463	8	⋯	302
Gl 416	1	⋯	⋯	⋯	⋯	⋯	⋯	⋯	⋯	⋯		1	⋯	32
Gl 421B	7	−0.69 ± 0.03	−0.75 ± 0.03	0.625 ± 0.020	⋯	⋯	⋯	1.09	−0.72	0.976	7.235	7	116	⋯
Gl 425B	1	−1.55 ± 0.05	−2.00 ± 0.05	0.334 ± 0.020	⋯	⋯	⋯	1.29	−1.775	3.876	4.802	1	67	⋯
Gl 455.1	1	⋯	⋯	⋯	⋯	⋯	⋯	⋯	−5.777	11.28		⋯	⋯	⋯
Gl 466	2	⋯	⋯	⋯	⋯	⋯	⋯	⋯	⋯	⋯		2	⋯	34
Gl 496.1	47	−0.76 ± 0.01	−0.85 ± 0.01	0.653 ± 0.020	⋯	⋯	⋯	1.12	−0.805	1.125	1.497	47	365	⋯
Gl 509.1	1	⋯	⋯	⋯	−1.00 ± 0.10	−1.60 ± 0.10	0.326 ± 0.020	1.60	−1.30	3.219		1	⋯	66

Table 2
(Continued)

Star	No. meas.	HARPS Ca II H EW (Å)	HARPS Ca II K EW (Å)	HARPS H_α EW (Å)	SOPHIE Ca II H EW (Å)	SOPHIE Ca II K EW (Å)	SOPHIE H_α EW (Å)	K/H Ratio	⟨Ca II⟩ EW (Å)	Ca II Flux (10^5 erg s^{-1} cm^{-2})	Ca II Flux[a] (10^5 erg s^{-1} cm^{-2})	No.. meas.	S/N HARPS @5000	S/N SOPHIE @5000
Gl 517	5	−2.36 ± 0.05	−2.83 ± 0.05	−0.611 ± 0.020	⋯	⋯	⋯	1.20	−2.595	11.33		5	141	⋯
Gl 522	3	−0.56 ± 0.05	−0.64 ± 0.05	0.662 ± 0.020	⋯	⋯	⋯	1.14	−0.60	1.292	1.911	3	75	⋯
Gl 524.1	6	−0.94 ± 0.03	−0.99 ± 0.03	0.577 ± 0.020	⋯	⋯	⋯	1.05	−0.965	2.389		6	130	⋯
Gl 542.2	1	⋯	⋯	⋯	⋯	⋯	⋯	⋯	−1.231	3.251		⋯	⋯	⋯
Gl 546	9	⋯	⋯	⋯	−0.75 ± 0.10	−1.10 ± 0.10	0.591 ± 0.020	1.47	−0.925	2.617		9	⋯	146
Gl 558	2	⋯	⋯	⋯	−0.52 ± 0.10	−0.86 ± 0.10	0.572 ± 0.020	1.65	−0.69	1.573	3.379	2	⋯	80
Gl 562	6	⋯	⋯	⋯	−0.83 ± 0.10	−1.19 ± 0.10	0.558 ± 0.020	1.43	−1.01	2.580		6	⋯	126
Gl 571	4	−1.01 ± 0.05	−1.08 ± 0.05	0.525 ± 0.020	⋯	⋯	⋯	1.07	−1.045	2.031	4.872	4	99	⋯
Gl 571.1	4	−1.10 ± 0.03	−1.24 ± 0.03	0.597 ± 0.020	⋯	⋯	⋯	1.13	−1.17	1.813	2.412	4	123	⋯
Gl 583	4	−1.01 ± 0.03	−1.17 ± 0.03	0.579 ± 0.020	⋯	⋯	⋯	1.16	−1.09	2.316	4.884	4	102	⋯
Gl 619	6	⋯	⋯	⋯	−0.38 ± 0.10	−0.66 ± 0.10	0.615 ± 0.020	1.74	−0.52	1.087	1.731	6	⋯	129
Gl 629.1	5	−0.86 ± 0.03	−0.97 ± 0.03	0.612 ± 0.020	⋯	⋯	⋯	1.13	−0.915	1.587	2.191	5	95	⋯
Gl 659B	2	⋯	⋯	⋯	⋯	⋯	⋯	⋯	−1.278	4.195		⋯	⋯	⋯
Gl 673	2	⋯	⋯	⋯	⋯	⋯	⋯	⋯	−1.632	2.541		⋯	⋯	⋯
Gl 707	9	−0.77 ± 0.01	−0.87 ± 0.01	0.617 ± 0.020	⋯	⋯	⋯	1.13	−0.82	1.979		9	226	⋯
Gl 710	3	−1.01 ± 0.10	−1.02 ± 0.10	0.588 ± 0.020	⋯	⋯	⋯	1.01	−1.015	1.760	2.955	3	77	⋯
Gl 726	5	−0.79 ± 0.03	−0.88 ± 0.03	0.574 ± 0.020	⋯	⋯	⋯	1.11	−0.835	2.035		5	126	⋯
Gl 728	18	⋯	⋯	⋯	−0.43 ± 0.10	−0.60 ± 0.10	0.612 ± 0.020	1.40	−0.515	0.850	1.160	18	⋯	373
Gl 747.1	1	⋯	⋯	0.393 ± 0.050	⋯	⋯	⋯	⋯	⋯	⋯		⋯	⋯	⋯
Gl 747.3AB	7	−0.58 ± 0.03	−0.64 ± 0.03	0.624 ± 0.020	⋯	⋯	⋯	1.10	−0.61	1.270	1.753	7	161	⋯
Gl 757	2	−0.76 ± 0.10	−0.86 ± 0.10	0.545 ± 0.020	⋯	⋯	⋯	1.13	−0.81	1.231	3.367	2	49	⋯
Gl 763	15	⋯	⋯	⋯	−1.07 ± 0.05	−1.47 ± 0.05	0.486 ± 0.020	1.37	−1.271	1.910	4.386	1	⋯	91HE
Gl 773	1	⋯	⋯	⋯	⋯	⋯	⋯	⋯	−0.903	2.328		⋯	⋯	⋯
Gl 782	2	−0.84 ± 0.01	−0.92 ± 0.01	0.592 ± 0.020	⋯	⋯	⋯	1.10	−0.88	2.572		15	206	⋯
Gl 786.1	1	⋯	⋯	⋯	−0.73 ± 0.10	−1.11 ± 0.10	0.619 ± 0.020	1.52	−0.92	1.673	2.573	2	⋯	73
Gl 795AB	1	⋯	⋯	⋯	−0.45 ± 0.05	−0.53 ± 0.05	0.600 ± 0.020	1.18	−0.49	0.994	3.030	1	⋯	105HE
Gl 798	22	−0.51 ± 0.01	−0.58 ± 0.01	0.603 ± 0.020	⋯	⋯	⋯	1.14	−0.545	0.979	2.943	22	380	⋯
Gl 801	4	−0.36 ± 0.05	−0.36 ± 0.05	0.667 ± 0.020	⋯	⋯	⋯	1.00	−0.36	0.750	1.151	4	76	⋯
Gl 818	12, 1	−0.43 ± 0.01	−0.50 ± 0.01	0.699 ± 0.020	⋯	⋯	⋯	1.16	−0.465	1.396		12, 1	362	82HE
Gl 820B	1	⋯	⋯	⋯	⋯	⋯	⋯	⋯	−1.63	2.51	⋯	⋯	⋯	⋯
Gl 826.1	1	−1.28 ± 0.10	−1.33 ± 0.10	0.571 ± 0.020	⋯	⋯	⋯	1.04	−1.305	2.937		1	40	⋯
Gl 830	1	⋯	⋯	0.658 ± 0.020	⋯	⋯	⋯	⋯	⋯	⋯	⋯	1	33	⋯
Gl 842	7	−1.18 ± 0.01	−1.31 ± 0.01	0.482 ± 0.020	⋯	⋯	⋯	1.11	−1.245	0.615		7	173	⋯
Gl 847A	14	−0.84 ± 0.05	−0.92 ± 0.05	0.568 ± 0.020	⋯	⋯	⋯	1.10	−0.88	1.489	5.806	14	131	⋯
Gl 855	10	−1.34 ± 0.03	−1.49 ± 0.03	0.491 ± 0.020	⋯	⋯	⋯	1.11	−1.415	0.965		⋯	⋯	⋯
Gl 857.1	2	⋯	⋯	⋯	−0.58 ± 0.05	−0.84 ± 0.05	0.623 ± 0.020	1.45	−0.71	1.897		2	⋯	241HE
Gl 884	1	−1.33 ± 0.10	−1.39 ± 0.10	0.527 ± 0.020	⋯	⋯	⋯	1.05	−1.36	2.033	3.207	1	38	⋯
Gl 885A[b]	2	−2.650 ± 0.05	−2.974 ± 0.05	⋯	⋯	⋯	⋯	1.12	−2.812	5.774		⋯	⋯	⋯
Gl 889A	1	−1.21 ± 0.10	−1.19 ± 0.10	0.547 ± 0.020	⋯	⋯	⋯	0.98	−1.20	2.691	4.954	1	32	⋯
Gl 891	⋯	⋯	⋯	⋯	⋯	⋯	⋯	⋯	−0.876	0.932		⋯	⋯	⋯
Gl 894	3	−0.89 ± 0.05	−0.94 ± 0.05	0.610 ± 0.020	⋯	⋯	⋯	1.06	−0.915	2.048	2.953	3	69	⋯
Gl 895.3	5	−1.17 ± 0.03	−1.29 ± 0.03	0.563 ± 0.020	⋯	⋯	⋯	1.10	−1.23	3.045		5	87	⋯
Gl 898	40	−1.30 ± 0.03	−1.44 ± 0.03	0.516 ± 0.020	⋯	⋯	⋯	1.11	−1.37	3.210		40	343	⋯
Gl 900[b]	1	−3.247 ± 0.03	−3.581 ± 0.03	⋯	−2.44 ± 0.10	−3.29 ± 0.10	0.110 ± 0.020	1.35	−3.414	6.565		1	⋯	71HE
Gl 900	2	⋯	⋯	⋯	⋯	⋯	⋯	⋯	−5.638	10.84		⋯	⋯	⋯
Gl 906	3	⋯	⋯	⋯	−0.66 ± 0.10	−0.91 ± 0.10	0.579 ± 0.020	1.38	−0.785	1.180	2.735	3	⋯	84
Gl 907.1	⋯	⋯	⋯	⋯	⋯	⋯	⋯	⋯	−6.222	8.698		⋯	⋯	⋯
HIP 14593A	3	−0.49 ± 0.03	−0.51 ± 0.03	0.660 ± 0.020	⋯	⋯	⋯	1.04	−0.50	1.179		3	69	⋯
HIP 19410ABC	4	−0.62 ± 0.03	−0.75 ± 0.03	0.670 ± 0.020	⋯	⋯	⋯	1.21	−0.685	1.841		4	70	⋯
HIP 21865	4	−0.34 ± 0.03	−0.42 ± 0.03	0.703 ± 0.020	⋯	⋯	⋯	1.24	−0.38	1.292		4	91	⋯
HIP 40170	1	⋯	⋯	⋯	⋯	⋯	⋯	⋯	−1.31	3.398		⋯	⋯	⋯
HIP 42108AB	2	−0.056 ± 0.01	−0.122 ± 0.01	0.683 ± 0.020	⋯	⋯	⋯	2.18	−0.089	0.169	0.491	2	62	⋯
HIP 42910	1	−0.70 ± 0.15	−0.76 ± 0.15	0.667 ± 0.020	⋯	⋯	⋯	1.09	−0.73	1.945		1	30	⋯
HIP 50773	3	⋯	⋯	⋯	−0.88 ± 0.20	−1.37 ± 0.20	0.535 ± 0.020	1.56	−1.125	1.856	3.116	3	⋯	65

Table 2
(Continued)

Star	No. meas.	HARPS Ca II H EW (Å)	HARPS Ca II K EW (Å)	HARPS H_α EW (Å)	SOPHIE Ca II H EW (Å)	SOPHIE Ca II K EW (Å)	SOPHIE H_α EW (Å)	K/H Ratio	⟨Ca II⟩ EW (Å)	Ca II Flux (10^5 erg s^{-1} cm^{-2})	Ca II Flux[a] (10^5 erg s^{-1} cm^{-2})	No.. meas.	S/N HARPS @5000	S/N SOPHIE @5000
HIP 51073	4	−0.43 ± 0.05	−0.44 ± 0.05	0.655 ± 0.020	⋯	⋯	⋯	1.02	−0.435	1.111		4	79	⋯
HIP 51263	1	>−0.05	>−0.05	0.700 ± 0.020	⋯	⋯	⋯	⋯	⋯	<0.142		⋯	⋯	⋯
HIP 53175	7	⋯	⋯	⋯	−0.54 ± 0.20	−0.71 ± 0.20	0.472 ± 0.020	1.31	−0.625	1.425	1.913	7	⋯	84
HIP 56838	3	−0.35 ± 0.03	−0.40 ± 0.03	0.678 ± 0.020	⋯	⋯	⋯	1.14	−0.375	0.839	1.137	3	82	⋯
HIP 58945	1	⋯	⋯	⋯	−0.84 ± 0.20	−1.24 ± 0.20	0.579 ± 0.020	1.48	−1.04	2.412	4.359	1	⋯	39
HIP 59247	4	⋯	⋯	⋯	⋯	⋯	0.591 ± 0.020	⋯	⋯	⋯		4	⋯	58
HIP 60438A[b]	1	−5.400 ± 0.03	−5.613 ± 0.03	⋯	⋯	⋯	⋯	1.04	−5.507	8.971		⋯	⋯	⋯
HIP 60438B[b]	1	−2.419 ± 0.03	−2.827 ± 0.03	⋯	⋯	⋯	⋯	1.17	−2.623	4.273		⋯	⋯	⋯
HIP 60501	4	⋯	⋯	⋯	⋯	⋯	0.659 ± 0.020	⋯	⋯	⋯		4	⋯	51
HIP 60661	2	⋯	⋯	⋯	−0.39 ± 0.25	−0.76 ± 0.25	0.592 ± 0.020	1.95	−0.575	⋯		⋯	⋯	⋯
HIP 72044	3	⋯	⋯	⋯	−0.39 ± 0.05	−0.57 ± 0.05	0.610 ± 0.020	1.46	−0.48	1.678		3	⋯	102
HIP 76550	3	−0.28 ± 0.05	−0.27 ± 0.05	0.571 ± 0.020	⋯	⋯	⋯	0.96	−0.275	0.448	5.785	3	52	⋯
HIP 78395	11	−0.68 ± 0.03	−0.72 ± 0.03	0.601 ± 0.020	⋯	⋯	⋯	1.06	−0.70	1.991		11	131	⋯
HIP 80083	3	−0.28 ± 0.05	−0.30 ± 0.05	0.624 ± 0.020	⋯	⋯	⋯	1.07	−0.29	1.281		3	50	⋯
HIP 103150	1	−0.46 ± 0.15	−0.58 ± 0.15	0.579 ± 0.020	⋯	⋯	⋯	1.26	−0.52	0.965	2.802	1	33	⋯
HIP 110245	3	−0.82 ± 0.05	−0.93 ± 0.05	0.599 ± 0.020	⋯	⋯	⋯	1.13	−0.875	2.935		3	73	⋯
HIP 110714	2	−0.97 ± 0.05	−1.11 ± 0.05	0.615 ± 0.020	⋯	⋯	⋯	1.14	−1.04	1.786	2.534	2	58	⋯
HIP 113597[b]	2	−2.758 ± 0.03	−3.019 ± 0.03	⋯	⋯	⋯	⋯	1.09	−2.889	5.810		⋯	⋯	⋯
HIP 116011	7	⋯	⋯	⋯	⋯	⋯	0.576 ± 0.020	⋯	⋯	⋯		7	⋯	55

Notes. Results were obtained using spectra from HARPS, SOPHIE, and FEROS. For each star, we give the S/N ratio for the sum of all available spectra, as well as the number of spectra (no. meas.) that we used to compute the equivalent widths.

[a] Corrected or metallicity effects.

[b] FEROS spectra.

(This table is available in machine-readable form.)

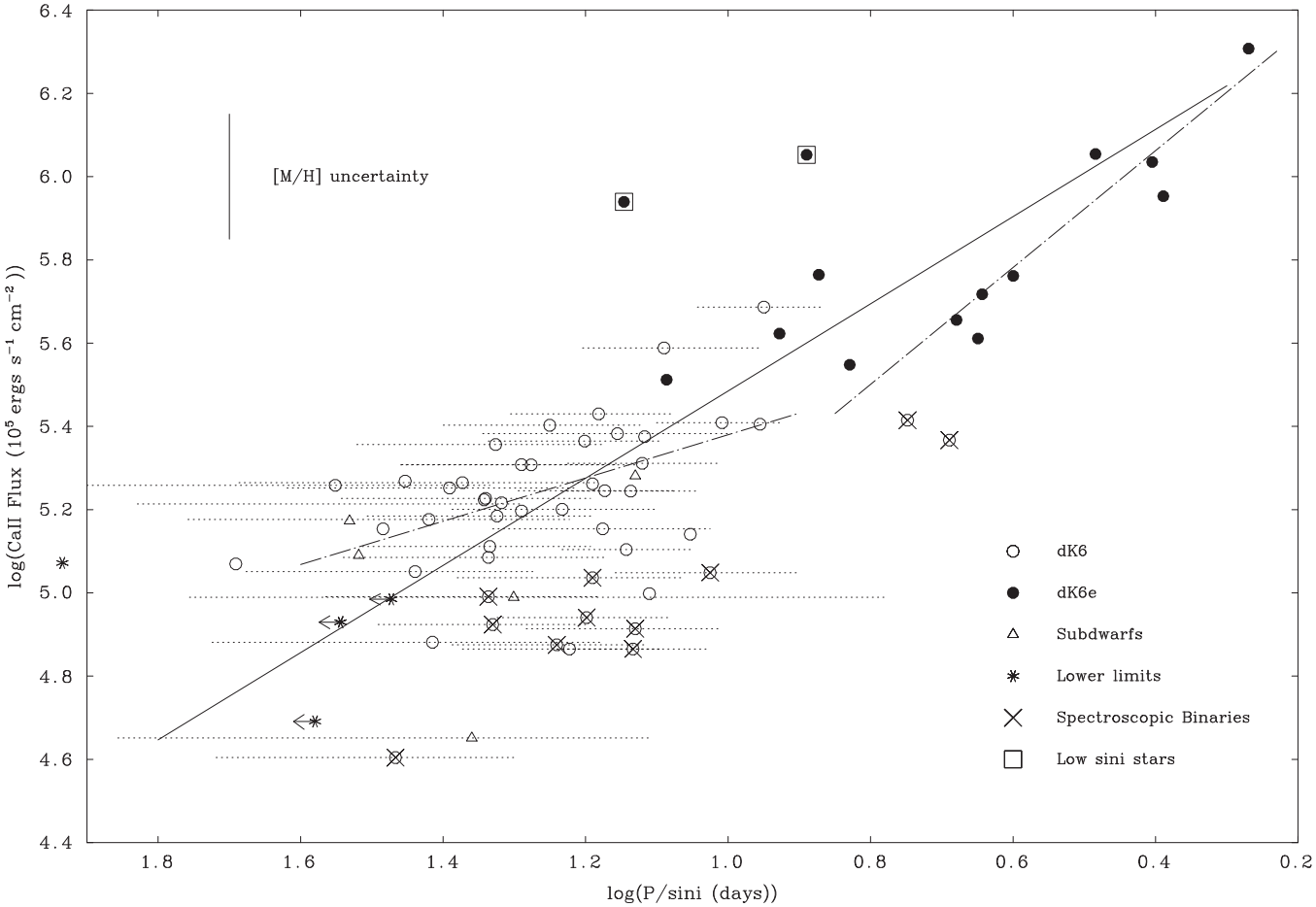

Figure 3. Correlation between the logarithm of the mean surface flux of the Ca II resonance doublet and $\log(P/\sin i)$ for stars with spectral sub-type dK6. We overplot the heteroscedastic linear LSF (solid line). We also plot the heteroscedastic linear LSF to the low-activity stellar sub-sample (dotted-dashed straight line between $\log(P/\sin i) = 1.6$ and 0.9) and the heteroscedastic linear LSF to the high-activity stellar sub-sample (a separate dotted-dashed straight line between $\log(P/\sin i) = 0.85$ and 0.25). In the top left of the figure, we show an estimate of the error on the Ca II mean fluxes due to metallicity effects.

We also searched the literature for other measurements of the Ca II EW. We found only a few measurements of the Ca II EW or flux for our dK6 stars (Marilli et al. 1986; Rutten 1987; Duncan et al. 1991; Browning et al. 2010). These measures are also listed in Table 2.

We saw in Paper XV (see also Section 3.4) that correction for metallicity effects in dM2 stars is essential in order to obtain a good correlation between the Ca II EW and $P/\sin i$. This is due to the fact that the Ca II line formation depends sensitively on the Ca abundance (E. R. Houdebine & P. M. Panagi 2017, in preparation). Here the same applies to dK6 stars and to the Ca II surface fluxes. In Paper I, we compiled [M/H] measures for our dK6 stellar sample and here we computed the Ca II surface fluxes corrected for metallicity effects, assuming a proportionality between [M/H] and Ca II surface fluxes.

In Figure 3, we show the RAC that we have obtained for our dK6 stars. The heteroscedastic linear LSF to the data in Figure 3 is shown by the solid line. One of the stars in our sample, Gl 208 (a dM6(e) star with $P/\sin i = 8.94$ days), is probably also a fast rotator: but its value of $v \sin i$ is too small (and its value of $P/\sin i$ is too large) to be entirely consistent with its observed activity level. It is possible that we are viewing this star close to its rotation axis, i.e., $\sin i$ may be atypically low. We also report on two relatively active stars with a rather slow rotation: Gl 455.1 and Gl 907.1. These stars depart noticeably from the main correlation. We believe that these stars also have low $\sin i$. Most of the other stars follow the solid-line correlation fairly well with a few exceptions: a group of stars that lie below the main correlation and are low-activity fast rotators. One of them is a subdwarf: their internal structure may cause their dynamos to operate differently from those in main-sequence K stars. For the few other stars, similar discrepancies from the RAC have been found in dM2 stars (Paper XV and Section 3.4); they will also be noted among dM3 stars (see Section 3.5). Reiners et al. (2012) also observed a few stars that are discrepant compared to the global trend: Reiners et al. disregarded such objects as being due to measurement errors. However, the repetition with which they appear in our samples, and the fact that they are relatively rapidly rotating, lead us to believe that these low-activity relatively fast rotators may indeed exist as a possibly significant sub-set of late K and M dwarfs. The best explanation we have is that, in a star such as Gl 412.3AB, which exhibits a slight asymmetry when its photospheric spectral lines are subjected to rotational analysis (see Paper I), these stars may be unresolved spectroscopic binaries: as such, they could yield abnormally broadened cross-correlation profiles (see also Gl 186AB in Paper I). Therefore these stars are probably spectroscopic binaries that are unresolved at the time the observations were made. This is quite plausible since binarity is a common characteristic of late-type dwarfs. We label these stars as spectroscopic binaries in Figure 3.

Including the known binaries in our dK6 sample, the number of probable spectroscopic binaries yield a value of 20% binaries in our full sample. This is consistent with the recent finding of Ward-Duong et al. (2015) that binary stars constitute about 25% of their stellar sample for $M_* \sim 0.7\,M_\odot$. In the subsequent subsections, we will see that the proportion of binaries amount to about 28%, 37%, and 48% for our dM2, dM3, and dM4 stellar samples, respectively. Our dM2 and dM3 results are again compatible with the fraction of about 32–37% derived by Ward-Duong et al. (2015) for these stars. For our dM4 sample, our figure of 48% is somewhat larger than the 37% fraction expected at this spectral type. This disagreement may find a simple explanation in the bias in detecting parallaxes for nearby M dwarfs. Indeed, faint single M4 dwarfs are much more difficult to detect than the companions to nearby brighter M and K dwarfs. Therefore, our dM4 sample, which is largely based on parallax surveys of nearby dwarfs, is biased toward the detection of faint companions to nearby brighter M and K dwarfs. This should explain why we have a larger binary fraction for the M4 dwarf sample.

We should like to emphasize four points regarding the plot in Figure 3. (i) Metallicity differences from star to star contribute to the scatter about the dK6 RAC in Figure 3. By analogy, in Paper XV we reported that metallicity differences among dM2 stars are responsible for the greater part of the scatter in the RAC. (ii) Another contribution to the scatter is that our statistics on the Ca II line EW are poor; we have very few measures of the Ca II line EW for most of our dK6 stars compared to what we have for the stars in our dM2 sample, and the Ca II line EW is known to vary with rotation and with the phase of the activity cycle (e.g., Baliunas et al. 1995). However, we have little or no information as to which part of the cycle our observations happened to "catch" for any particular star. (iii) The value of $\sin i$ may vary from 1 to 0 and certainly contributes to the scatter in Figure 3. (iv) The range of effective temperatures in our dK6 sample is somewhat larger than in our samples of dM2, dM3, and dM4 stars (e.g., only ± 70 K in dM3 stars, where $T_{\rm eff}$ ranges from 3210 to 3350 K).

We would like to emphasize, as well, that a few of the active stars in our dK6 stellar sample are candidate young stars that may not yet have contracted to the main sequence (MS). A reliable way to identify the pre-main-sequence (PMS) stars in our samples is the stellar radius: PMS stars that have not yet contracted to the MS have abnormally large radii. We identified three such stars in our dK6 sample: GJ 1177A, GJ 182, and GJ 425B are possible PMS stars (see Paper I). However, Gl 425B is a rather low-activity star. As such, the abnormally large radius for this star is probably due to binarity. Nevertheless, we find that these stars do correlate well with the MS stars. In our M2 sample (see Section 3.4), we have also identified two PMS stars: GJ 1264 and GJ 803. But again, as we shall see, these PMS stars correlate very well with the other MS stars. In our M3 sample, GJ 277A is a possible PMS star. In our M4 sample, GJ 2069A, GJ 3322, GJ 669A, GJ 695B, and GJ 812A are possible PMS stars according to their radii. We emphasize that all these stars do not rotate especially fast. There are many MS stars that rotate faster. These PMS stars are actually expected to spin up as they contract to the MS, and young MS stars are expected to be the fastest rotators (e.g., Barnes 2003; for a theoretical model of this process, see e.g., Figure 2 in Mullan & MacDonald 2003). In fact, that is what we observe in our samples of stars: young MS stars are the fastest rotators (e.g., among our M4 sample, GJ 3631, GJ 3789, GJ 4020B, GJ 4338B, GJ 431, GJ 630.1, GJ 791.2A) with $v \sin i$ in excess of 15 km s^{-1} and up to 56 km s^{-1}.

All of our RACs demonstrate that PMS stars do not stand out as significantly different from the main correlations of the MS stars (see subsequent sections). Numerous previous studies also found similar results (e.g., Mamajek & Hillebrand 2008, Browning et al. 2010, Christian et al. 2011, West et al. 2015). This finding is rather intriguing since PMS stars may have internal structures that differ from those of MS stars: in fact, some PMS stars may even be fully convective. More investigation is required to confirm this result, but so far, in our samples, we found no definitive evidence that PMS stars obey different RACs from those of MS stars.

The heteroscedastic linear LSF to the RAC in Figure 3 gives the following:

$$F_{\rm Ca\,II} = 3.402 \pm 0.021 \times 10^6 \times (P/\sin i)^{-1.047 \pm 0.042}. \quad (6)$$

The parameters of this LSF are given in Table 1. The χ^2 is 0.093 and the statistical significance is 99.9% for 55 dK6 stars. The homoscedastic linear LSF to the same data set gives:

$$F_{\rm Ca\,II} = 1.95 \pm 0.34 \times 10^6 \times (P/\sin i)^{-0.81 \pm 0.06}. \quad (7)$$

The correlation coefficient for this fit is 0.876, the statistical significance is 99.9% and the χ^2 is only 0.021 for 55 dK6 stars. We find, in this case, that the heteroscedastic and the homoscedastic linear fits give slightly different results for the slope and for the flux amplitude: This is due to the fact that high-activity stars (fast rotators) have smaller uncertainties in $P/\sin i$ compared to low-activity stars, and this gives them much higher weights in the least square fit. As a result, the heteroscedastic linear solution fits the high-activity stars better, whereas the homoscedastic linear solution clearly underestimates the fluxes among high-activity stars. Therefore, in this case, the heteroscedastic fit gives more sensible results.

For future reference, we note that, in Figure 3, the correlation in Equation (6) spans the entire range of $P/\sin i$ values for which we have dK6 data. In particular, it is important to notice that the dK6 data exhibit no evidence for a flattening (or "saturation") of the RAC at the shortest periods ($P/\sin i = 1.8$ days). This is consistent with previous results for the earlier spectral type (dK4), which also showed no signs of saturation (see Section 3.2). Neither is there evidence for saturation among dM2 stars (see Figure 5).

Having analyzed the combined samples of slow and fast rotators, we now turn to performing heteroscedastic and homoscedastic linear LSF on the sub-samples of low-activity stars (dK6) and high-activity stars (dK6e) separately. The heteroscedastic linear LSF to the dK6 low-activity stars yields:

$$F_{\rm Ca\,II} = 8.23 \pm 2.23 \times 10^5 \times (P/\sin i)^{-0.531 \pm 0.12}. \quad (8)$$

The χ^2 for this fit is 0.017 and the statistical significance is 99.9% for 41 dK6 stars (see Table 1). This fit is shown as the straight dotted-dashed line in the lower left portion of Figure 3. The homoscedastic linear LSF to this sub-sample gives:

$$F_{\rm Ca\,II} = 1.29 \pm 0.36 \times 10^6 \times (P/\sin i)^{-0.637 \pm 0.11}. \quad (9)$$

The correlation coefficient for this fit is 0.706, the statistical significance is 99.9% and the χ^2 is only 0.014 for 41 dK6 stars. Therefore, these two fits are highly statistically significant at a confidence level greater than 99.9%.

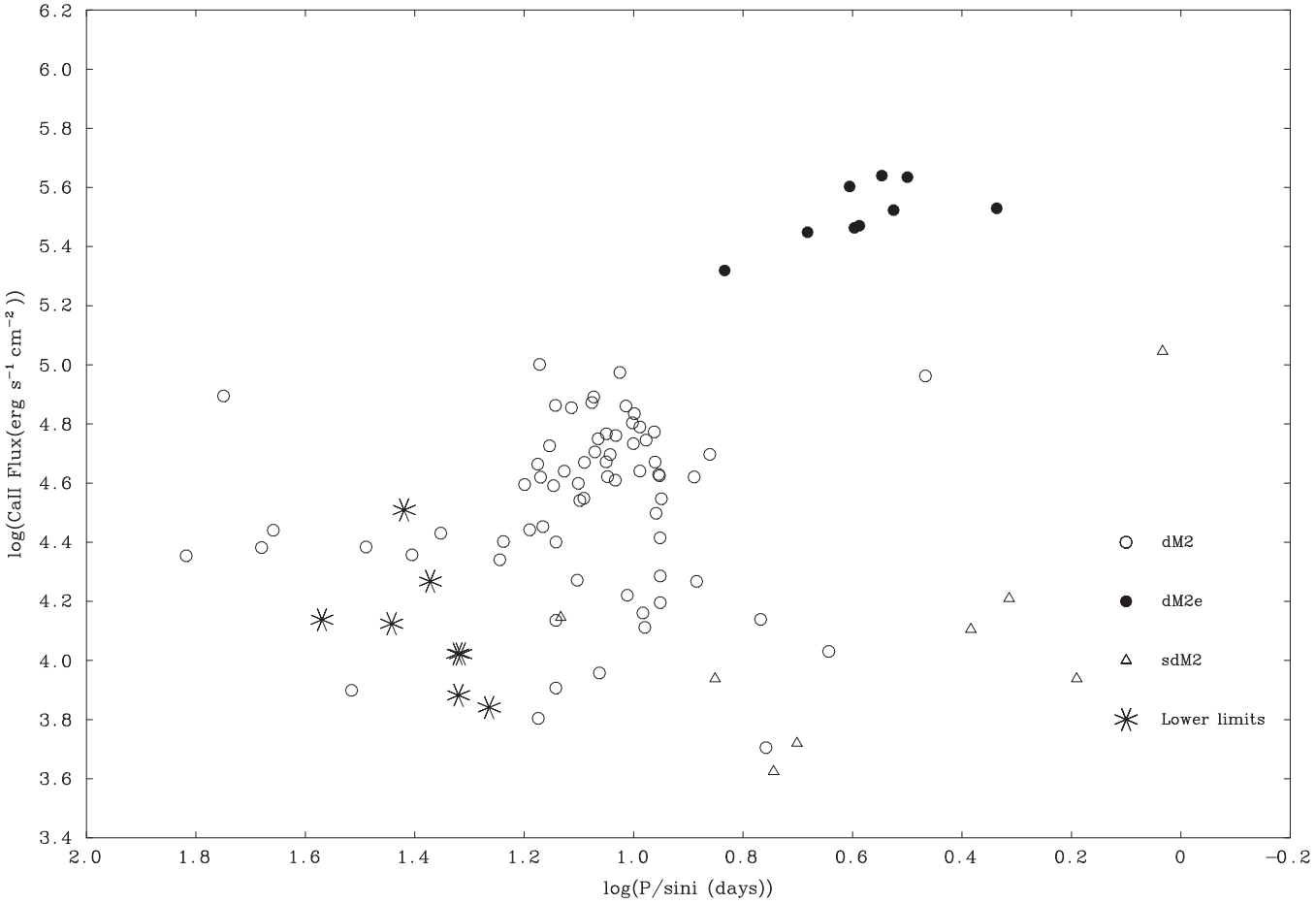

Figure 4. Correlation between the logarithm of the mean surface flux of the Ca II resonance doublet and $\log(P/\sin i)$ for stars with spectral sub-type dM2. In this plot, no corrections have been made for metallicity differences.

We also fitted the high-activity stellar sub-sample. The heteroscedastic linear LSF to the dK6 high-activity stars yields:

$$F_{\mathrm{Ca\,II}} = 4.20 \pm 3.52 \times 10^{6} \times (P/\sin i)^{-1.402 \pm 0.43}. \quad (10)$$

The χ^2 for this fit is 0.023 and the statistical significance is 99.9% for nine dK6e stars (see Table 1). This fit is shown as the straight dotted-dashed line in the upper right portion of Figure 3.

We again find that the gradient of the RAC for the low-activity stars alone (−0.86, −0.64) seems shallower than that of the low+high-activity star sample (−1.05, −0.81) and that the gradient of the RAC for the high-activity stars alone (−1.402, −1.364) seems steeper than that of the low+high-activity star sample (−1.05, −0.81). We find that this difference in RAC steepness occurs systematically between the low-activity sub-samples and the full samples for all five of our spectral sub-types (see Table 1 and Sections 3.4–3.6). The parameter $\frac{R}{\delta}$ is 17.20 for the high-activity star sub-sample and 39.68 for the low-activity star sub-sample. Therefore, the parameter $\delta = \frac{\langle \mathrm{error} \rangle}{\sqrt{n}}$, which is a normalized estimate of the mean error on the measurements, is much smaller than the period domains of the RACs in both cases. Hence, these LSFs should be relatively well established, which corresponds to the high statistical significances we obtain (Table 1). However, we consider these results as still preliminary because the domains of the RACs are relatively small compared to the typical uncertainties on individual measures.

If this difference between the RACs of the low and high-activity sub-samples is confirmed, this may represent a discovery of interest. Indeed, to the extent that the slope of an RAC is related in some way to an underlying dynamo process, the difference that we found between the slopes of the low and high-activity sub-samples suggests that there may exist two different dynamo regimes for these two sub-samples of stars. We find that this difference between low and high-activity regimes persists for all our samples of stars with different spectral sub-types. However, we observe a difference for stars that are more massive than the TTCC and stars that are less massive than the TTCC. For the former, the slope among high-activity stars is steeper than the slope among the low +high-activity stars, whereas for the latter, we find that the slope among high-activity stars is shallower than the slope among the low+high-activity stars. This preliminary result could be of interest for the dynamo mechanisms. More data with a higher resolution spectrograph will be needed to confirm these results.

3.4. The RAC in M2 Dwarfs

We have re-investigated the RAC in the sample of dM2 stars of Paper XV. We have given the new stellar parameters and new $P/\sin i$ values in Paper I. We show the raw data in

Table 3
Values of $v \sin i$, $P/\sin i$ as well as [M/H] from Paper I for Our dM2 Stars

Star	$v \sin i$ (km s−1)	$P/\sin i$ (days)	[M/H] (dex)	Ca II EW (Å)	F_{HK} (10^4 erg s^{-1} cm−2)	F_{HK}[a] (10^4 erg s^{-1} cm−2)
GJ 1010A	⋯	⋯	−0.098	−0.605	2.621	10.555
GJ 1062	9.8	1.92−0.53+0.65	−0.584	⋯	⋯	⋯
GJ 1114	3.8	5.73−1.50+2.07	−0.339	−0.117	0.507	0.664
GJ 1264	6.46	6.82−1.51+2.06	+0.378	−4.45	20.85	8.732
GJ 2085	2.46	10.80−3.23+5.31	+0.000	−0.77	4.071	4.071
GJ 3084	3.16	9.74−4.07+5.98	+0.023	−0.841	4.373	4.147
GJ 3098	2.60	8.97−2.49+3.98	−0.200	−0.86	4.215	6.680
GJ 3207	⋯	⋯	−0.346	−0.19	0.801	1.777
GJ 3340	2.67	9.00−2.91+4.59	−0.048	−0.83	4.256	4.753
GJ 3215	⋯	⋯	−0.314	−0.45	1.950	4.018
GJ 3440	2.71	8.95−3.56+5.59	−0.165	−0.6	2.599	3.800
GJ 3759	2.71	9.10−2.52+3.95	−0.121	−0.645	3.148	4.159
GJ 3778	1.72	13.86−6.49+13.4	+0.002	−0.635	2.515	2.503
GJ 3915	1.88	22.51−12.4+24.0	+0.413	−0.60	2.694	1.041
GJ 4155	⋯	⋯	−0.231	−0.755	3.005	5.115
GJ 9381	2.19	14.01−4.81+8.44	+0.100	−0.90	3.899	3.097
GL 2	2.76	9.74−2.48+3.85	−0.018	−1.316	6.166	6.427
Gl 15A	1.43	13.87−4.92+12.0	−0.386	−0.303	1.366	3.322
Gl 16	2.34	11.23−3.27+5.53	−0.105	−1.084	4.696	5.980
GL 27.1	2.63	10.01−3.03+4.83	−0.016	−1.080	5.413	5.616
Gl 29.1A	10.6	3.16−0.64+0.77	+0.101	−9.69	43.12	34.17
Gl 29.1B	9.5	3.52−0.74+0.91	+0.101	−9.81	43.65	34.59
Gl 49	2.49	11.83−3.13+5.12	+0.026	−1.797	7.785	7.333
Gl 63	<1	>20.90	−0.309	−0.159	0.762	1.552
Gl 87	3.99	5.86−1.24+1.68	−0.027	−0.294	1.377	1.465
Gl 91	1.68	15.82−5.34+11.3	−0.090	−0.968	3.938	4.845
GL 114.1A	1.82	12.68−4.11+8.14	−0.242	−0.466	1.868	3.261
Gl 130	1.27	13.59−5.98+16.7	−0.766	−0.332	1.399	8.162
Gl 133	<1	>20.70	−0.466	−0.28	1.051	3.073
Gl 134	2.53	13.90−3.93+6.37	+0.128	−1.596	7.290	5.429
Gl 140AB	9.4	2.93−0.74+0.92	−0.002	−2.175	9.167	9.209
Gl 150.1B	3.7	7.26−1.74+2.42	−0.084	−1.063	4.980	6.043
Gl 153B	1.4	20.97−8.24+20.6	+0.017	>−0.25	<1.054	<1.014
Gl 155.1	2.93	7.67−2.05+3.10	+0.175	−0.355	1.851	1.237
Gl 162	2.35	11.61−3.48+5.86	+0.019	−1.115	5.621	5.380
Gl 173	2.35	10.27−2.91+4.91	−0.225	−0.430	1.661	2.788
Gl 191	9.15	1.55−0.26+0.33	−1.024	−0.164	0.867	9.163
Gl 205	2.73	11.92−2.94+4.59	+0.101	−1.555	7.453	5.907
Gl 212	1.98	14.85−4.55+8.51	+0.067	−1.872	10.03	8.596
Gl 218	1.66	15.49−5.21+11.1	−0.099	−0.643	2.767	3.475
Gl 229	2.63	11.22−2.80+4.46	+0.060	−1.124	5.845	5.091
Gl 250B	⋯	⋯	−0.247	−0.400	1.294	2.285
Gl 275.1	2.7	13.87−4.14+6.51	+0.172	−0.16	0.807	0.543
Gl 289	<1	>18.37	−0.741	−0.16	0.693	3.817
Gl 330	3.05	9.62−2.57+3.82	+0.023	−0.302	1.447	1.372
Gl 361	1.95	12.54−3.90+7.37	−0.212	−0.926	3.476	5.663
Gl 366	<1	>27.69	−0.014	−0.284	1.331	1.375
Gl 378	2.25	17.30−5.20+8.99	+0.096	−0.755	2.524	2.023
Gl 382	2.9	9.49−2.37+3.60	−0.059	−1.398	5.563	6.372
Gl 390	2.46	10.78−2.97+4.89	−0.030	−1.231	5.767	6.179
Gl 411	0.61	32.77−11.9+30.8	−0.442	−0.199	0.792	2.191
Gl 412A	1.6	11.55−3.82+8.40	−0.435	−0.180	0.907	2.469
Gl 430.1	0.46	65.7−28.3+108	+0.089	−0.43	2.261	1.842
Gl 433	<1	>23.54	−0.199	−0.439	1.850	2.925
Gl 450	2.47	9.14−2.41+3.96	−0.247	−1.054	4.690	8.283
Gl 477	1.95	14.79−5.07+9.57	−0.057	−1.063	4.168	4.753
Gl 490A	8.4	3.87−0.91+1.15	+0.078	−6.03	29.55	24.69
Gl 494AB	9.75	2.17-0.39+0.47	−0.339	−7.222	33.84	73.86
Gl 507.1	2.32	13.39−3.83+6.49	+0.065	−1.036	4.367	3.760
Gl 508.2	1.78	15.01−5.01+10.1	−0.002	⋯	⋯	⋯
Gl 510	2.49	10.33−3.02+4.93	−0.162	−1.77	7.252	10.53
Gl 514	2.07	12.62−3.63+6.59	−0.030	−0.788	3.972	4.256
Gl 521	0.85	30.84−9.69+18.7	−0.017	−0.505	2.420	2.517

Table 3
(Continued)

Star	$v \sin i$ (km s−1)	$P/\sin i$ (days)	[M/H] (dex)	Ca II EW (Å)	F_{HK} (10^4 erg s^{-1} cm−2)	F_{HK}[a] (10^4 erg s^{-1} cm−2)
Gl 526	1.00	25.41−6.99+12.1	−0.086	−0.498	2.275	2.773
Gl 536	<1	>26.27	−0.032	−0.689	3.228	3.475
Gl 537AB	3.6	7.11−1.82+2.55	−0.046	…	…	…
Gl 540	2.09	14.97−4.52+8.16	+0.073	−0.915	4.613	3.899
Gl 552	0.58	45.55−17.9+49.1	−0.100	−0.734	2.756	3.470
Gl 563.2A	2.24	2.06−0.72+1.24	−1.742	−0.355	1.621	89.49
Gl 563.2B	1.82	2.42−0.93+1.85	−1.754	−0.33	1.274	72.31
Gl 618.4	1.45	17.56−7.21+17.4	−0.119	−0.515	2.191	2.822
Gl 634	<0.6	>37.12	−0.303	−0.345	1.373	2.758
Gl 637	2.19	8.94−2.68+4.71	−0.415	−0.33	1.569	4.080
Gl 645	2.80	7.75−2.64+4.09	−0.257	−0.91	4.174	7.543
Gl 649	2.27	11.77−3.29+5.65	−0.020	−1.036	5.077	5.316
Gl 654AB	5.7	4.40−1.02+1.46	−0.090	−0.262	1.073	1.320
Gl 672.1	2.99	8.70−2.75+4.13	−0.086	…	…	…
Gl 686	2.49	8.94−2.35+3.85	−0.245	−0.412	1.930	3.393
Gl 701	1.6	14.65−4.91+10.8	−0.169	−0.592	2.837	4.187
Gl 724	2.97	9.17−2.37+3.58	−0.005	−1.21	5.930	5.999
Gl 737B	…	…	+0.134	−1.79	8.685	6.379
Gl 745A	3.0	5.03−1.25+1.89	−1.03	−0.136	0.525	5.625
Gl 745B	2.8	5.55−1.44+2.22	−1.07	−0.109	0.421	4.946
Gl 767A	2.9	12.30−3.29+5.01	+0.126	−1.08	4.679	3.501
Gl 781	12.7	1.08−0.22+0.25	−1.10	−2.136	11.11	139.87
Gl 800A	2.34	12.33−3.68+6.22	−0.113	−0.738	3.537	4.588
Gl 803	9.68	4.03−0.68+0.84	+0.154	−8.364	40.089	28.12
Gl 806	0.46	47.86−20.9+80.5	−0.336	−0.624	2.410	5.224
Gl 808	1.27	14.94−7.23+20.1	−0.882	−0.16	0.637	4.854
Gl 809	2.66	11.04−2.76+4.36	+0.067	−0.956	4.971	4.260
Gl 815AB	7.61	3.35−0.73+0.95	−0.167	−8.38	33.35	48.99
Gl 821	2.63	7.10−1.89+3.02	−0.484	−0.185	0.867	2.643
Gl 832	…	…	−0.268	−0.569	2.197	4.072
Gl 842	2.80	10.05−2.56+3.96	+0.050	−1.15	6.362	5.670
Gl 855	2.99	9.97−2.61+3.92	+0.049	−1.275	6.833	6.104
Gl 863	2.64	8.90−2.44+3.88	−0.132	−0.699	3.524	4.776
Gl 867A	7.02	4.81−0.98+1.31	+0.080	−7.272	28.08	23.36
Gl 880	2.07	14.25−4.09+7.43	+0.040	−1.165	5.321	4.853
Gl 887	…	…	−0.092	−0.670	3.284	4.059
Gl 895	0.52	56.16−22.6+71.4	+0.049	−1.675	7.848	7.011
Gl 908	2.25	9.54−2.59+4.48	−0.271	−0.270	1.294	2.415
St 497	6.5	3.95−1.45+1.98	−0.027	−6.20	29.05	30.91
St 928	2.1	11.16−4.86+8.74	−0.176	−0.94	4.183	6.273
G192-11A	2.6	10.14−2.71+4.33	−0.009	−2.405	12.12	12.37
MCC 354A	2.47	12.99−3.82+6.27	+0.109	−1.80	7.163	5.573
MCC 452	…	…	+0.360	−0.96	4.992	2.179
MCC 488	3.2	10.60−3.03+4.43	+0.113	−1.87	9.427	7.267
LHS 1155		…	…	−0.88	3.399	…

Note. We also give the Ca II EW (from the compilation of Paper XVIII), surface fluxes F_{HK}, and the surface fluxes corrected for the metallicity effects.
[a] Surface flux corrected from metallicity effects.

(This table is available in machine-readable form.)

Figure 4. We can see in this figure that there is a large scatter among M2 dwarf low-activity stars. Most of the subdwarfs also lie significantly apart from most of the M2 dwarfs. Most of this large scatter is due to metallicity effects on the Ca II line formation.

We used the empirical correlation found by Houdebine (2008, Paper VII) to determine the metallicity for each star as a function of its radius (see Paper I). We use these values here to correct the Ca II surface fluxes for metallicity effects, assuming a proportionality between surface flux and metallicity (optically thin case). The Ca II line EW, surface fluxes and surface fluxes corrected for metallicity are all listed in Table 3.

We show in Figure 5 the Ca II surface fluxes (after the data have been corrected for metallicity effects) as a function of $P/\sin i$. The improvement of the correlation between this figure and Figure 4 is striking: it shows how important it is to correct the RAC for metallicity effects in M dwarfs. In Figure 5, the scatter has been much reduced among the slow rotators, and also among the fast rotators. Moreover, even subdwarfs correlate with normal metallicity dwarfs.

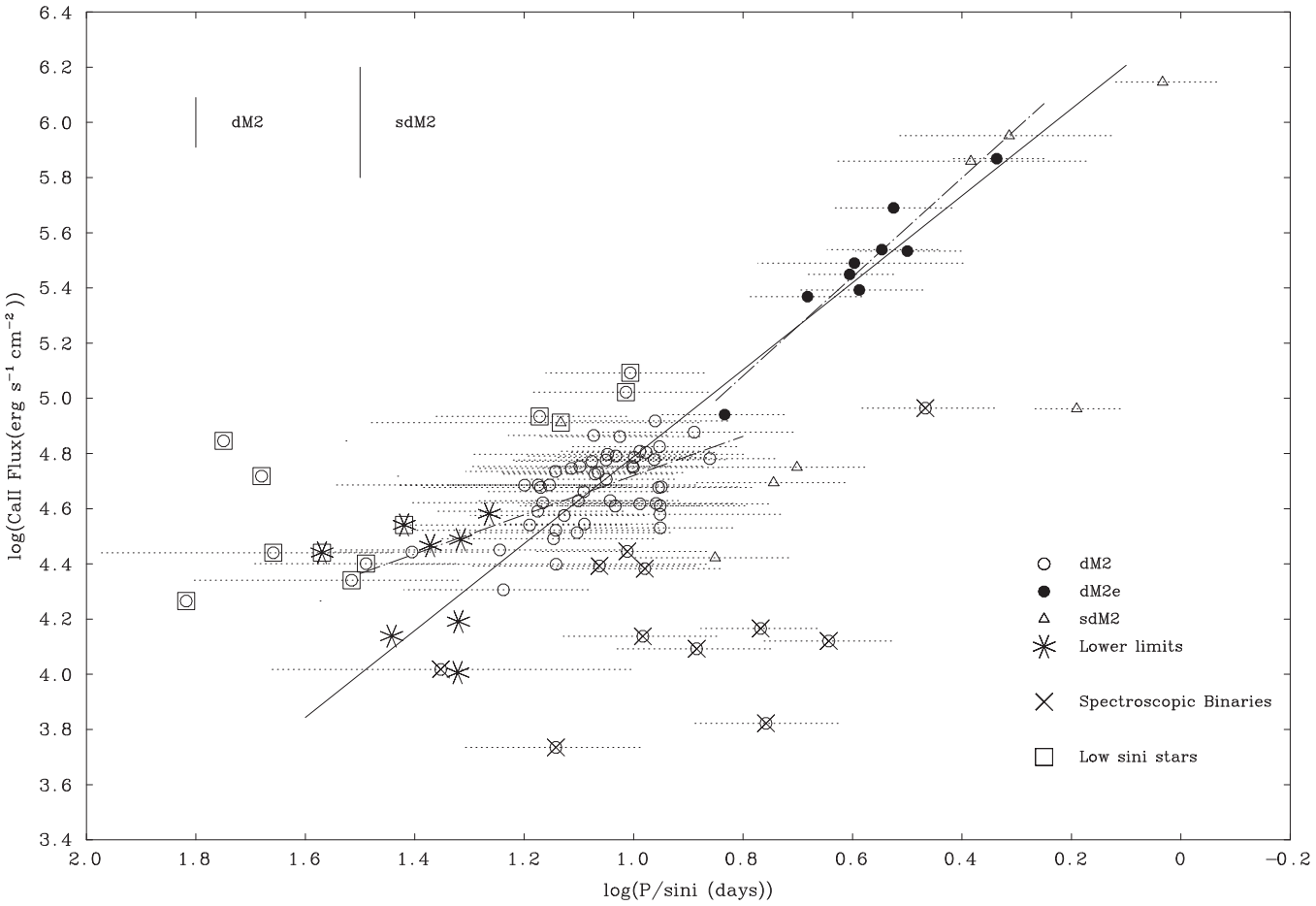

Figure 5. Correlation between the logarithm of the mean surface flux of the Ca II resonance doublet corrected for metallicity effects and $\log(P/\sin i)$ for stars with spectral sub-type dM2. The comparison between this correlation and that of Figure 4 is striking: it shows how important it is to correct for metallicity effects on the RAC in M dwarfs. In this figure, even subdwarfs now correlate with normal metallicity dwarfs. The straight solid line shows the heteroscedastic linear LSF to the data. The dotted-dashed lines show the heteroscedastic linear LSF to the low-activity star and high-activity star sub-samples. We show in the upper-left corner of the figure estimates of the uncertainties on the Ca II mean surface fluxes due to the corrections for metallicity effects, for dwarfs and subdwarfs.

In Figure 5, we plot the uncertainties on $P/\sin i$ as dotted lines for each star. For these uncertainties, we assumed an uncertainty of ± 0.14 km s^{-1} for measures of $v \sin i$ below 1 km s^{-1}, ± 0.30 km s^{-1} for $v \sin i$ between 1 km s^{-1} and 6 km s^{-1}, and ± 0.50 km s^{-1} for $v \sin i$ above 6 km s^{-1} (see Paper I). Uncertainties in the values of $P/\sin i$ have already been included in Figures 2 and 3, following the same prescription as we describe here. Similar uncertainties will be included in Figures 8 and 12 in connection with dM3 and dM4 stars, respectively.

In Figure 5, the straight solid line shows the heteroscedastic linear LSF to the data. There is little difference between this fit and the linear LSF that was obtained in Paper XV. There is a moderate shift between the two correlations, and the gradient is almost unchanged (see Table 2). We identified some low-activity, relatively fast rotators in this M2 dwarf sample. As mentioned in the previous section, these stars are probably unresolved spectroscopic binaries, so we have labelled these stars "spectroscopic binaries" in Figure 5. There are also a few stars that have rotation periods that are too long for their surface fluxes. We believe these stars are a sub-group of stars with low $\sin i$. These stars are shown as squares in Figure 5.

The heteroscedastic linear LSF to the RAC in Figure 5 gives the following:

$$F_{\mathrm{Ca\,II}} = 2.312 \pm 0.276 \times 10^6 \times (P/\sin i)^{-1.575 \pm 0.058}. \quad (11)$$

The parameters of this LSF are given in Table 1. The χ^2 is 0.028 for 66 dM2 stars.

The homoscedastic linear LSF to the RAC in Figure 5 gives the following:

$$F_{\mathrm{Ca\,II}} = 1.89 \pm 0.85 \times 10^6 \times (P/\sin i)^{-1.481 \pm 0.068}. \quad (12)$$

The parameters of this LSF are given in Table 2. The correlation coefficient is 0.949 and the χ^2 is 0.018 for 66 dM2 stars. The gradient of this correlation (-1.481) is very close to that of the correlation found in Paper XV (-1.53). In fact there are few differences between the two results: the correlation has only been shifted slightly in $P/\sin i$. Both the homoscedastic and the heteroscedastic fit give significant correlations with a statistical significance better than 99.9%. The heteroscedastic linear fit yields a somewhat slightly larger slope than the homoscedastic linear fit. This is because the errors on the dM2e stars are significantly smaller than those of the dM2 stars, and therefore the weights of the dM2e stars in the correlations are larger than those of dM2 stars in the heteroscedastic fit. As a consequence, the heteroscedastic fit goes through the

Table 4
Equivalent Width (EW, in Units of Å) of the Ca II Resonance Doublet and H_α Line for Our Sample of dM3 Stars (see HM)

		HARPS			SOPHIE				
Star	No. of meas.	Ca II H EW (A)	Ca II K EW (A)	H_α EW (A)	Ca II H EW (A)	Ca II K EW (A)	H_α EW (A)	K/H ratio	⟨Ca ii⟩
GJ 1046	6	−0.370 ± 0.01	−0.470 ± 0.01	0.329 ± 0.020	⋯	⋯	⋯	1.27	−0.420
GJ 1050	9	−0.101 ± 0.01	−0.125 ± 0.01	0.261 ± 0.020	⋯	⋯	⋯	1.24	−0.113
GJ 1097	7	−0.431 ± 0.01	−0.506 ± 0.01	0.306 ± 0.020	⋯	⋯	⋯	1.17	−0.469
GJ 1125	8, 8	−0.273 ± 0.01	−0.365 ± 0.01	0.248 ± 0.020	−0.29 ± 0.10	−0.48 ± 0.10	0.235 ± 0.020	1.34	−0.319
GJ 1203	8	−0.248 ± 0.01	−0.317 ± 0.01	0.298 ± 0.020	⋯	⋯	⋯	1.28	−0.283
GJ 1212AB	1	⋯	⋯	0.249 ± 0.020	⋯	⋯	⋯	⋯	⋯
GJ 1271	8	⋯	⋯	⋯	−0.61 ± 0.05	−0.91 ± 0.05	0.332 ± 0.020	1.49	−0.76
GJ 2121	1	⋯	⋯	0.286 ± 0.020	⋯	⋯	⋯	⋯	⋯
GJ 3139	2	−0.48 ± 0.03	−0.64 ± 0.03	0.365 ± 0.020	⋯	⋯	⋯	1.33	−0.560
GJ 3160AB	1	⋯	⋯	0.276 ± 0.020	⋯	⋯	⋯	⋯	⋯
GJ 3189	9	−0.065 ± 0.05	−0.127 ± 0.05	0.224 ± 0.020	⋯	⋯	⋯	1.95	−0.096
GJ 3279	10	−0.446 ± 0.01	−0.546 ± 0.03	0.362 ± 0.020	⋯	⋯	⋯	1.22	−0.496
GJ 3293	19	−0.736 ± 0.01	−0.824 ± 0.01	0.339 ± 0.020	⋯	⋯	⋯	1.12	−0.780
GJ 3404A	19	−0.303 ± 0.01	−0.336 ± 0.01	0.268 ± 0.020	⋯	⋯	⋯	1.11	−0.320
GJ 3412AB	1	⋯	⋯	⋯	−0.29 ± 0.10	−0.43 ± 0.20	0.255 ± 0.020	1.48	−0.36
GJ 3459	7	−0.428 ± 0.02	−0.523 ± 0.02	0.269 ± 0.020	⋯	⋯	⋯	1.22	−0.476
GJ 3528	6	−0.693 ± 0.02	−0.843 ± 0.02	0.342 ± 0.020	⋯	⋯	⋯	1.22	−0.768
GJ 3563	11	−0.320 ± 0.01	−0.388 ± 0.01	0.315 ± 0.020	⋯	⋯	⋯	1.21	−0.354
GJ 3598	1	⋯	⋯	0.316 ± 0.020	⋯	⋯	⋯	⋯	⋯
GJ 3634	49	−0.542 ± 0.01	−0.625 ± 0.01	0.376 ± 0.020	⋯	⋯	⋯	1.15	−0.584
GJ 3643	1	⋯	⋯	0.293 ± 0.020	⋯	⋯	⋯	⋯	⋯
GJ 3708A	8	−0.381 ± 0.02	−0.430 ± 0.02	0.275 ± 0.020	⋯	⋯	⋯	1.13	−0.406
GJ 3846	6	−0.483 ± 0.05	−0.496 ± 0.05	0.260 ± 0.020	⋯	⋯	⋯	1.03	−0.490
GJ 3892	8	−0.481 ± 0.01	−0.561 ± 0.01	0.334 ± 0.020	⋯	⋯	⋯	1.17	−0.521
GJ 3916AB	3	−0.357 ± 0.05	−0.418 ± 0.05	0.327 ± 0.020	⋯	⋯	⋯	1.17	−0.388
GJ 4004	2	⋯	⋯	0.220 ± 0.020	⋯	⋯	⋯	⋯	⋯
GJ 4231	4	−13.31 ± 0.5	−12.79 ± 0.5	−4.064 ± 0.1	⋯	⋯	⋯	0.96	−13.05[a]
GJ 4129	1	⋯	⋯	0.242 ± 0.020	⋯	⋯	⋯	⋯	⋯
Gl 12	6, 2	−0.252 ± 0.1	−0.214 ± 0.1	0.255 ± 0.020	⋯	⋯	0.270 ± 0.020	0.85	−0.233
Gl 70	7, 7	−0.538 ± 0.01	−0.659 ± 0.01	0.282 ± 0.020	−0.73 ± 0.05	−0.92 ± 0.05	0.251 ± 0.020	1.22	−0.701
Gl 84	2	−0.749 ± 0.05	−0.926 ± 0.05	⋯	⋯	⋯	⋯	1.24	−0.838[a]
Gl 109	28	⋯	⋯	⋯	−0.54 ± 0.01	−0.77 ± 0.01	0.225 ± 0.020	1.43	−0.655
Gl 145	6, 2	−0.757 ± 0.02	−0.853 ± 0.02	0.236 ± 0.020	⋯	⋯	⋯	1.13	−0.805
Gl 163	56	−0.369 ± 0.01	−0.431 ± 0.01	0.304 ± 0.020	⋯	⋯	⋯	1.17	−0.400
Gl 204.2	10	−0.532 ± 0.02	−0.586 ± 0.02	0.302 ± 0.020	⋯	⋯	⋯	1.10	−0.559
Gl 207.1	1, 4	−9.266 ± 0.2	−10.01 ± 0.2	−2.99 ± 0.020	−16.1 ± 1	−24.5 ± 2	−3.22 ± 0.20	1.08	−9.638
Gl 226	9	⋯	⋯	⋯	−0.40 ± 0.05	−0.68 ± 0.05	0.344 ± 0.020	1.70	−0.54
Gl 238	2	−0.409 ± 0.1	−0.381 ± 0.1	0.349 ± 0.020	⋯	⋯	⋯	0.93	−0.395
Gl 251	23	⋯	⋯	⋯	−0.25 ± 0.03	−0.38 ± 0.03	0.240 ± 0.020	1.52	−0.315
Gl 298	6	−0.498 ± 0.02	−0.619 ± 0.02	0.312 ± 0.020	⋯	⋯	⋯	1.24	−0.559
Gl 352	1	−0.261 ± 0.05	−0.326 ± 0.05	0.304 ± 0.020	⋯	⋯	⋯	1.25	−0.294
Gl 357	6	−0.186 ± 0.01	−0.217 ± 0.01	0.266 ± 0.020	⋯	⋯	⋯	1.17	−0.202
Gl 358	28	−2.45 ± 0.05	−2.72 ± 0.05	−0.532 ± 0.020	⋯	⋯	⋯	1.11	−2.585
Gl 377	8	−0.964 ± 0.01	−1.10 ± 0.01	0.319 ± 0.020	⋯	⋯	⋯	1.14	−1.032
Gl 386	6	−0.509 ± 0.01	−0.571 ± 0.01	0.323 ± 0.020	⋯	⋯	⋯	1.12	−0.540
Gl 388	40	−7.90 ± 0.05	−8.61 ± 0.05	−2.48 ± 0.020	⋯	⋯	⋯	1.09	−8.255
Gl 399	7	−0.443 ± 0.02	−0.529 ± 0.02	0.326 ± 0.020	⋯	⋯	⋯	1.19	−0.486
Gl 408	?	⋯	⋯	⋯	−0.54 ± 0.02	−0.77 ± 0.02	0.314 ± 0.020	1.43	−0.655
Gl 422	27	−0.212 ± 0.01	−0.246 ± 0.01	0.286 ± 0.020	⋯	⋯	⋯	1.16	−0.229
Gl 436	141, 19	−0.325 ± 0.01	−0.376 ± 0.01	0.300 ± 0.020	−0.27 ± 0.02	−0.45 ± 0.02	0.259 ± 0.020	1.16	−0.345
Gl 443	13	−0.898 ± 0.02	−1.093 ± 0.01	0.320 ± 0.020	⋯	⋯	⋯	1.22	−0.996
Gl 452A	11	−0.483 ± 0.03	−0.624 ± 0.03	0.357 ± 0.020	⋯	⋯	⋯	1.29	−0.554
Gl 452.1	11	−3.430 ± 0.05	−3.783 ± 0.05	−0.799 ± 0.020	⋯	⋯	⋯	1.10	−3.607
Gl 463	10	⋯	⋯	⋯	−0.51 ± 0.02	−0.72 ± 0.02	0.341 ± 0.020	1.41	−0.615
Gl 479	48	−1.608 ± 0.03	−1.847 ± 0.05	0.098 ± 0.020	⋯	⋯	⋯	1.15	−1.728
Gl 480	5, 21	−0.640 ± 0.05	−0.736 ± 0.05	0.314 ± 0.020	−0.75 ± 0.05	−1.17 ± 0.05	0.300 ± 0.020	1.15	−0.799
Gl 513	7	−0.365 ± 0.03	−0.425 ± 0.03	0.327 ± 0.020	⋯	⋯	⋯	1.16	−0.395
Gl 581	258	−0.190 ± 0.01	−0.224 ± 0.01	0.193 ± 0.020	⋯	⋯	⋯	1.18	−0.207
Gl 588	21	−0.592 ± 0.01	−0.704 ± 0.01	0.318 ± 0.020	⋯	⋯	⋯	1.19	−0.648
Gl 595	1	⋯	⋯	⋯	⋯	⋯	0.254 ± 0.020	⋯	⋯
Gl 617B	9	⋯	⋯	⋯	−0.84 ± 0.03	−1.30 ± 0.03	0.309 ± 0.020	1.55	−1.07

Table 4
(Continued)

Star	No. of meas.	HARPS Ca II H EW (A)	HARPS Ca II K EW (A)	HARPS H_α EW (A)	SOPHIE Ca II H EW (A)	SOPHIE Ca II K EW (A)	SOPHIE H_α EW (A)	K/H ratio	⟨Ca ii⟩
Gl 618A	19	−0.448 ± 0.01	−0.517 ± 0.01	0.312 ± 0.020	⋯	⋯	⋯	1.15	−0.483
Gl 623	3	⋯	⋯	⋯	−0.27 ± 0.10	−0.36 ± 0.10	0.248 ± 0.020	1.33	−0.315
Gl 634	9	−0.318 ± 0.03	−0.377 ± 0.03	0.353 ± 0.020	⋯	⋯	⋯	1.19	−0.348
Gl 644AB	1	−2.625 ± 0.05	−2.941 ± 0.05	−1.292 ± 0.20	⋯	⋯	⋯	1.12	−2.783
Gl 655	9	⋯	⋯	⋯	−0.45 ± 0.10	−0.80 ± 0.10	0.250 ± 0.020	1.78	−0.625
Gl 660A	1	−0.423 ± 0.1	−0.531 ± 0.1	0.262 ± 0.020	⋯	⋯	⋯	1.26	−0.477
Gl 671	7	⋯	⋯	⋯	−0.34 ± 0.02	−0.42 ± 0.02	0.279 ± 0.020	1.24	−0.38
Gl 674	44	−1.153 ± 0.01	−1.335 ± 0.01	0.125 ± 0.020	⋯	⋯	⋯	1.16	−1.244
Gl 687AB	16	⋯	⋯	⋯	−0.36 ± 0.01	−0.58 ± 0.02	0.292 ± 0.020	1.64	−0.47
Gl 693	7	−0.391 ± 0.03	−0.447 ± 0.03	0.271 ± 0.020	⋯	⋯	⋯	1.14	−0.419
Gl 694	11	⋯	⋯	⋯	−0.58 ± 0.01	−0.90 ± 0.01	0.317 ± 0.020	1.55	−0.74
Gl 725A	19	⋯	⋯	⋯	−0.22 ± 0.01	−0.34 ± 0.01	0.233 ± 0.020	1.55	−0.28
Gl 735A	1, 2	−8.286 ± 0.3	−8.743 ± 0.3	−1.99 ± 0.20	⋯	⋯	−1.71 ± 0.20	1.06	−8.515
Gl 735B	1, 2	−5.360 ± 0.3	−5.623 ± 0.3	−1.99 ± 0.20	⋯	⋯	−1.71 ± 0.20	1.05	−5.492
Gl 739	2	−0.636 ± 0.1	−0.788 ± 0.1	0.292 ± 0.020	⋯	⋯	⋯	1.24	−0.712
Gl 752A	13, 7	−0.784 ± 0.01	−0.910 ± 0.01	0.338 ± 0.020	−0.72 ± 0.02	−1.16 ± 0.02	0.375 ± 0.020	1.16	−0.828
Gl 781.1A	3	>−0.30	>−0.30	0.206 ± 0.020	⋯	⋯	⋯	⋯	>−0.30
Gl 793	8	⋯	⋯	⋯	−1.12 ± 0.04	−1.78 ± 0.04	0.111 ± 0.020	1.59	−1.45
Gl 844	16	⋯	⋯	⋯	−1.32 ± 0.05	−2.08 ± 0.05	0.236 ± 0.020	1.58	−1.70
Gl 849	36	−0.580 ± 0.01	−0.694 ± 0.01	0.355 ± 0.020	⋯	⋯	⋯	1.20	−0.637
Gl 877	41	−0.454 ± 0.01	−0.528 ± 0.01	0.308 ± 0.020	⋯	⋯	⋯	1.16	−0.491
Gl 896A	1	⋯	⋯	⋯	−8.98 ± 0.20	−12.5 ± 0.20	−3.80 ± 0.20	1.39	−10.74

Notes. Results were obtained using spectra from HARPS, SOPHIE, and FEROS.
[a] FEROS spectrum.

(This table is available in machine-readable form.)

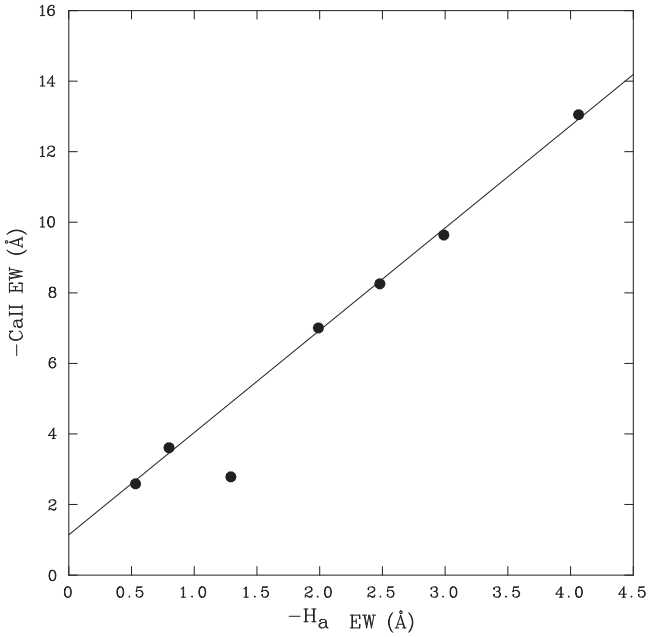

Figure 6. Correlation between the mean EW of the Ca II resonance doublet and the H_α EW for stars with spectral sub-type dM3e. The solid line is the least square fit to the data.

sub-sample of dM2e stars whereas the homoscedastic fit underestimates clearly the higher fluxes of the dM2e stars. Therefore the heteroscedastic fit provides globally a better evaluation of the slope for the dM2+dM2e stars.

We also performed linear LSF to the sub-samples of only the dM2 low-activity and the high-activity dM2e stars (see Table 1). The heteroscedastic linear LSF to the dM2 low-activity stars sub-sample yields:

$$F_{\mathrm{Ca\,II}} = 2.68 \pm 0.77 \times 10^5 \times (P/\sin i)^{-0.709\pm0.14}. \quad (13)$$

Therefore, the gradient of the RAC for the low-activity dM2 stars is again significantly shallower than that of the combined sample of low+high-activity stars.

For the homoscedastic linear LSF to the dM2 low-activity stars, we obtain:

$$F_{\mathrm{Ca\,II}} = 4.17 \pm 1.15 \times 10^5 \times (P/\sin i)^{-0.891\pm0.12}. \quad (14)$$

Both the heteroscedastic and the homoscedastic fits show that the gradient of the RAC for the low-activity dM2 stars is again (as for dK4 and dK6 stars) significantly shallower than those of the combined sample of low+high-activity stars. The χ^2 for these fits are 0.046 and 0.013, respectively. These fits are statistically significant at a confidence level better than 99.9%. We note that the slope of the heteroscedastic fit is slightly shallower than that of the homoscedastic fit and is also shallower than the value found for the heteroscedastic fit for the dK6 sample. However, if we take into account errors (see Table 1), there are in fact no significant differences between these values.

The heteroscedastic linear LSF to the dM2e high-activity star sub-sample yields:

$$F_{\mathrm{Ca\,II}} = 3.28 \pm 0.54 \times 10^6 \times (P/\sin i)^{-1.793\pm0.14}. \quad (15)$$

Therefore, the slope of the RAC for the high-activity dM2e stars is again steeper than that of the combined sample of low

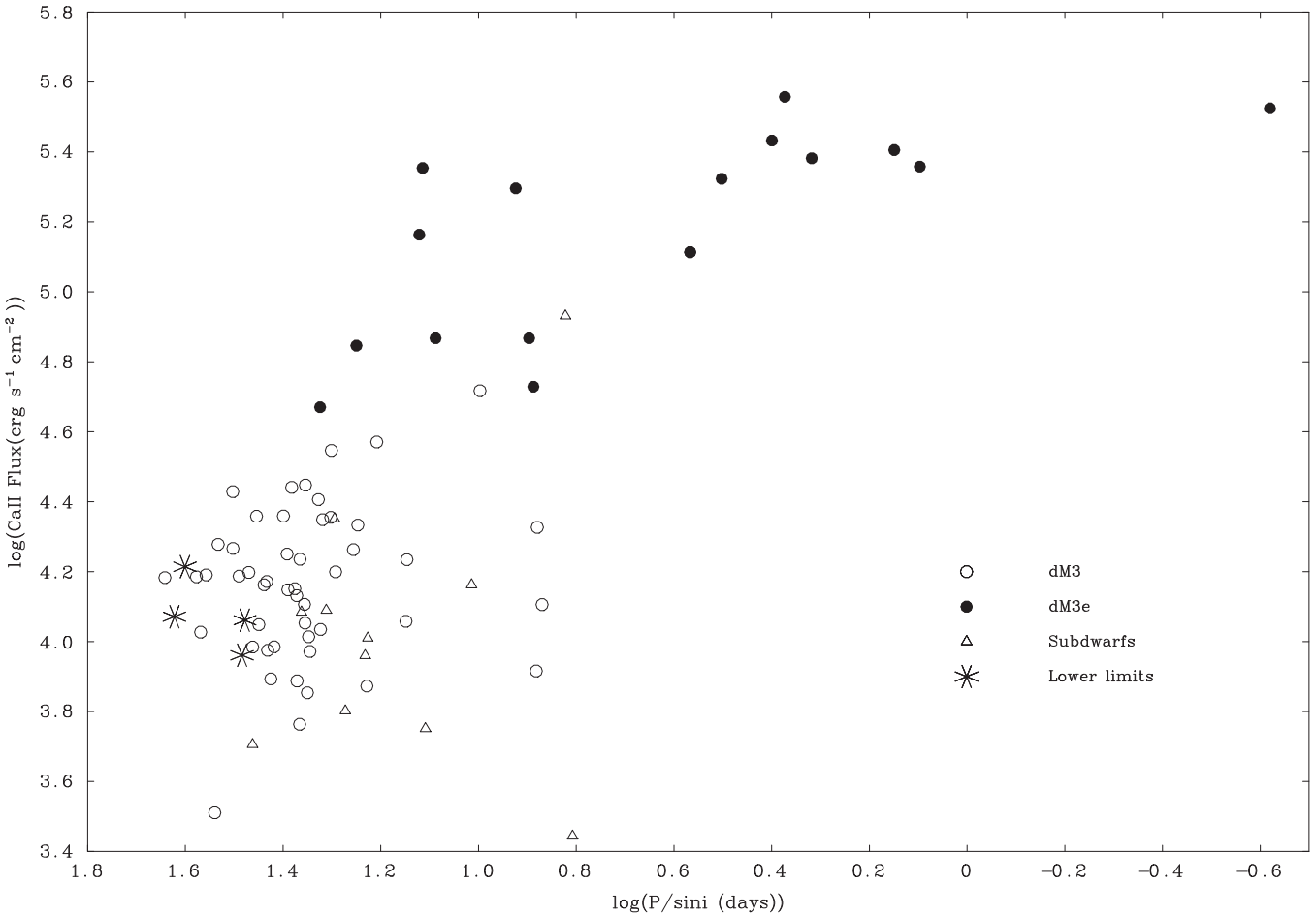

Figure 7. Correlation between the logarithm of the mean surface fluxes of the Ca II resonance doublet and $\log(P/\sin i)$ for stars with spectral sub-type dM3. No corrections for metallicity were applied here. One can see that (as for the case of dM2 stars) there is a large scatter among the data when it is not corrected for metallicity effects.

+high-activity stars. We note that this slope gets closer to that of the combined sample as we move from dK4 to dM2. The differences between these two slopes were larger for dK4 and dK6 stars.

The parameter $\frac{R}{\delta}$ is 23.45 for the high-activity star sub-sample and 34.77 for the low-activity star sub-sample. Therefore, the parameter $\delta = \frac{\langle \text{error} \rangle}{\sqrt{n}}$, which is a normalized estimate of the mean error on the measurements, is much smaller than the period domains of the RACs in both cases. Hence, these LSFs should be relatively well established, which corresponds to the high statistical significances we obtain (Table 1). However, we consider again these results as still preliminary because the domains of the RACs are relatively small compared to the typical uncertainties on individual measures.

3.5. The RAC in M3 Dwarfs

In HM, we have already listed the results for the rotational parameters $v \sin i$ and $P/\sin i$ of our dM3 stellar sample. However, we re-computed the stellar parameters for our sample of dM3 stars in Paper I according to the new results of Mann et al. (2015). The revised values of the parameters for the dM3 sample can be found in Paper I. In the present paper, we report on chromospheric line data for dM3 stars: these data were not a part of HM. In Table 4, we list the EW we have obtained for the Ca II resonance doublet and for the H_α line for our dM3 stars.

In order to supplement our sample of $v \sin i$ and Ca II measurements, and in order to have an unbiased sample of measurements, we searched the literature for additional $v \sin i$ and Ca II measurements. We found several additional stars with $v \sin i$ measurements (see Paper I), but we found only a few measurements of the Ca II lines for these stars (Stauffer & Hartmann 1986; Rutten 1987; Giampapa et al. 1989; Rutten et al. 1989). Instead, we found several measures of the H_α EW (Soderblom et al. 1991; Hawley et al. 1996; Kamper et al. 1997; Christian & Mathioudakis 2002; Gizis et al. 2002; Pace 2013). Fortunately, there is a relatively tight correlation between the mean Ca II line mean EW and H_α EW in dM3 and dM4 stars. Therefore, we decided to infer the Ca II line mean EW from the measures of the H_α EW. We show in Figure 6 the relationship between the Ca II line mean EW and the H_α EW for our measurements of dM3 stars (see Table 4). As one can see, the correlation between these two parameters is very good for all stars except Gl 644AB, which lies slightly below. The homoscedastic linear least square fit to this data except Gl 644AB gives:

$$\text{EW}_{\text{Ca II}} = 2.90 \pm 0.05 \times \text{EW}_{\text{H}_\alpha} + 1.14 \pm 0.125. \quad (16)$$

The parameters of this fit are given in Table 1. The fit is very good with a correlation coefficient of 0.9994. We give the Ca II line mean EW computed from the H_α EW in Table 4.

Table 5
The Values of $v \sin i$, $P/\sin i$ and [M/H] from Paper I for Our Targets in Our List of dM3 Stars

Star	$v \sin i$ (km s^{-1})	$P/\sin i$ (days)	[M/H] (dex)	Ca II EW (Å)	F_{HK}	F_{HK}[a] (10^4 erg s^{-1} cm^{-2})
GJ 1046	2.63	7.41−1.1+1.2	−0.078	−0.420	1.276	1.527
GJ 1050	0.59	34.4−18+310	−0.035	−0.113	0.324	0.351
GJ 1054B	32.13	0.45−0.07+0.08	−0.323	…	…	…
GJ 1097	<0.5	>41.91	−0.033	−0.469	1.178	1.271
GJ 1125	0.99	10.3−2.9+8.3	−0.691	−0.319	1.454	7.138
GJ 1203	0.82	23.5−7.1+18	−0.087	−0.283	0.772	0.943
GJ 1212A	0.69	25.3−9.6+57	−0.170	…	…	…
GJ 1212B	0.90	19.3−7.1+13	−0.170	…	…	…
GJ 1271	1.39	20.0−5.1+7.7	+0.127	−0.76	2.265	1.691
GJ 2121	2.06	12.5−3.1+4.2	+0.059	…	…	…
GJ 3139	0.90	29.4−7.8+14	+0.084	−0.560	1.577	1.300
GJ 3160A	0.95	22.0−6.2+9.9	−0.033	…	…	…
GJ 3160B	1.06	19.8−5.3+7.4	−0.033	…	…	…
GJ 3189	1.42	6.43−1.8+1.6	−0.801	−0.096	0.278	1.758
GJ 3279	0.85	23.7−13+26	−0.045	−0.496	1.417	1.572
GJ 3293	0.85	25.0−12+25	−0.031	−0.780	2.287	2.456
GJ 3404A	0.90	26.5−9.8+17	−0.005	−0.320	0.782	0.791
GJ 3412A	…	…	−0.280	−0.36	0.914	1.742
GJ 3412B	…	…	−0.280	−0.36	0.914	1.742
GJ 3459	0.69	23.1−7.7+48	−0.238	−0.476	1.215	2.102
GJ 3528	0.90	28.4−8.1+15	+0.057	−0.768	2.283	2.002
GJ 3563	0.85	22.2−6.3+14	−0.104	−0.354	1.033	1.313
GJ 3598	0.69	30.0−15+80	−0.035	…	…	…
GJ 3634	0.85	24.6−11+22	−0.033	−0.584	1.780	1.921
GJ 3643	1.00	20.4−5.7+9.0	−0.036	…	…	…
GJ 3708A	0.50	37.0−17+∞	−0.122	−0.406	1.064	1.409
GJ 3846	0.82	20.5−6.4+16	−0.189	−0.490	1.230	1.901
GJ 3892	0.82	27.4−7.6+20	−0.026	−0.521	1.453	1.543
GJ 3916A	1.24	14.1−3.1+3.8	−0.168	−0.388	1.143	1.683
GJ 3916B	3.51	4.97−0.7+0.7	−0.168	−0.388	1.143	1.683
GJ 4004	0.59	28.6−18+290	−0.186	…	…	…
GJ 4129	0.50	37.9−18+∞	−0.104	…	…	…
GJ 4231	80.00	0.24−0.08+0.09	−0.080	−13.05	33.48	40.25
GJ 4282AB	15.00	1.25−0.48+0.54	−0.115	−9.115	22.82	29.74
Gl 12	0.95	12.8−4.4+6.9	−0.508	−0.233	0.564	1.817
GL 48	2.45	10.7−2.9+4.9	+0.071	…	…	…
Gl 70	1.01	20.8−5.4+10	−0.033	−0.701	2.233	2.409
GL 84	…	…	−0.094	−0.838	2.555	…
Gl 109	1.34	13.9−3.2+4.8	−0.113	−0.655	1.716	2.226
Gl 119B	4.00	7.72−2.2+3.0	+0.217	−1.840	5.358	3.251
Gl 140C	6.70	2.99−1.0+1.3	−0.052	−1.36	4.173	4.704
Gl 145	0.85	19.6−5.1+12	−0.194	−0.805	2.246	3.511
Gl 163	0.85	26.0−6.8+16	−0.027	−0.400	0.966	1.028
Gl 204.2	0.69	36.1−14+83	+0.033	−0.559	1.552	1.438
Gl 207.1	9.52	2.51−0.4+0.4	+0.006	−9.638	27.08	26.71
Gl 226	1.12	19.6−5.1+9.0	−0.028	−0.54	1.583	1.688
Gl 238	0.85	28.0−7.3+17	+0.005	−0.395	1.118	1.105
Gl 251AB	1.14	16.9−4.4+7.5	−0.388	−0.315	0.746	1.823
GL 277A	8.00	3.69−0.86+1.1	+0.175	−4.958	8.13	8.682
GL 298	1.00	24.6−5.7+9.2	+0.023	−0.559	1.407	1.334
GL 352	0.90	7.6−1.0+1.0	+0.178	−0.294	0.824	0.547
Gl 357	1.21	18.7−4.3+8.2	−0.189	−0.202	0.634	0.980
Gl 358	1.10	17.7−3.3+4.2	−0.030	−2.585	7.018	7.520
Gl 377	…	24.1−5.4+7.2	+0.084	−1.032	2.760	2.275
Gl 386	0.69	37.8−12+79	+0.068	−0.540	1.532	1.310
Gl 388	2.63	8.38−1.1+1.2	−0.028	−8.255	19.77	21.09
Gl 399	0.59	43.6−17+330	+0.064	−0.486	1.524	1.315
Gl 408	1.12	18.1−4.6+8.1	−0.045	−0.655	1.832	2.032
Gl 422	0.90	23.1−5.8+11	−0.033	−0.229	0.580	0.626
Gl 436	0.86	27.0−9.0+26	−0.019	−0.345	0.944	0.986
Gl 443	0.90	31.8−8.7+16	+0.150	−0.996	2.684	1.900
Gl 452A	0.95	27.1−7.3+12	+0.062	−0.554	1.485	1.287
Gl 452.1	1.60	6.66−1.9+2.2	−0.651	−3.607	8.541	38.24

Table 5
(Continued)

Star	$v \sin i$ (km s^{-1})	$P/\sin i$ (days)	[M/H] (dex)	Ca II EW (Å)	F_{HK}	F_{HK}[a] (10^4 erg s^{-1} cm^{-2})
Gl 463	1.17	23.1−6.4+10	+0.101	−0.615	1.720	1.363
Gl 479	1.06	21.1−4.4+6.3	−0.026	−1.728	4.679	4.968
Gl 480	0.73	34.0−12+53	+0.033	−0.799	1.897	1.758
Gl 513	0.77	29.0−11+39	−0.027	−0.395	0.965	1.027
GL 581	…	…	−0.215	−0.207	0.508	0.833
Gl 588	0.77	31.8−8.3+35	+0.022	−0.648	1.847	1.756
Gl 595AB	1.62	9.25−2.1+2.8	−0.293	…	…	…
Gl 617B	1.12	22.6−6.0+11	+0.045	−1.07	2.803	2.527
Gl 618A	0.82	22.8−6.9+18	−0.115	−0.483	1.278	1.665
Gl 623	0.94	22.3−6.4+16	−0.034	−0.315	0.937	1.013
Gl 634	1.00	17.1−5.0+7.8	−0.182	−0.348	0.912	1.387
Gl 644A	1.79	12.2−2.0+2.2	−0.029	−2.783	7.366	7.875
Gl 644B	2.78	7.88−1.1+1.1	−0.029	−2.783	7.366	7.875
Gl 655	<0.5	>39.88	−0.057	−0.625	1.637	1.867
Gl 660A	0.82	22.6−8.3+20	−0.120	−0.477	1.130	1.490
Gl 671	0.94	21.2−6.3+15	−0.061	−0.38	1.083	1.246
Gl 674	0.90	20.0−4.5+8.6	−0.143	−1.244	3.521	4.894
Gl 687AB	0.73	30.3−11+130	−0.028	−0.47	1.151	1.228
Gl 693	0.82	16.8−4.3+12	−0.372	−0.419	1.024	2.412
Gl 694	1.29	17.7−4.2+6.2	−0.024	−0.74	2.155	2.277
Gl 725AB	0.85	22.5−7.0+18.4	−0.372	−0.28	0.714	1.682
Gl 735A	1.86	13.0−2.0+2.4	+0.012	−8.515	22.60	21.98
Gl 735B	1.83	13.2−2.1+3.1	+0.012	−5.492	14.57	14.17
Gl 739	3.19	7.59−1.0+1.0	+0.012	−0.712	2.122	2.064
Gl 752A	1.19	21.2−4.3+6.7	+0.045	−0.828	2.549	2.298
GL 781.1A	9.20	1.93−0.50+0.62	−0.157	…	…	…
Gl 793	1.26	16.2−4.0+5.9	−0.036	−1.45	3.720	4.042
Gl 844	3.46	9.92−1.4+1.4	+0.324	−1.70	5.216	2.474
Gl 849	0.85	30.8−7.8+18	+0.076	−0.637	1.539	1.292
GL 856AB	11.00	2.36−0.63+0.76	+0.067	−14.42	36.11	30.95
GL 875.1	11.00	2.08−0.44+0.52	−0.024	−9.62	24.09	25.46
Gl 877	0.95	23.5−5.0+8.2	−0.026	−0.491	1.353	1.436
Gl 896A	14.03	1.41−0.14+0.14	−0.064	−10.74	25.43	29.47
Gl 897AB	7.10	3.18−0.97+1.29	−0.025	−7.250	21.06	22.31

Notes. We also give the Ca II EWs, surface fluxes F_{HK}, and the surface fluxes corrected for the metallicity effects.
[a] Surface flux corrected for metallicity effects.

(This table is available in machine-readable form.)

We show the RAC for dM3 stars for the raw data in Figure 7. In this figure, one can see that the scatter is very large among both dM3 and dM3e stars. The same kind of scatter was observed among the raw data of dM2 stars (Figure 4). Considering the good correction we had for the metallicity in the previous section for dM2 stars, we decided to compile all the metallicities published for our initial selection list of 381 dM3 stars, and try to obtain a metallicity–radius correlation for these stars, similarly to the dM2 stars in Paper VII. We found metallicities from the literature for 147 dM3 stars. This data and the radius–[M/H] relationship were reported in Paper I. Data for M3 stars corrected for metallicity can be found in Table 5 and Figure 8.

We show in Figure 8 the RAC corrected for metallicity effects for dM3 stars. The scatter is reduced compared to the raw data in Figure 7, but there remains a significant scatter among both dM3 and dM3e stars. The corrected correlation is not as good as for dM2 stars. We believe this is due partly to the poorer statistics we have on the Ca II line EWs. Indeed, for dM3 stars, we have very few measurements of the Ca II lines EWs (Table 4) whereas, for dM2 stars, we had several measurements for almost all stars (see Houdebine et al. 2012, Paper XIX). We also observe a larger scatter in the radius–[M/H] relationship for dM3 stars (see Paper I) compared to dM2 stars. This may also lead to poorer corrections of the metallicity effects on the RAC.

Among our sample of dM3 stars, we observe a sub-sample of relatively fast rotating, low-activity stars. Again, as in the case of dM2 stars, we believe that these stars are unresolved spectroscopic binaries. We also found three stars with possibly low $v \sin i$ (see Figure 8). In the corrected RAC, most of the subdwarfs now follow the same correlation as normal dwarfs, indicating that our metallicity corrections are reasonably correct.

We find that for periods above 7 days or so, the gradient between the dM3 stars (open circles, the slowest rotators) and the dM3e stars (filled circles, the fastest rotators) is very steep. Because we have only a few dM3e stars compared to the larger group of dM3 stars, we do not obtain a good linear LSF to both the dM3 and dM3e sub-samples. This is due to the fact that the linear LSF to the dM3 sub-sample gives a shallower gradient (−0.90, Table 1) compared to the dM3+dM3e sample. Therefore, we gave higher weights to our dM3e data points: we find that a weight of 7 to dM3e stars and 1 to dM3

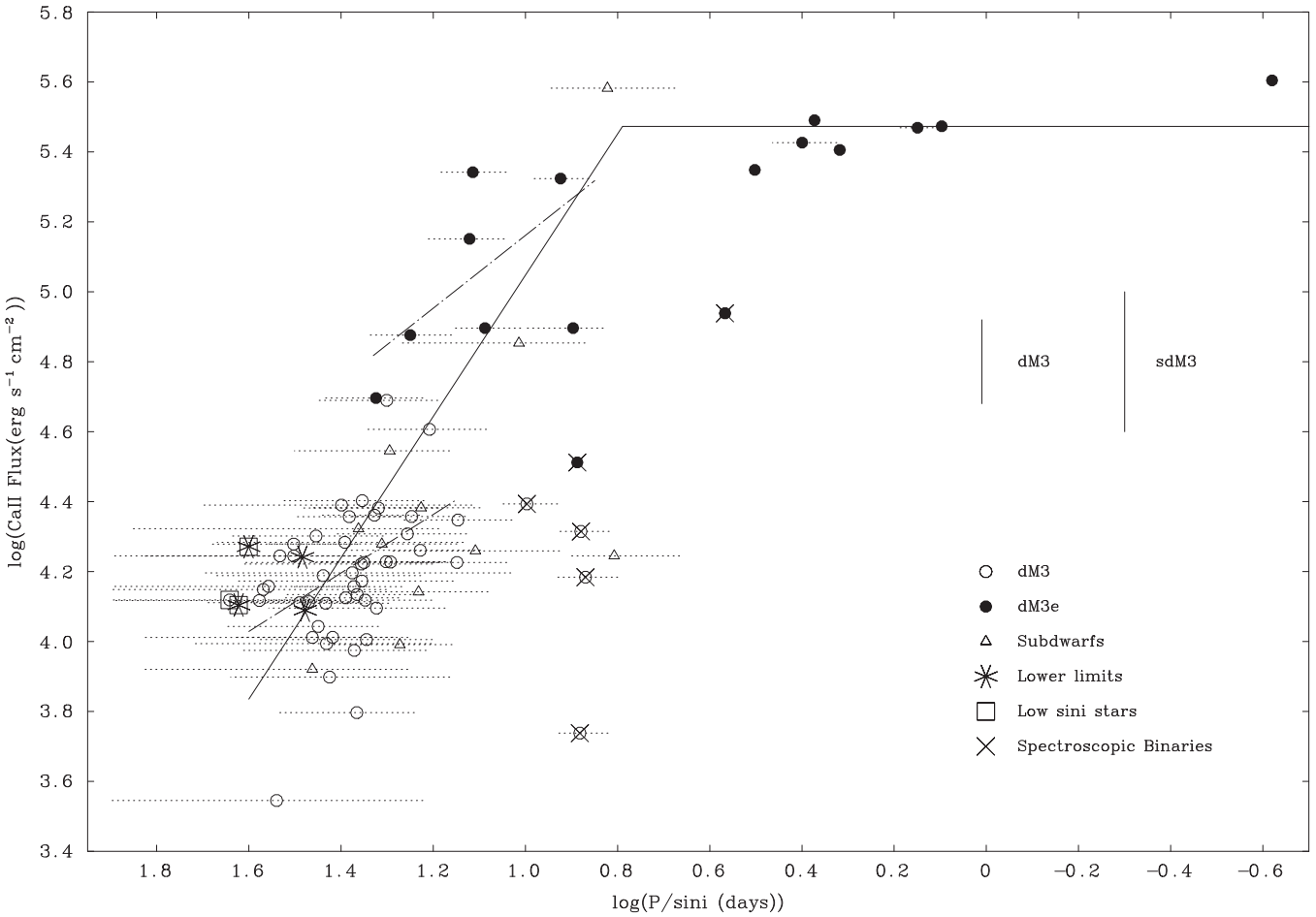

Figure 8. Correlation between the logarithm of the mean surface fluxes of the Ca II resonance doublet corrected for metallicity effects and $\log(P/\sin i)$ for stars with spectral sub-type dM3 (see Section 3.5). Note the possible feature of "saturation" at $P/\sin i < 6$ days. For "unsaturated" stars, i.e., those with $P/\sin i > 7$ days, the solid straight line is the heteroscedastic linear LSF to the combined data set of low+high-activity stars. The dotted-dashed curves represent the heteroscedastic linear LSFs to the low-activity star and high-activity star sub-samples, respectively (see the text). In the center-right hand of the figure, we show estimates of the uncertainties on the Ca II mean surface fluxes due to the corrections for metallicity effects, for dwarfs and subdwarfs.

stars gives a good fit to both data sub-samples. For $P/\sin i \geqslant 6.7$ days, we obtain the following heteroscedastic linear LSF for our dM3+dM3e sample (Table 1):

$$F_{\mathrm{Ca\,II}} = 1.169 \pm 0.476 \times 10^{7} \times (P/\sin i)^{-2.020 \pm 0.11}. \quad (17)$$

The gradient in Equation (17) (-2.02 ± 0.11) is significantly steeper than the gradients that we determined for our dK4 and dK6 samples (-0.814 ± 0.059 and -1.047 ± 0.042, respectively; see Figures 2 and 3). But interestingly, the mean gradient in Figure 8 is intermediate between that of dM2 stars (-1.575 ± 0.058) and that of dM4 stars (-2.56 ± 0.19; Table 1). Once again, this is an encouraging sign that the physical parameters we have derived for dM3 stars are plausible when compared with stars that are slightly hotter and slightly cooler. We plot the linear LSF for stars with periods $P/\sin i > 7$ days (we refer to these as unsaturated stars; see below) in Figure 8 (solid line).

For the homoscedastic fit, we obtain the following linear LSF for our dM3+dM3e sample (Table 1):

$$F_{\mathrm{Ca\,II}} = 1.52 \pm 1.00 \times 10^{7} \times (P/\sin i)^{-2.075 \pm 0.19}. \quad (18)$$

The slopes of both the heteroscedastic and the homoscedastic linear fits are comparable. Note that the uncertainty on the slope is smaller for the heteroscedastic fit than for the homoscedastic fit. Both fits confirm that the slope of the RAC is getting steeper as we move to later spectral types.

As we saw in Section 1.4, one would expect the RAC to flatten out for rotation periods shorter than 2–10 days. We have several objects in our M3 sample that have shorter rotation periods. We note that the RAC flattens out ("saturates") for the fastest rotating dM3e stars for $P/\sin i < 6$ days. In this period range, we find seven fast rotators with about the same surface flux ($\sim 2.97 \times 10^{5}$ erg s^{-1} cm^{-2}), which corresponds to the maximum observed in the unsaturated portion of the RAC. Although, in the present data set, we do not have enough data to clearly confirm the presence of a saturation plateau, one should expect saturation to occur among some of our sample stars according to previous investigations. We propose that saturation in our present dM3 sample occurs at about $\sim$6 days, which agrees with the expectations of saturation occurring in the range of 2–10 days. In Figure 8, we therefore represent the fits of the RAC in the "unsaturated" portion, and draw a flat plateau in the expected "saturated" portion of the RAC.

The fact that certain stars in our samples probably lie in a saturated regime, while others are found to lie in an unsaturated regime, has a bearing on a methodological point that was made in Section 1.1: a study of stellar dynamos is best done (we believe) by focusing on stars in an unsaturated regime.

Table 6
Equivalent Width (EW, in Units of Å) of the Ca II Resonance Doublet and H_α Line for Our Sample of dM4 Stars

Star	No. meas.	FEROS Ca II H EW (Å)	FEROS Ca II K EW (Å)	H_α EW (Å)	Mean Ca II EW (Å)	S_{HK}	Mean Ca II EW[a] (Å)	H_α EW (Å)	Mean Ca II EW (Å)
GJ 1001A	1	−0.20 ± 0.04	−0.09 ± 0.07	0.215 ± 0.02	−0.235(2)	⋯	⋯	0.218(15)	−0.235(2)
GJ 1005	⋯	⋯	⋯	⋯	⋯	⋯	⋯	0.224	⋯
GJ 1006A	2	−4.09 ± 0.04	−4.72 ± 0.04	−3.14 ± 0.20	−4.405(2)	⋯	⋯	−3.14(2)	−4.405(2)
GJ 1006B	2	−7.05 ± 0.05	−8.55 ± 0.05	−2.98 ± 0.20	−7.80(2)	⋯	⋯	−2.98(2)	−7.80(2)
GJ 1065	3	−0.26 ± 0.08	−0.24 ± 0.08	0.167 ± 0.02	−0.25(3)	⋯	⋯	0.189(4)	−0.25(3)
GJ 1105	⋯	⋯	⋯	⋯	−0.62(1)	⋯	⋯	0.203(3)	−0.62(1)
GJ 1129	3	−0.302 ± 0.03	−0.353 ± 0.03	0.190 ± 0.02	−0.328(3)	⋯	⋯	0.178(4)	−0.328(3)
GJ 1134	⋯	⋯	⋯	⋯	−0.095(1)	⋯	⋯	0.181(3)	⋯
GJ 1138	⋯	⋯	⋯	⋯	⋯	⋯	⋯	0.180(4)	⋯
GJ 1207	8	-6.529 ± 0.08	−7.801 ± 0.08	−2.55 ± 0.20	−7.098(11)	⋯	⋯	−2.830(11)	−7.098(11)
GJ 1254	⋯	⋯	⋯	⋯	⋯	⋯	⋯	0.133	⋯
GJ 1289	⋯	⋯	⋯	⋯	−1.680(1)	⋯	⋯	−0.432(18)	−1.680(1)
GJ 2036B	⋯	⋯	⋯	⋯	⋯	⋯	−14.49(2)	−8.135(2)	−14.49(2)
GJ 2069A	⋯	⋯	⋯	⋯	−16.91(1)	⋯	⋯	−4.548(5)	−16.91(1)
GJ 3149B	⋯	⋯	⋯	⋯	⋯	⋯	−5.647(1)	−3.50	−5.647(1)
GJ 3283B	⋯	⋯	⋯	⋯	⋯	⋯	−6.372(1)	−3.88	−6.372(1)
GJ 3322	⋯	⋯	⋯	⋯	⋯	⋯	−10.58(2)	−6.082(2)	−10.58(2)
GJ 3522	⋯	⋯	⋯	⋯	−7.10(1)	⋯	⋯	⋯	−7.10(1)
GJ 3631	⋯	⋯	⋯	⋯	⋯	⋯	−19.29(2)	−10.65(2)	−19.29(2)
GJ 3666	⋯	⋯	⋯	⋯	−0.21(1)	⋯	⋯	⋯	−0.21(1)
GJ 3707	2	−0.287 ± 0.08	−0.365 ± 0.08	0.200 ± 0.02	−0.341(9)	⋯	⋯	0.226(9)	−0.341(9)
GJ 3789	⋯	⋯	⋯	⋯	⋯	⋯	−19.31(3)	−10.66(3)	−19.31(3)
GJ 3801	⋯	⋯	⋯	⋯	⋯	⋯	⋯	0.212	⋯
GJ 3804	4	−0.251 ± 0.05	−0.366 ± 0.05	0.193 ± 0.02	−0.302(9)	0.648(4)	−0.291(4)	0.211(5)	−0.299(13)
GJ 3873	⋯	⋯	⋯	⋯	−0.465(3)	⋯	⋯	0.217(4)	−0.465(3)
GJ 3900	1	−0.401 ± 0.05	−0.504 ± 0.05	0.221 ± 0.02	−0.453(1)	⋯	⋯	0.240(3)	−0.453(1)
GJ 4020B	⋯	⋯	⋯	⋯	⋯	⋯	−12.94(1)	−7.32(1)	−12.94(1)
GJ 4063	⋯	⋯	⋯	⋯	−0.380(9)	1.235(14)	−0.631(14)	0.232(2)	−0.533(23)
GJ 4333	2	−0.495 ± 0.08	−0.572 ± 0.08	0.179 ± 0.02	−0.587(15)	1.060(4)	−0.525(4)	0.180(5)	−0.574(19)
GJ 4338B	⋯	⋯	⋯	⋯	⋯	⋯	−10.95(2)	−6.277(2)	−10.95(2)
GJ 4378A	2	−2.674 ± 0.1	−3.004 ± 0.1	−1.486 ± 0.20	−2.839(2)	⋯	⋯	−1.808(3)	−2.839(2)
GJ 4378B	2	−7.509 ± 0.1	−9.684 ± 0.1	−4.434 ± 0.20	−8.597(2)	⋯	⋯	−4.434(2)	−8.597(2)
Gl 15B	⋯	⋯	⋯	⋯	−0.964(14)	1.162(18)	−0.888(18)	0.216(4)	−0.921(32)
Gl 46	2	−0.208 ± 0.02	−0.321 ± 0.02	0.231 ± 0.02	−0.295(4)	⋯	⋯	0.241(4)	−0.295(4)
Gl 54.1	6	−8.814 ± 0.2	−9.027 ± 0.2	−2.099 ± 0.20	−7.044(17)	4.816(4)	−3.230(4)	−2.010(8)	−6.318(21)
Gl 84.1B	⋯	⋯	⋯	⋯	−0.625(7)	⋯	⋯	0.549(7)	−0.625(7)
Gl 105B	1	−0.278 ± 0.05	−0.313 ± 0.05	0.204 ± 0.02	−0.319(4)	0.727(1)	−0.372(1)	0.188(3)	−0.330(5)
Gl 166C	1	−5.206 ± 0.2	−5.502 ± 0.2	−2.999 ± 0.20	−5.354(1)	6.588(2)	−4.705(2)	−3.227(8)	−4.921(3)
Gl 169.1A	⋯	⋯	⋯	⋯	⋯	⋯	⋯	0.174(1)	⋯
Gl 179	2	−0.626 ± 0.03	−0.759 ± 0.03	0.228 ± 0.02	−0.676(34)	1.592(4)	−0.856(4)	0.230(21)	−0.695(38)
Gl 203	2	−0.119 ± 0.05	−0.137 ± 0.05	0.177 ± 0.02	−0.121(5)	⋯	⋯	0.203(13)	−0.121(5)
Gl 206AB	⋯	⋯	⋯	⋯	−8.55(1)	⋯	⋯	−4.25(1)	−8.55(1)
Gl 206A	3	−7.348 ± 0.2	−8.802 ± 0.2	−3.630 ± 0.20	−8.154(4)	⋯	⋯	−3.585(4)	−8.154(4)
Gl 206B	3	−4.234 ± 0.2	−5.438 ± 0.2	−2.292 ± 0.20	−4.922(4)	⋯	⋯	−2.304(4)	−4.922(4)
Gl 213	⋯	⋯	⋯	⋯	−0.315(8)	0.670(4)	−0.303(4)	0.215	−0.311(12)
Gl 232	⋯	⋯	⋯	⋯	−0.36(4)	⋯	⋯	0.163(14)	−0.36(4)
Gl 234A	⋯	⋯	⋯	⋯	−5.88(1)	⋯	−4.797(32)	−3.055(32)	−4.830(33)
Gl 268AB	⋯	⋯	⋯	⋯	−4.66(2)	⋯	⋯	−2.152(16)	−4.66(2)
Gl 268A	⋯	⋯	⋯	⋯	−5.95(1)	⋯	⋯	−2.38(1)	−5.95(1)
Gl 268B	⋯	⋯	⋯	⋯	−3.37(1)	⋯	⋯	−2.34(1)	−3.37(1)
Gl 273	5	−0.357 ± 0.03	−0.538 ± 0.03	0.207 ± 0.02	−0.380(21)	0.836(17	−0.497(17)	0.189(18)	−0.432(38)
Gl 277B	⋯	⋯	⋯	⋯	−6.61(6)	6.149(2)	−4.331(2)	−1.977(7)	−6.040(8)
Gl 285	⋯	⋯	⋯	⋯	−16.05(12)	28.48(4)	−27.26(4)	−7.003(15)	−16.04(12)
Gl 299	1	⋯	⋯	0.202 ± 0.02	−0.375(4)	⋯	⋯	0.185(15)	−0.375(4)
Gl 300	1	−0.592 ± 0.09	−0.784 ± 0.09	0.143 ± 0.02	−0.654(5)	⋯	⋯	0.167(2)	−0.654(5)
Gl 317	⋯	⋯	⋯	⋯	⋯	1.251(4)	−0.641(4)	0.281	−0.641(4)
Gl 319B	1	−0.181 ± 0.08	−0.292 ± 0.08	0.295 ± 0.02	−0.236(1)	⋯	⋯	0.295(1)	−0.236(1)
Gl 324B	⋯	⋯	⋯	⋯	−0.73(1)	⋯	⋯	0.249	−0.73(1)
Gl 375AB	⋯	⋯	⋯	⋯	⋯	2.560(2)	−1.513(2)	−4.75	−1.513(2)
Gl 375A	1	−9.234 ± 0.2	−8.184 ± 0.2	−3.722 ± 0.2	−8.709(1)	⋯	⋯	−3.722	−8.709(1)
Gl 375B	1	−7.352 ± 0.2	−8.578 ± 0.2	−3.746 ± 0.2	−7.965(1)	⋯	⋯	−3.746	−7.965(1)

Table 6
(Continued)

Star	No. meas.	FEROS Ca II H EW (Å)	FEROS Ca II K EW (Å)	FEROS H_α EW (Å)	Mean Ca II EW (Å)	S_{HK}	Mean Ca II EW[a] (Å)	H_α EW (Å)	Mean Ca II EW (Å)
Gl 398	7	−8.122 ± 0.2	−10.174 ± 0.2	−3.617 ± 0.2	−8.573(9)	⋯	⋯	−3.617(7)	−8.573(9)
Gl 402	5	−0.451 ± 0.05	−0.673 ± 0.05	0.209 ± 0.02	−0.699(15)	1.279(4)	−0.658(4)	0.175(21)	−0.690(19)
Gl 431	1	−7.620 ± 0.2	−8.782 ± 0.2	−4.017 ± 0.2	−8.790(3)	⋯	⋯	−4.519(3)	−8.790(3)
Gl 445	⋯	⋯	⋯	⋯	−0.179(14)	0.566(4)	−0.195(4)	0.247(13)	−0.183(18)
Gl 447	1	−0.541 ± 0.05	−0.824 ± 0.05	0.187 ± 0.02	−0.452(13)	0.875(4)	−0.417(4)	0.176(10)	−0.444(17)
Gl 469	⋯	⋯	⋯	⋯	−0.47(8)	⋯	⋯	0.189(7)	−0.47(8)
Gl 486	1	−0.248 ± 0.05	−0.314 ± 0.05	0.195 ± 0.02	−0.237(18)	0.648(5)	−0.284(5)	0.175(13)	−0.242(20)
Gl 487	⋯	⋯	⋯	⋯	−1.125	⋯	⋯	−0.251(54)	−1.125
Gl 490B	⋯	⋯	⋯	⋯	⋯	⋯	−7.35(1)	−4.39(1)	−7.35(1)
Gl 512B	5	−0.415 ± 0.03	−0.526 ± 0.03	0.315 ± 0.02	−0.470(5)	⋯	⋯	0.315(5)	−0.470(5)
Gl 520C	⋯	⋯	⋯	⋯	⋯	⋯	−7.65(1)	−4.55(1)	−7.65(1)
Gl 545	⋯	⋯	⋯	⋯	⋯	⋯	⋯	0.192(3)	⋯
Gl 553.1	3	−0.148 ± 0.03	−0.204 ± 0.03	0.186 ± 0.02	−0.178(15)	0.501(4)	−0.214(4)	0.174(11)	−0.186(19)
Gl 555	2	−0.384 ± 0.03	−0.573 ± 0.03	0.191 ± 0.02	−0.390(14)	0.904(8)	−0.576(8)	0.157(21)	−0.458(22)
Gl 568AB	⋯	⋯	⋯	⋯	⋯	⋯	⋯	−0.203(1)	⋯
Gl 592	6	−0.190 ± 0.05	−0.234 ± 0.05	0.212 ± 0.02	−0.212(6)	⋯	⋯	0.212(6)	−0.212(6)
Gl 609	5	−0.269 ± 0.09	−0.401 ± 0.09	0.211 ± 0.02	−0.401(8)	⋯	⋯	0.206(11)	−0.401(8)
Gl 630.1	⋯	⋯	⋯	⋯	⋯	⋯	−8.51(1)	−5.00(1)	−8.51(1)
Gl 643AB	2	−0.178 ± 0.05	−0.264 ± 0.05	0.210 ± 0.02	−0.197(3)	⋯	⋯	0.176(24)	−0.197(3)
Gl 644B	1	−0.213 ± 0.1	−0.419 ± 0.1	0.201 ± 0.02	−0.316(1)	⋯	⋯	0.201(1)	−0.316(1)
Gl 669A	2	−8.560 ± 0.2	−10.86 ± 0.2	−5.887 ± 0.2	−5.866(8)	4.431(2)	−2.923(2)	−2.696(6)	−5.277(10)
Gl 682	1	−0.399 ± 0.08	−0.552 ± 0.08	0.183 ± 0.02	−0.476(1)	⋯	⋯	0.183(1)	−0.476(1)
Gl 695B	⋯	⋯	⋯	⋯	⋯	⋯	⋯	0.283	⋯
Gl 699	1	−0.445 ± 0.03	−0.370 ± 0.03	0.249 ± 0.02	−0.411(15)	0.761(71)	−0.353(71)	0.222(33)	−0.363(86)
Gl 720B	⋯	⋯	⋯	⋯	−0.29	⋯	⋯	0.253	−0.29
Gl 725B	⋯	⋯	⋯	⋯	−0.305(15)	0.651(22)	−0.292(22)	0.267	−0.298(37)
Gl 729	6	−4.375 ± 0.2	−5.110 ± 0.2	−1.685 ± 0.2	−4.743(6)	8.967(4)	−6.811(4)	−1.793(17)	−5.570(10)
Gl 732A	3	−3.120 ± 0.2	−3.803 ± 0.2	−1.141 ± 0.2	−3.462(3)	⋯	⋯	−1.141(3)	−3.462(3)
Gl 781.1B	1	−3.994 ± 0.2	−4.938 ± 0.2	−2.634 ± 0.2	−4.466(1)	⋯	⋯	−2.967(2)	−4.466(1)
Gl 791.2A	⋯	⋯	⋯	⋯	⋯	⋯	−7.775(3)	−4.615(3)	−7.775(3)
Gl 812A	4	−2.555 ± 0.1	−3.073 ± 0.1	−1.553 ± 0.2	−2.814(4)	⋯	⋯	−2.030(6)	−2.814(4)
Gl 860B	⋯	⋯	⋯	⋯	⋯	3.304(2)	−2.055(2)	−2.098(3)	−2.055(2)
Gl 865AB	1	−7.308 ± 0.2	−8.846 ± 0.2	−2.688 ± 0.2	−6.816(2)	⋯	⋯	−2.369(2)	−6.816(2)
Gl 865A	⋯	⋯	⋯	⋯	⋯	⋯	−4.88(1)	−3.10(1)	−4.88(1)
Gl 865B	⋯	⋯	⋯	⋯	⋯	⋯	−8.70(1)	−5.10(1)	−8.70(1)
Gl 867B	⋯	⋯	⋯	⋯	⋯	⋯	−7.722(2)	−4.587(2)	−7.722(2)
Gl 873A	⋯	⋯	⋯	⋯	−7.70(2)	12.525(4)	−10.171(4)	−3.784(17)	−9.347(6)
Gl 876A	5	−0.348 ± 0.01	−0.711 ± 0.01	0.200 ± 0.02	−0.448(137)	1.022(119)	−0.503(119)	0.197(52)	−0.473(256)
Gl 896AB	⋯	⋯	⋯	⋯	⋯	⋯	−6.43(34)	−3.91(34)	−6.43(34)
Gl 896B	⋯	⋯	⋯	⋯	⋯	5.490(2)	−9.156(9)	−6.143(7)	−9.156(9)
G 97-52B	⋯	⋯	⋯	⋯	⋯	⋯	⋯	−0.126(1)	⋯
LHS 1723	⋯	⋯	⋯	⋯	⋯	⋯	−0.68(1)	−0.9(1)	−0.68(1)

Note. Results were obtained using FEROS spectra as well as a compilation of data published in the literature. When the H_α EW is known but with no observations of the Ca II EW, we derived the Ca II EW according to the H_α EW–Ca II EW correlation (see Figure 8).
[a] Inferred from the H_α EW-Ca II EW correlation.

(This table is available in machine-readable form.)

Therefore in what follows, the least squares fits that we will present refer only to stars in the unsaturated regime. In this regime, the observations show that there exist stars of both low (dM) and high (dMe) activity, so the sample provides access to a range of "dynamo strengths." In contrast, in the saturated regime, only high-activity stars (dMe) are present.

In the regime of our unsaturated stars, we also performed heteroscedastic and homoscedastic linear LSFs to the separate sub-samples of low-activity dM3 and high-activity dM3e stars respectively (see Table 1). The heteroscedastic linear LSF to the dM3 low-activity stars (all of which are in the unsaturated regime) yields:

$$F_{\mathrm{Ca\,II}} = 2.33 \pm 1.10 \times 10^5 \times (P/\sin i)^{-0.837\pm0.20}. \quad (19)$$

Therefore, the gradient of the RAC for the low-activity stars is again much shallower than that of the combined sample of low+high-activity stars, and by more than 3σ. Therefore, the linear LSF to the combined sample may be somehow inadequate. We plot the linear LSF to the low-activity sub-sample also in Figure 8 (dotted-dashed line).

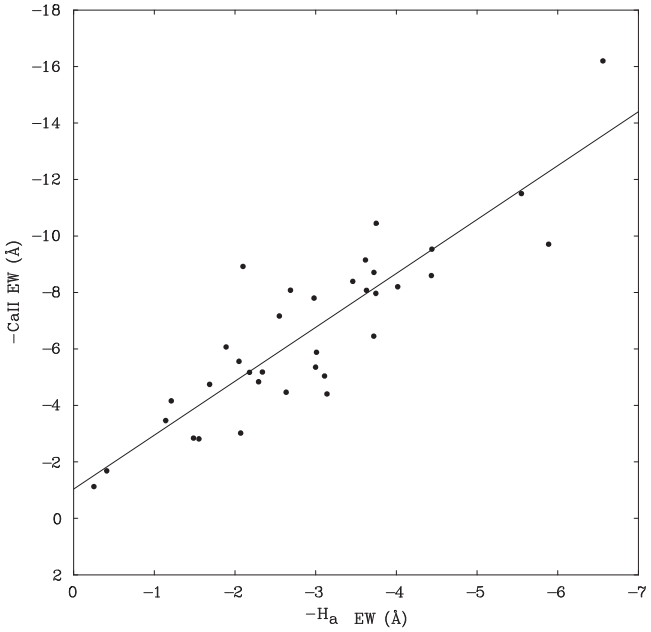

Figure 9. Correlation between the mean EW of the Ca II resonance doublet and the H_α EW for stars with spectral sub-type dM4e. The solid line is the linear LSF to the data.

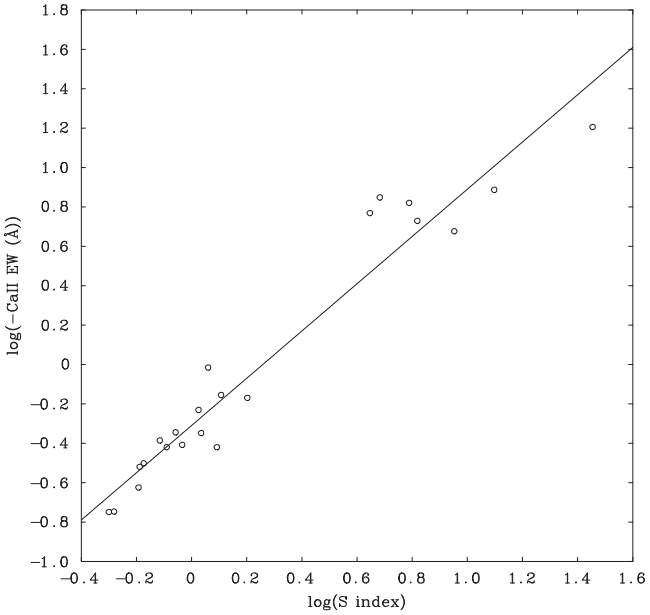

Figure 10. Correlation between the mean EW of the Ca II resonance doublet and the Ca II Mount Wilson S index for stars with spectral sub-type dM4. The solid line is the linear LSF to the data.

The homoscedastic linear LSF to the dM3 low-activity stars yields:

$$F_{\mathrm{Ca\,II}} = 3.09 \pm 1.58 \times 10^5 \times (P/\sin i)^{-0.93\pm0.22}. \quad (20)$$

Both fits yield comparable results within errors. The χ^2 for these fits are 0.039 and 0.047 respectively. Both fits are highly statistically significant at a 99.9% confidence level. Once again, we see that the slopes of the RAC among low-activity dM3 stars (−0.84, −0.93) are significantly shallower (by more than 3σ) than the slopes of the RAC for the combined sample of high and low-activity dM3 stars (−2.02, −2.08).

Turning now to the high-activity dM3e stars in the unsaturated regime, we find that the heteroscedastic linear LSF yields:

$$F_{\mathrm{Ca\,II}} = 1.60 \pm 1.20 \times 10^6 \times (P/\sin i)^{-1.041\pm0.58}. \quad (21)$$

In contrast to the results we obtained for the K4, K6, and M2 samples, this time for the dM3e sub-sample of unsaturated stars, the slope of the RAC is shallower than that of the combined sample of (unsaturated) low+high-activity stars. It seems that at the TTCC, the slope of the RAC for (unsaturated) high-activity stars is falling significantly to a value of about −1. Although there remains some uncertainty on our fit for dM3e stars (because we have only eight stars in the unsaturated regime, and with a significant scatter), we shall see in the next subsection that this decrease in the steepness of the slope is confirmed in our (unsaturated) dM4e sub-sample and is significant above the 3σ level (23 stars). Our M4 sample also confirms that, the slope of the RACs for the high-activity (unsaturated) sub-samples has fallen below the slope of the combined dM+dMe samples.

We have also performed LSFs to the full sub-sample of dM3e stars (unsaturated+saturated). We give the results of the fits in Table 1 (dM3e+sat). The slope for the full sub-sample has fallen to −0.39, which is considerably smaller than the value of −1.04 we found above. However, this presents us with the idea that at the TTCC, the slope of the RAC for dM3e stars is of the same order than that of the slope for the low-activity dM3 stars (see Section 3.7.6).

The relative invariance of the RAC slopes that we have obtained for the linear LSF to the low-activity stars in our five stellar samples gives an important degree of credibility to our results. It is important to note that all of our low-activity stars have been found to lie in the unsaturated regime of the RAC, i.e., in the regime where (we believe) dynamo theory can best be tested. To the extent that the slope of the RAC is determined (in the unsaturated regime) by the physical properties of a dynamo, our results suggest that there may exist only one dynamo regime for the low-activity stars from dK4 to dM4 within errors (see Section 3.7.2). The parameter $\frac{R}{\delta}$ is 18.28 for the high-activity star sub-sample and 21.77 for the low-activity star sub-sample. Therefore, the parameter $\delta = \frac{\langle \mathrm{error} \rangle}{\sqrt{n}}$, which is a normalized estimate of the mean error on the measurements, is much smaller than the period domains of the RACs in both cases. Hence, these LSFs should be relatively well established, which corresponds to the high statistical significances we obtain (Table 1). However, these results may still be preliminary because the domains of the RACs are relatively small compared to the typical uncertainties on individual measures as highlighted by the referee.

There is the possibility that there exist two different dynamo regimes for dK, dM and dKe, dMe, respectively throughout the spectral range we investigate. Note that, in contrast to the low-activity dK and dM stars, the dynamo regimes in high-activity dKe and dMe stars vary with spectral type, especially at the TTCC. Might these changes be an indication that the dynamo mechanisms undergo a change at the TTCC, perhaps from an α–Ω dynamo to an α^2 type of dynamo?

There tends to be more and more high-activity, relatively slow rotators when we move to the spectral sub-types dM3 and dM4, which questions the validity of a single RAC for the combined samples at these spectral types. Given the consistency of the results we have obtained for the slopes of the RAC for the low-activity stars for our five spectral sub-types, it is

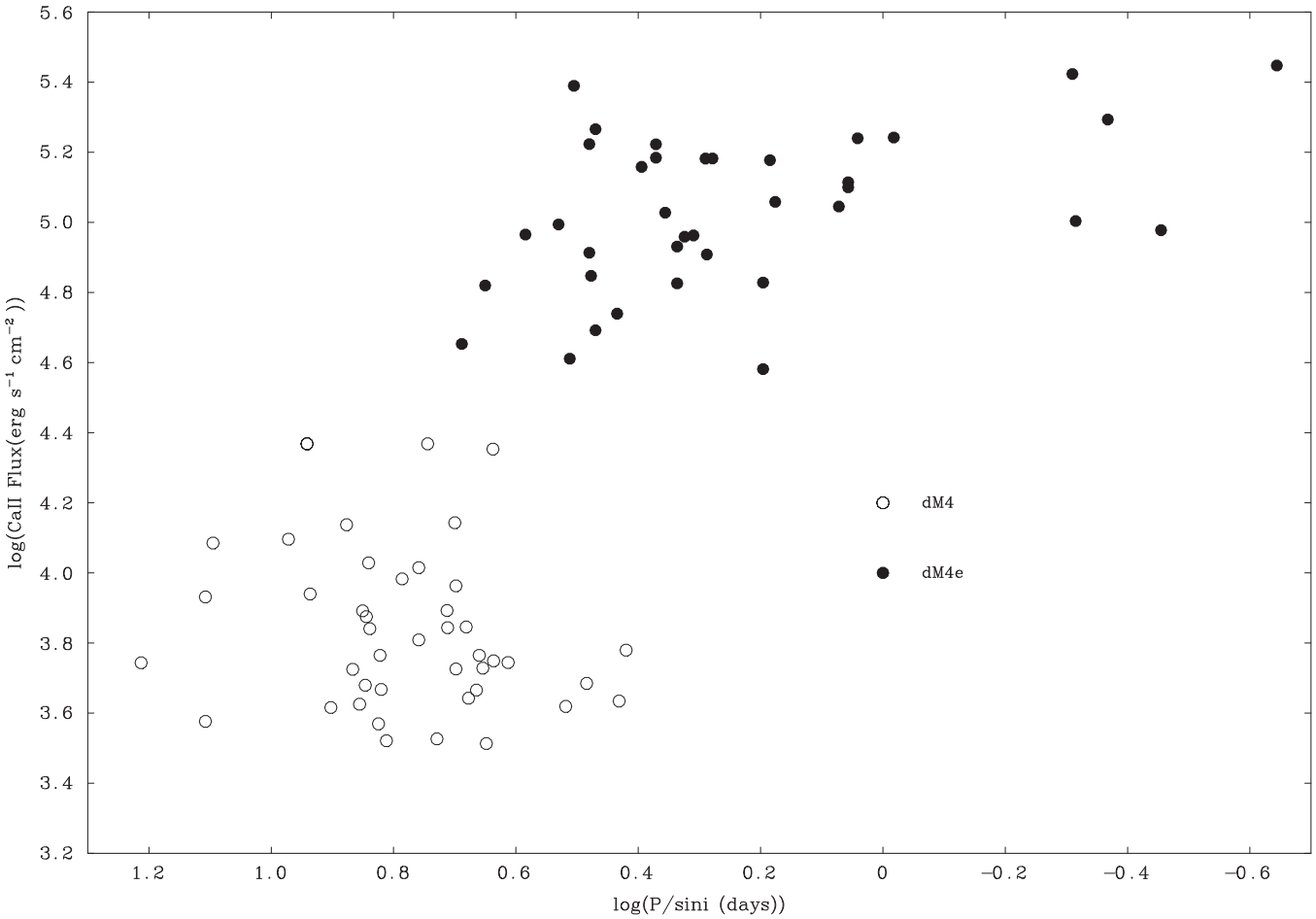

Figure 11. Correlation between the mean EW of the Ca II resonance doublet and $\log(P/\sin i)$ for stars with spectral sub-type dM4. Filled dots: dM4e. Hollow circles: dM4 stars.

possible that a single dynamo mechanism may apply to all low-activity stars in our sample. However, we arrive at a different conclusion regarding the dynamo mechanism among the high-activity stars. At the TTCC and beyond, we propose that high-activity stars may switch to a different dynamo mechanism (see Section 3.7).

3.6. The RAC in M4 Dwarfs

Considering that, in our previous study of the RAC in dM4 stars, we had only a couple of dozen stars (Houdebine 2012a, Paper XVII), we decided to compile all available measures of $v \sin i$ published in the literature (see Paper I). With our own measures, we obtained $v \sin i$ measures for 106 dM4 stars (Paper I) from our initial list of 395 dM4 stars. Our dM4 stars in this study were selected according to their $(R–I)_C$ color, within the range [1.500;1.700]. This range is somewhat larger than the one used in Paper XVII in order to have more targets.

In order to obtain the RAC for dM4 stars, we also compiled the Ca II resonance doublet and the H_α line EW and fluxes from the literature. We give this compilation of data in Table 6. The data were collected from the following authors: Giampapa & Liebert (1986), Stauffer & Hartmann (1986), Fleming & Giampapa (1989), Herbst & Miller (1989), Young et al. (1989), Hawley et al. (1996), Delfosse et al. (1998), Gizis et al. (2002), Mohanty & Basri (2003), Wright et al. (2003), Rauscher & Marcy (2006), Morales et al. (2008), Walkowicz & Hawley (2009), Browning et al. (2010), Isaacson & Fischer (2010), Houdebine (2012b), Reiners et al. (2012), and Pace (2013). In addition to this data, we also measured the Ca II and H_α EW from FEROS spectra from the ESO archive for 47 dM4 stars. We give the results in Table 6. Together with the measurements from Paper XVIII, this allows us to derive a correlation between the Ca II EW and the H_α EW for dM4e stars. We show this correlation in Figure 9. Although there is more scatter in this sample than in our dM3 star sample, we have a relatively good correlation with a correlation coefficient of 0.877 for 35 measures (see Table 1). This correlation is significant at a confidence level better than 99.8%. The LSF to this data gives:

$$\mathrm{EW_{Ca\,II}} = 1.909 \pm 0.18 \times \mathrm{EW_{H_\alpha}} - 1.035 \pm 0.58. \quad (22)$$

Equation (22) allows us to obtain an estimate of the Ca II EW when we have only the H_α line EW available for dM4e stars. Similarly, we compiled many measures of the Mount Wilson S index (Table 6). We show the empirical correlation between the Ca II EW and the S index in Figure 10. Again, we obtain a relatively good correlation between the two parameters, with a correlation coefficient of 0.970 for 22 data points (see Table 1). The relationship between the Ca II EW and the S index is:

$$\mathrm{EW_{Ca\,II}} = 0.4898 \pm 0.047 \times S^{1.20 \pm 0.07}. \quad (23)$$

All these compilations of data now allow us to compute the Ca II surface fluxes (Table 7). We show the Ca II surface fluxes as a function of $P/\sin i$ for our dM4 stellar sample in

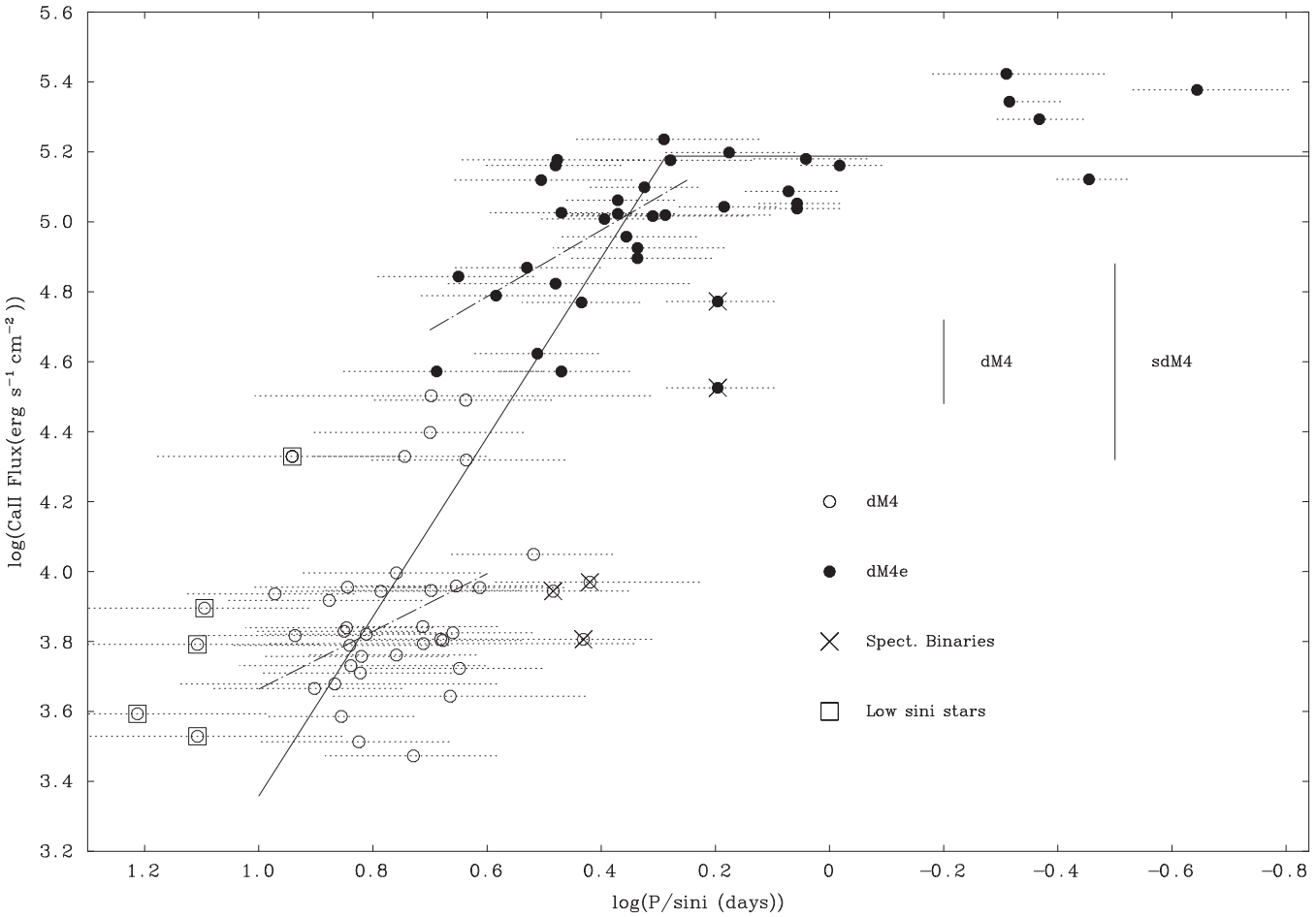

Figure 12. Correlation between the logarithm of the mean surface fluxes of the Ca II resonance doublet corrected for metallicity effects and $\log(P/\sin i)$ for stars with spectral sub-type dM4. Notice the onset of saturation for stars with $\log(P/\sin i) \leqslant 0.2$. LSFs have been obtained for the stars in the unsaturated regime as follows. Solid line, heteroscedastic linear LSF; separated dotted-dashed lines, the heteroscedastic linear LSF to the low-activity dM4 and to the high-activity dM4e subsamples. We show in the center-right of the figure estimates of the uncertainties on the Ca II mean surface fluxes due to the corrections for metallicity effects, for dwarfs and subdwarfs.

Figure 11. One can see in this diagram that the scatter is very large, and is similar to (or even worse than) the raw correlation for dM3 stars. It appears that the scatter increases from spectral sub-types dM2 to dM4. However, there is a parameter that plays a role in the scatter in Figure 11: the $(R–I)_C$ range for our dM4 sample ([1.500:1.700]) spans 0.2 dex, whereas for our dM2 and dM3 samples, it spans 0.132 dex. This larger range in our selected targets contributes to the larger scatter observed in Figures 11 and 12. In Figure 11, it is noteworthy that there is no overlap in Ca II fluxes between the low-activity dM4 stars (up to $\log(F_{HK} = 4.4)$ and the high-activity dM4e stars ($\log(F_{HK} \geqslant 4.6$): there is a clear gap in the fluxes, although the two groups overlap in their rotation periods. The dM3 stars do not show this clean separation between dM and dMe (Figure 8). The dM2 stars also show some separation (Figure 5), but it is not as clean as for dM4 stars.

Considering the good correction we had for metallicity in dM2 stars, we decided to compile all the metallicities published for our initial selection list of 395 dM4 stars, and try to obtain a metallicity–radius correlation for these stars (see Paper I). We found metallicities from the literature for 179 dM4 stars. Data for M4 stars that have been corrected for metallicity can be found in Figure 12 and Table 7.

In Figure 12, we show the RAC corrected for metallicity effects for dM4 stars. The scatter is reduced compared to the raw data in Figure 11, but there remains a significant scatter among both dM4 and dM4e stars. The corrected correlation is not as good as for dM2 stars in spite of the relatively good statistics we have on the Ca II surface fluxes.

We also observe among our sample of dM4 stars a subsample of relatively fast rotating, low-activity stars. Again, as in the case of dM2 and dM3 stars, we believe that these stars are unresolved spectroscopic binaries. We also found a few stars with possibly low $\sin i$ (see Figure 12).

We find that when we apply the linear heteroscedastic and homoscedastic LSFs to the combined dM4+dM4e stars in the unsaturated regime, the gradients are very steep, steeper even than what we found for our dM2 and dM3 stellar samples. We also find that dM4 stars rotate much faster than dM2 and dM3 stars. The change in Ca II flux between dM4 and dM4e stars is very abrupt, as already noticed in Figure 11, a difference of only 0.1 in the $\log(P/\sin i)$. Our data suggest that saturation in our dM4 sample occurs at about $P/\sin i \sim 1.8$ days. This agrees with the values found in previous studies. Specifically, for stars in the unsaturated regime, i.e., for $P/\sin i \geqslant 1.8$ days we obtain the following heteroscedastic linear LSF for the stars

Table 7
The Values of $v \sin i$, $P/\sin i$ and [M/H] Compiled from Paper I for Our Targets in Our List of dM4 Stars

Star	$v \sin i$ (km s^{-1})	$P/\sin i$ (days)	[M/H] (dex)	[M/H][a] (dex)	Ca II EW (Å)	F_{HK} (10^4 erg s^{-1} cm^{-2})	F_{HK}[b] (10^4 erg s^{-1} cm^{-2})
GJ 1001A	1.15	12.81−5.66+18.02	⋯	+0.047	−0.235	0.377	0.338
GJ 1005AB	3.00	3.41−0.96+1.44	−0.47	−0.210	⋯	⋯	⋯
GJ 1034	4.50	2.05−0.61+0.79	−0.38	−0.275	⋯	⋯	⋯
GJ 1065	4.00	2.70−0.65+0.88	0.20	−0.172	−0.25	0.431	0.640
GJ 1105	2.00	6.93−2.28+4.24	0.24	+0.022	−0.62	1.068	0.615
GJ 1129	3.00	4.62−1.94+2.91	0.05	+0.022	−0.328	0.463	0.440
GJ 1134	4.10	3.11−0.74+1.00	−0.16	−0.036	⋯	⋯	⋯
GJ 1207	10.70	1.18−0.21+0.25	−0.15	−0.042	−7.098	11.10	12.23
GJ 1254	4.00	5.39−1.41+1.90	0.22	+0.122	⋯	⋯	⋯
GJ 1289	2.60	4.34−1.27+2.04	0.12	−0.137	−1.680	2.256	3.093
GJ 2036B	19.8	0.429−0.07+0.08	⋯	−0.327	−14.49	19.66	19.66
GJ 2069A	6.43	3.20−0.98+1.34	0.27	+0.102	−16.91	24.53	13.17
GJ 3092B	3.80	4.87−1.24+1.70	⋯	+0.064	⋯	⋯	⋯
GJ 3149B	4.00	3.02−1.26+1.71	0.09	−0.078	−5.647	8.193	6.660
GJ 3283B	6.00	1.94−0.67+0.93	⋯	−0.111	−6.372	8.101	10.46
GJ 3322	7.68	9.20−4.57+5.94	⋯	⋯	−10.58	16.30	16.30
GJ 3398	4.00	3.11−0.81+1.10	⋯	−0.054	⋯	⋯	
GJ 3631AB	19.10	0.49−0.16+0.18	−0.64	−0.268	−19.29	26.51	26.51
GJ 3707	2.0	7.36−3.53+6.55	0.35	+0.047	−0.341	0.531	0.477
GJ 3789	56.50	0.227−0.07+0.07	0.07	−0.033	−19.31	28.02	23.85
GJ 3801	4.00	3.67−0.88+1.20	0.14	+0.047	⋯	⋯	⋯
GJ 3804	2.50	6.64−2.04+3.32	0.09	+0.055	−0.299	0.582	0.513
GJ 3873	4.00	6.90−2.89+3.91	0.11	+0.245	−0.465	0.693	0.538
GJ 3900	3.00	5.15−2.95+4.43	0.46	+0.050	−0.453	0.698	0.622
GJ 3907	2.50	5.39−1.91+3.11	0.06	+0.006	⋯	⋯	⋯
GJ 4020B	16.16	1.10−0.24+0.27	⋯	+0.060	−12.94	17.38	15.14
GJ 4030	4.50	3.90−1.14+1.49	−0.04	+0.059	⋯	⋯	⋯
GJ 4049B	2.50	3.81−1.16+1.89	−0.13	−0.255	⋯	⋯	⋯
GJ 4063AB	2.17	4.99−2.93+5.16	−0.54	−0.169	−0.533	0.918	3.183
GJ 4108	4.50	2.04−0.60+0.78	⋯	−0.278	⋯		
GJ 4248	1.58	7.75−2.71+6.04	⋯	−0.066	⋯	⋯	⋯
GJ 4333	2.50	8.64−2.51+4.09	0.25	+0.123	−0.574	0.871	0.656
GJ 4338B	14.50	1.53−0.29+0.33	⋯	+0.134	−10.95	15.05	11.05
GJ 4378A	4.00	4.88−1.69+2.29	⋯	+0.081	−2.839	4.501	3.735
Gl 15B	1.90	5.01−1.57+3.01	−0.95	−0.255	−0.921	1.390	2.500
Gl 46	1.29	16.32−6.60+18.1	0.15	+0.112	−0.295	0.554	0.392
Gl 54.1	2.50	3.00−0.89+1.45	−0.33	−0.402	−6.318	7.039	15.05
Gl 84.1B	2.00	12.45−4.27+7.94	−0.18	+0.190	−0.625	1.217	0.786
Gl 105B	2.45	6.61−1.95+3.21	−0.09	+0.053	−0.330	0.465	0.572
Gl 166C	2.90	4.47−1.17+1.78	−0.10	−0.024	−4.921	6.607	6.982
GL 169.1A	1.94	7.80−2.44+4.62	0.29	+0.049	⋯	⋯	⋯
GL 179	2.50	7.53−2.35+3.84	0.22	+0.065	−0.695	1.372	0.827
GL 203	4.00	2.67−0.68+0.92	−0.23	−0.179	−0.121	0.239	0.406
Gl 206A	6.37	1.95−0.62+0.84	0.19	−0.054	−8.154	15.21	17.22
Gl 206B	6.11	2.04−0.65+0.90	0.19	−0.054	−4.922	9.179	10.39
GL 213	2.70	4.76−1.29+2.03	−0.16	−0.030	−0.311	0.439	0.635
GL 232	3.10	3.05−0.80+1.18	−0.25	−0.259	−0.36	0.484	0.879
GL 234A	4.73	2.72−0.57+0.74	⋯	−0.030	−4.830	5.490	5.883
GL 268A	10.65	1.57−0.32+0.38	0.16	+0.056	−5.95	6.736	5.921
GL 268B	10.65	1.57−0.32+0.38	0.16	+0.056	−3.37	3.815	3.353
GL 273	2.36	6.99−1.91+3.22	−0.08	+0.055	−0.432	0.750	0.902
Gl 277B	6.40	3.39−0.87+1.19	0.10	+0.125	−6.040	9.867	7.399
GL 285	6.16	2.95−0.71+0.98	0.24	+0.062	−16.04	18.45	10.62
GL 299	2.96	3.30−0.90+1.35	−0.43	−0.239	−0.375	0.416	1.120
GL 300	3.00	5.16−1.34+2.01	0.20	+0.050	−0.654	0.781	0.696
GL 317	2.50	9.37−2.56+4.18	−0.10	+0.160	−0.641	1.248	0.863
GL 319B	3.70	7.17−1.82+2.53	0.04	+0.223	−0.236	0.422	0.385
GL 324B	2.36	6.11−1.90+3.20	0.42	+0.039	−0.73	0.961	0.878
GL 375A	10.0	2.35−0.48+0.58	⋯	+0.161	−8.709	16.71	11.53
GL 375B	10.0	2.35−0.48+0.58	⋯	+0.161	−7.965	15.29	10.55
GL 402	2.40	5.74−1.65+2.75	0.12	+0.019	−0.690	1.035	0.991
Gl 431	20.36	0.960−0.15+0.17	⋯	+0.081	−8.790	17.47	14.50
Gl 445	2.25	6.48−1.90+3.28	−0.30	+0.044	−0.183	0.332	0.662

Table 7
(Continued)

Star	$v \sin i$ (km s^{-1})	$P/\sin i$ (days)	[M/H] (dex)	[M/H][a] (dex)	Ca II EW (Å)	F_{HK} (10^4 erg s^{-1} cm^{-2})	F_{HK}[b] (10^4 erg s^{-1} cm^{-2})
Gl 447	2.20	4.51−1.33+2.32	−0.04	−0.230	−0.444	0.535	0.909
GL 458BC	5.40	1.74−0.45+0.65	−0.53	−0.262	...	...	...
Gl 469	1.58	12.81−4.94+11.0	0.14	+0.095	−0.47	0.854	0.619
GL 486	2.25	7.99−2.37+4.10	−0.05	+0.061	−0.242	0.413	0.463
Gl 487A	1.65	8.74−3.05+6.54	−0.04	+0.039	−1.125	2.335	2.134
Gl 487B	1.22	11.87−4.79+14.05	−0.04	+0.039	−1.125	2.335	2.134
Gl 487C	2.60	5.55−1.55+2.47	−0.04	+0.039	−1.125	2.335	2.134
GL 490B	8.60	2.27−0.56+0.71	0.07	+0.081	−7.35	10.66	9.073
GL 512B	4.00	2.63−0.94+1.27	0.12	−0.190	−0.470	0.602	0.932
GL 520C	8.20	1.50−0.35+0.45	−0.14	−0.063	−7.65	11.44	15.79
GL 544B	4.66	2.44−0.80+1.03	−0.13	−0.129	...	...	...
GL 545	4.00	3.07−1.08+1.46	−0.12	−0.063	...	...	...
Gl 553.1	2.50	6.68−2.04+3.33	0.26	+0.056	−0.186	.0.371	0.326
GL 555	2.60	5.74−1.58+2.53	0.20	+0.048	−0.458	0.644	0.577
GL 568AB	4.00	4.78−1.18+1.60	0.45	+0.073	...	...	...
GL 592	3.00	5.36−1.53+2.29	0.14	+0.053	−0.212	0.336	0.297
GL 609	3.00	4.57−1.25+1.88	−0.06	+0.017	−0.401	0.582	0.668
GL 630.1AB	27.50	0.484−0.09+0.10	−0.34	−0.003	−8.51	10.09	22.07
GL 643AB	2.73	4.45−1.26+1.97	−0.21	−0.074	−0.197	0.326	0.529
GL 644B	2.73	4.10−1.18+1.84	−0.21	−0.144	−0.316	0.555	0.900
Gl 669A	6.30	3.84−1.01+1.39	0.08	+0.176	−5.277	9.231	6.155
GL 682	3.00	4.80−1.22+1.83	0.11	+0.039	−0.476	0.701	0.641
GL 695B	7.33	3.03−0.72+0.95	...	+0.136	...		
Gl 699	2.02	4.99−1.49+2.75	−0.40	−0.220	−0.363	0.532	0.883
GL 720B	2.30	7.02−2.06+3.52	−0.16	+0.053	−0.29	0.478	0.691
GL 725B	5.09	4.33−1.42+2.12	−0.57	−0.155	−0.298	0.561	2.084
GL 729	4.72	2.11−0.41+0.53	−0.14	−0.227	−5.570	9.099	12.56
GL 732A	...	...	−0.01	+0.056	−3.462	5.489	5.617
GL 781.1B	9.20	2.17−0.56+0.70	−0.07	+0.090	−4.466	6.700	7.872
GL 783.2B	1.76	8.14−3.48+7.09	−0.15	+0.036	...	...	...
GL 791.2A	31.90	0.351−0.05+0.05	0.06	−0.144	−7.775	9.500	13.23
GL 812A	10.00	2.95−0.71+0.87	0.12	+0.284	−2.814	4.922	3.734
GL 860B	4.05	3.25−0.71+0.96	−0.13	−0.012	−2.055	4.084	4.198
Gl 865A	7.09	1.90−0.53+0.71	−0.10	+0.006	−8.70	15.22	15.01
Gl 865B	6.20	2.17−0.64+0.88	−0.10	+0.006	−4.88	8.536	8.419
Gl 867B	7.01	2.48−0.54+0.72	0.15	+0.059	−7.722	14.40	10.19
GL 873A	5.99	3.02−0.70+0.98	−0.05	+0.062	−9.347	16.73	14.50
GL 876A	2.57	7.09−1.95+3.13	...	+0.062	−0.473	0.779	0.675
GL 896A	15.81	1.14−0.18+0.21	0.10	+0.062	−9.470	13.02	11.29
GL 896B	15.81	1.14−0.18+0.21	0.10	+0.062	−9.156	12.59	10.92
LHS 2795	6.40	(2.38)	...	...	...	...	...
LHS 3279	30.0	(0.508)	...	...	...	...	...
G 97-52B	4.00	(3.81)	...	...	...	...	...

Notes. We also give the Ca II EW (from the compilation of Table 6), surface fluxes F_{HK}, and the surface fluxes corrected for the metallicity effects.
[a] Metallicity from the radius–metallicity relation.
[b] Surface flux corrected for metallicity effects.

(This table is available in machine-readable form.)

in our combined dM4+dM4e sample:

$$F_{\mathrm{Ca\,II}} = 8.38 \pm 2.05 \times 10^5 \times (P/\sin i)^{-2.564 \pm 0.19}. \quad (24)$$

The gradient in Equation (24) (-2.564 ± 0.19) is significantly steeper than the gradient that we determined for our dK6 (-1.047 ± 0.042: Table 1) and dM2 stars (-1.575 ± 0.058: Table 1), and is also steeper than the gradient for our dM3 stars (-2.020 ± 0.11: Table 1). This confirms that the slope of the linear LSFs increases in absolute value when the spectral type increases from dK4 to dM4. This increase is particularly marked at the TTCC (M3) and beyond.

For $P/\sin i \geqslant 1.8$ days we obtain the following homoscedastic linear LSF for the stars in our combined dM4+dM4e sample:

$$F_{\mathrm{Ca\,II}} = 7.94 \pm 2.05 \times 10^5 \times (P/\sin i)^{-2.526 \pm 0.13}. \quad (25)$$

The gradient in Equation (25) (-2.526 ± 0.18) is very close to that determined for the heteroscedastic linear fit (-2.564 ± 0.19: Table 1). As a whole, we find comparable results from the heteroscedastic and homoscedastic linear fits, suggesting that the errors on the measures do not play a large role in the determination of the linear fits (Table 1).

In Figure 12 we observe a flattening ("saturation") for the fastest rotating dM4e stars for $P/\sin i < 1.6$ days. This is a range in periods where saturation is expected to occur (see Section 1.4). Although our data set is not yet complete enough

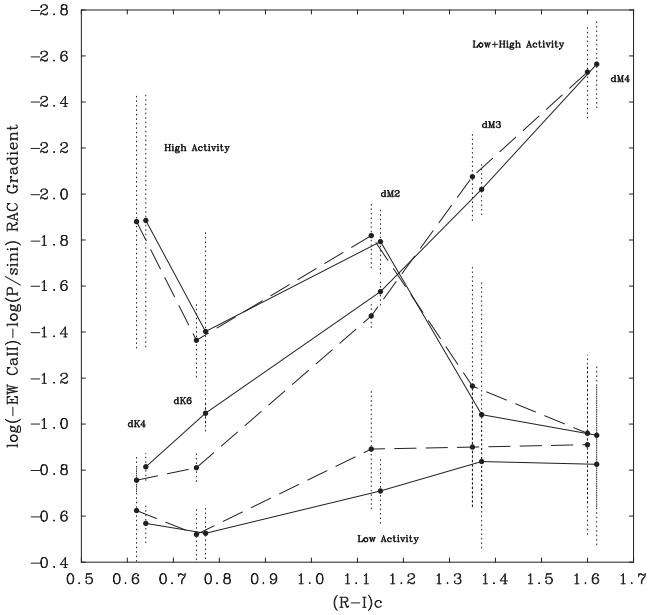

Figure 13. Values of the slopes of the heteroscedastic linear LSFs (solid lines) and the homoscedastic linear LSFs (dashed lines) to the RACs as a function of the infra-red color $(R–I)_C$. We indicate the fits to the combined samples of high +low-activity stars (dK+dKe, dM+dMe) in each spectral sub-type (labelled "Low+High Activity"). The lower curves are the fits to low-activity stars only (dK, dM, labelled "Low Activity"). We also indicate the fits to the high-activity star sub-samples in the unsaturated regime (dKe, dMe, labelled "High Activity"). The slopes for the combined samples increase significantly from dK4 to dM4, with only minor differences between heteroscedastic and homoscedastic fits. For the low-activity stars, as a whole, the slopes for the heteroscedastic and homoscedastic models agree well and the results indicate that the slopes remain almost constant within the error bars from dK4 to dM4. The magnitudes of the slopes for the (unsaturated) high-activity stars lie significantly above those for the low-activity stars at spectral types dK4, dK6, and dM2. At the TTCC (M3) and beyond (M4), the slopes for the (unsaturated) high-activity stars significantly diminish.

to be conclusive of a saturation phenomenon, we assume here that, for $P/\sin i$ shorter than $\sim$2 days, saturation occurs. In this period range, we observe 12 fast rotators with a mean surface flux of $\sim 1.54 \times 10^5$ erg s^{-1} cm^{-2}.

We also performed separate linear LSFs to the sub-samples of only the low-activity dM4 and the sub-set of high-activity dM4e stars (all of which we assume are in the unsaturated regime), respectively (see Table 1). The heteroscedastic linear LSF to the dM4 low-activity stars yields:

$$F_{\mathrm{Ca\,II}} = 3.08 \pm 1.25 \times 10^4 \times (P/\sin i)^{-0.825 \pm 0.35}. \quad (26)$$

Therefore, the gradient of the RAC for the low-activity stars is again much shallower than that of the combined sample of low and high-activity stars (unsaturated), and by more than 3σ. Therefore, the linear LSF to the full sample is somehow inadequate. We note also that the slopes of the heteroscedastic linear LSF to the sub-samples of only the low-activity stars remain approximately constant (within measurement errors) from dK4 to dM4. This point will be further developed in Section 3.7.

The homoscedastic linear LSF to the dM4 low-activity stars yields:

$$F_{\mathrm{Ca\,II}} = 3.80 \pm 1.89 \times 10^4 \times (P/\sin i)^{-0.91 \pm 0.39}. \quad (27)$$

Again, the gradient of the RAC for the low-activity stars is shallower than that of the combined sample of low and high-activity stars, and by more than 3σ. We find that for the low-activity dM4 stars, both the homoscedastic and heteroscedastic models give similar results for the mean value of the slope of the RAC. And this mean value (0.825–0.91) is remarkably similar (within 1σ) to the mean values for low-activity stars in the other four spectral sub-types: 0.624, 0.637, 0.891, 0.93. However, there is one aspect in which the dM4 slow rotators differ from the other four sub-types: the dM4 stars have significantly larger values of σ associated with the slope of the RAC in both the homo- and heteroscedastic LSFs. We will return to this topic in Section 3.7.2.

We find that the χ^2 is much poorer for the heteroscedastic model (1.966) than that for the homoscedastic LSF (0.057). Nevertheless, both fits are statistically highly significant (better than 96%).

The heteroscedastic linear LSF to the 23 unsaturated dM4e high-activity stars yields:

$$F_{\mathrm{Ca\,II}} = 2.27 \pm 0.58 \times 10^5 \times (P/\sin i)^{-0.951 \pm 0.31}. \quad (28)$$

Therefore, the gradient of the RAC for the high-activity stars is also much shallower than that of the combined sample of low and high-activity stars, and by more than 3σ. Therefore, the linear LSF to the full sample seems rather inadequate. This point is straightforward if one looks at the linear heteroscedastic LSFs in Figure 12. It is obvious that the LSFs to the low-activity stars, and to the high-activity stars cannot be reproduced by a simple linear or quadratic function. We note that the dM4e data confirm the decrease in the slope of the LSF fits to unsaturated stars as we pass through the TTCC. In addition, we also performed a linear LSF to the full sample of dM4e stars (unsaturated+saturated) in order to compare with the previous fit. We find a slope of -0.47 for the full sub-sample of dM4e stars (Table 1). This result again suggests that the slopes for the sub-samples of low-activity stars and of high-activity stars are of the same order after the TTCC. The parameter $\frac{R}{\delta}$ is 18.90 for the high-activity star sub-sample and 19.13 for the low-activity star sub-sample. These figures are still very high, although that of the low-activity sub-sample has decreased compares to other spectral types. Therefore, the parameter $\delta = \frac{\langle \mathrm{error} \rangle}{\sqrt{n}}$ is still much smaller than the period domains of the RACs in both cases. As a consequence, these LSFs should be established with a good confidence level, which is in agreement with the high statistical significances we obtain for these fits (Table 1).

We find that the linear fits (to the unsaturated dM4+dM4e samples) are incapable of reproducing the slopes among the low-activity stars and the (unsaturated) high-activity stars. We face the same problem as we did in dealing with the case of dM3 stars: the problem is that there exist high activity, relatively slow rotators and low-activity, relatively fast rotators. These two types of stars overlap in their range of values of $P/\sin i$.

The dM3 and especially the dM4 data sets lead us to question the validity of fitting both the low-activity and high-activity (unsaturated) sub-samples with a single RAC. Instead, it seems to us that it might be better to consider the possibility that two distinct RACs are present in the data. To the extent that the RACs are determined with dynamo operation, this leads us to wonder: is there perhaps a distinct dynamo process operating in low-activity dM4 stars from the dynamo process that is at work in (unsaturated) high-activity dM4e stars? The slopes of the linear LSF to the low-activity stars for our five stellar samples are rather homogeneous, even for the dM4 stars,

although the latter stars are almost certainly fully convective. This result suggests that there may exist a single dynamo regime for the slow rotators from dK4 to dM4 within errors (see Section 3.7.2). This important result should be tested with larger samples of low-activity stars.

There exist more and more unsaturated high-activity-relatively slow rotators when we move to the spectral sub-types dM3 and especially dM4. These relatively slow rotators overlap in $P/\sin i$ with the low-activity stars. This poses an important problem: we cannot fit both the low-activity and (unsaturated) high-activity samples satisfactorily with a single RAC. We suggest that the dynamo mechanisms behave differently among the high-activity stars when crossing the TTCC. At the TTCC (dM3) and beyond, the data suggest that there exist two different dynamo regimes for low and high-activity stars (see Section 3.7). These differences in these dynamo regimes could be related to differential rotation: in the young high-activity stars differential rotation is expected to be larger and it should vanish with age, i.e., in the low-activity stars. Large differential rotation would boost the magnetic field generation in these fully convective stars, such that we could have high activity, relatively slow rotators with large differential rotation.

Now that we have assembled enough data to construct RACs at five different spectral sub-types for late K and M dwarfs, it is worthwhile to examine the systematics of RACs as a function of spectral sub-type.

3.7. The Slopes of the RACs: Variation with Spectral Sub-type

Now that we have values of the RAC slopes for five different spectral sub-types, we provide an overview by plotting the slopes as a function of the infra-red color index $(R–I)_C$ in Figure 13. In this figure, results are plotted separately for three distinct samples of stars: the low-activity stars only (lower curves), the (unsaturated) high-activity stars only (labelled "High Activity"), and the combined samples low+high-activity stars (labelled "Low+High Activity"). In this figure, the heteroscedastic models are plotted as solid lines, and the homoscedastic models are plotted as the dashed lines.

3.7.1. Linear LSFs: Combined Samples of Low Plus High Activity Stars

In Figure 13, the upper curves refer to the combined samples: the plotted points indicate the mean values of the RAC gradients that we have obtained for each of our five sub-samples by means of linear heteroscedastic (solid line) and homoscedastic (dashed line) LSFs. Attached to each mean value of the gradient is plotted the 1σ uncertainty in the mean value of the gradient.

We see that the value of the mean gradient becomes monotonically steeper as $(R–I)_C$ increases. The heteroscedastic (solid line) and homoscedastic (dashed line) models give similar results. There are some significant differences (above the 3σ level) between the two models for the dK6 sample, but this does not affect the overall trend observed for the gradient.

The fact that the magnitude of the gradient increases monotonically with increasing spectral type implies that the magnitude of the effects of rotation on the mechanisms of the dynamo increases systematically as we examine our combined samples at later spectral types. If this result is connected with the physics of the dynamo, and if it is physically permissible to consider low-activity stars in the same context as (unsaturated) high-activity stars, then the results in Figure 13 may provide an important new constraint on the dynamo mechanism(s). The magnitude of the gradient increases monotonically as we go from the spectral sub-type dK4 to the spectral sub-type dM4. The results in Figure 13 suggest that, if the TTCC occurs at dM3, the effects of rotation on chromospheric emission are larger in fully convective stars than in early M type and late K dwarfs where a radiative core persists. If this result is taken at face value, it does not appear to be consistent with the suggestions of Durney et al. (1993), mentioned in the first paragraph of Introduction.

Previous studies have also reported a variation in the RAC gradient of linear fits (e.g., Stepień 1989, 1993, 1994) as a function of spectral type: the RAC was found to be steepest (i.e., most negative) at dF6 ($B–V = 0.45$) and shallowest close to dK6 ($B–V = 1.41$; KH). However, the most complete study (Stepień 1989) did not include any stars that are cooler than dK6. Thus, the study we report here is complementary to Stepień's work, extending that work toward cooler stars as far as dM4 ($(B–V) = 1.60$). However, our results indicate that the trend noted by Stepień between dF6 and dK6 (namely, the RAC becomes shallower in cool stars) does not continue at later spectral types. On the contrary, we find that the trend in the gradient reverses: according to our samples, the RAC for the combined samples becomes steeper as we go toward dM4.

It is natural to wonder if the pronounced steepening of the RAC gradient is a signature of changes in the dynamo mechanism when crossing the TTCC. As noted in the Introduction, it appears that the TTCC lies between subtypes dM2 and dM4. In this context, we consider it significant that, among the stars in our samples, the RAC gradient for the combined samples steepens rapidly between spectral subtypes dM2 and dM4. Moreover, HM report a notable lengthening in the mean rotation periods of inactive and active stars also at spectral subtype M3. Also at M3, coronal loops in active stars become noticeably longer (see HM for a discussion of loop length data reported by Mullan et al. 2006).

Our data lead us to believe that something interesting takes place in the spectral subtype range dM2–dM4 as regards the rotational and activity parameters. Is the interesting behavior between dM2 and dM4 perhaps associated with changes in the dynamo regime when crossing the TTCC? Possibly, although we have not yet been successful in identifying a physical explanation that accounts for the results reported above. However, whatever the physical mechanism that is responsible for the increased steepnesses in Figure 13, the rise in the steepness of the gradient for the combined sample from sub-type K4 to sub-type M2 indicates that the changes occurring in the RAC slopes (and therefore perhaps also in the dynamo mechanism(s)) may be progressive and may begin even earlier than sub-type dM2.

3.7.2. Linear LSFs: Low Activity Stars Only

Now let us consider only the *low-activity stars*, in order to position ourselves as much as possible in the unsaturated regime of the Ca II fluxes, and therefore (hopefully) also in the unsaturated regime of the dynamo. The continuous line and dashed line in Figure 13 (lower curves) are a plot of the slopes of the heteroscedastic and homoscedastic linear LSFs respectively to the RACs for the low-activity stars sub-samples only. The parameter $\frac{R}{\delta}$ lies between 19.13 and 39.68 for these low-activity

star sub-samples. Therefore, the parameter $\delta = \frac{\langle \text{error} \rangle}{\sqrt{n}}$, which is a normalized estimate of the mean error on the measurements, is much smaller than the period domains of the RACs in all cases. Hence, these LSFs should be established to a relatively high confidence level, which agrees with the high statistical significances we obtain for these fits (Table 1).

In this regard, we note that the process of applying a LSF to a data set leads not only to a mean value for the slope: the LSF also yields a standard deviation σ for the slope. We consider it worthwhile to note that the values of σ contain information about the robustness of the slope.

Figure 13 shows that the slopes for the slow rotators (dK, dM only) do not behave the same as for the combined samples of stars (dK+dKe or dM+dMe). The gradient a for the low-activity stars remains almost constant (within the error bars) between dK4 and dM4 at a level of $a = -(0.8–0.9)$. More specifically, if we consider not merely the absolute value of a, but also the statistical significance of its value compared to its own σ, we find the following pattern: in dK4 stars, the magnitude of a is 5.6 times its own σ, in dK6 stars, a is 6.1 times its σ, in dM2 stars, a is 7.4 times its σ, and in dM3 stars, a is 4.3 times its σ. All four of these cases have slopes that are statistically highly significant. The chromospheric emission in these cases does indeed depend sensitively on rotation. But in M4 stars, a has a value that is only 2.3 times its own σ for the homoscedastic model and 2.4 times its own σ for the heteroscedastic model. In this case, at the 3σ level of significance, the mean slope that we have derived for the RAC of our sample of low-activity dM4 stars is formally consistent with zero. In a situation where the slope of the RAC is zero (or formally consistent with zero), the meaning is that the chromospheric emission in low-activity dM4 stars does not depend on rotation at all (or is consistent with zero sensitivity to rotation).

Although our LSFs of the slow rotators seem well established because of the large number of measures we have in our sub-samples, we still consider these results as preliminary and they should be confirmed with measures from a higher resolution spectrograph (such as ESO-ESPRESSO), because our errors on the individual measures are still large compared to the period domains of the RACs.

3.7.3. Linear LSFs: High Activity Stars Only

We also show the slopes of the heteroscedastic and homoscedastic LSFs to the sub-samples of only the (unsaturated) high-activity stars in Figure 13. The parameter $\frac{R}{\delta}$ lies between 17.20 to 23.45 for these high-activity star sub-samples (the case of dK4e stars is not considered because we have too few measures). Therefore, the parameter $\delta = \frac{\langle \text{error} \rangle}{\sqrt{n}}$, which is the normalized estimate of the mean error on the measurements, is much smaller than the period domains of the RACs in all cases. Hence, these LSFs should be established with a rather good confidence level, which agrees with the high statistical significances we obtain for these correlations ($\geqslant$90%, Table 1). However, we consider these results as still preliminary because the domains of the RACs are relatively small compared to the typical uncertainties on individual measures. We note that these slopes behave quite differently from the slopes of the low-activity stars and the slopes of the combined samples of low +high-activity stars. For the high-activity stars, we observe that the slopes are clearly steeper than those for the low-activity

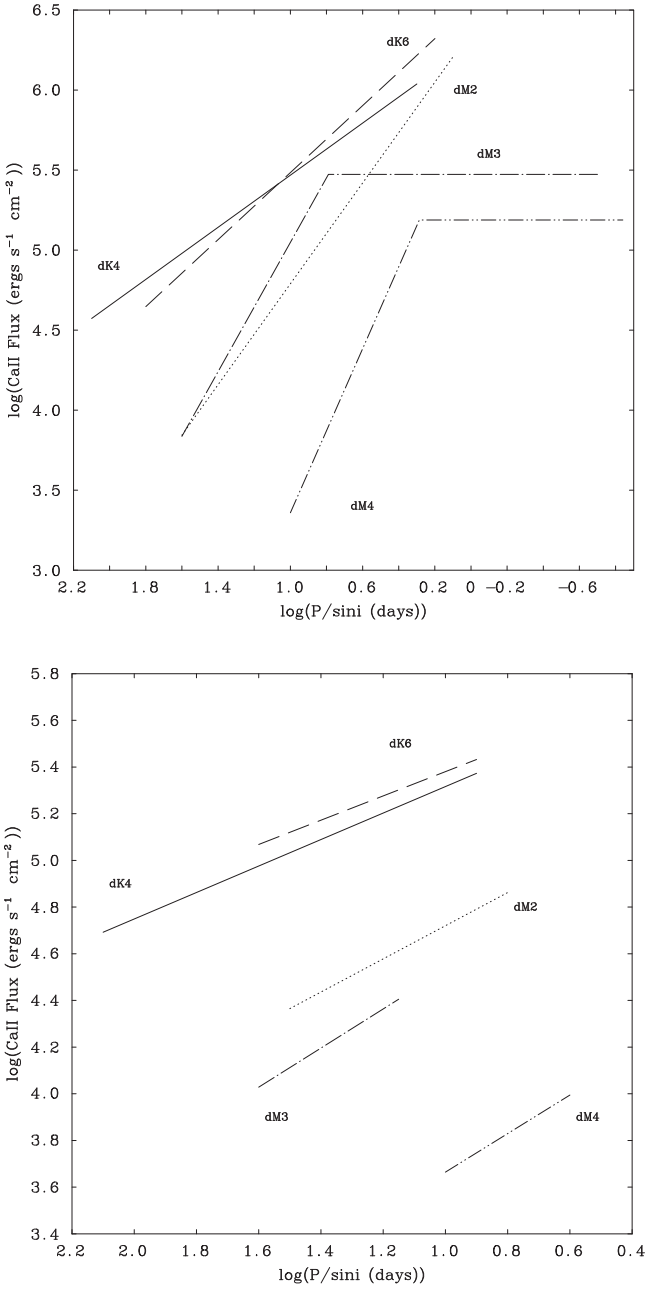

Figure 14. Upper panel: RACs for the logarithm of the Ca II resonance line surface fluxes and $\log(P/\sin i)$ for combined samples of low+high-activity stars in each sub-type dK4, dK6, dM2, dM3, and dM4. Note the major differences that exist between different spectral sub-types as regards the surface fluxes of the Ca II lines and the rotation periods. Lower panel: RACs for the same five spectral sub-types, but for the sub-samples of low-activity stars only (see the text).

stars at spectral types dK6 and dM2. At these spectral types, they are also steeper than the slopes of the combined samples of low+high-activity stars. These higher slopes suggest the existence of two different dynamo regimes for the low and the high-activity sub-samples for these stars.

However, things change at the TTCC. At the TTCC (dM3), the slopes for the high-activity stars are found to diminish dramatically, by a factor of about 2. Although there remains a large uncertainty on this slope for dM3e stars, the fall of the slopes at the TTCC is confirmed by the measure of the slope for dM4e stars with a much higher confidence level. Beyond the

TTCC (dM4), the slope continues to diminish. In fact, the slope at dM4 reaches a value that is very similar to the slope we have obtained for the low-activity star sub-samples (although we emphasize that the overall shapes of the RACs are very different: see Figures 8 and 12). This dramatic decrease in steepness among (unsaturated) high-activity stars at M3 and M4 suggests that the dynamo mechanisms operating in dK4, dK6, and dM2 high-activity stars (perhaps an α–Ω dynamo?) may be different from those operating in the fully convective dM3 and dM4 high-activity stars (perhaps an α^2 dynamo?). In this regard, we detect no major changes in the slopes at the TTCC for the low-activity star sub-samples apart from a decreased statistical significance of the RAC slope. This point is further discussed in the next sub-section.

We emphasize that, although our LSFs to the high-activity stars seem relatively well established, in our sub-samples we have only few measures (from 8 to 23). Therefore, these results should be confirmed with larger stellar samples and are still preliminary.

3.7.4. Approaching the TTCC?

These results lead us to suggest a five-part conclusion.

(i) The gradients of the RACs that we have obtained in our combined samples of low+high-activity stars unambiguously increase with increasing spectral type with a high level of confidence. But it also appears that the linear LSFs only provide a poor description of the full RACs.

(ii) There appears to be a significant dichotomy between the low-activity and the (unsaturated) high-activity sub-samples. This leads us to consider that there may exist two distinct dynamo regimes in dKe, dMe and dK, dM stars.

(iii) The gradients of the combined samples suggest that there are changes operating in the dynamo mechanisms before, at, and after the TTCC. In addition, the gradients to the high-activity sub-samples point to important changes in the dynamo mechanisms occurring at the TTCC and beyond.

(iv) We can confidently assert that in low-activity dK4, dK6, dM2, and dM3 stars, there is a robust ($>4\sigma$) increase in Ca II flux as the period decreases. That is, the dynamo in unsaturated dK4–dM3 stars *is* clearly sensitive to rotation.

(v) But in low-activity M4 stars, the sensitivity of the dynamo to rotation, although still perhaps present, is not as robust, and may even be zero (at the 3σ level of significance). Thus, even in the low-activity stars in our samples, a rotational dynamo is certainly contributing significantly to chromospheric heating in dK4–dM3 stars. But in dM4 low-activity stars, the signs of rotational control over chromospheric emission are less significant (in a statistical sense).

These two last points, if they can be confirmed, might be relevant in the context of Durney et al. (1993), who suggested that rotation would be a controlling influence in the case of interface dynamos, but should not be as effective as a controlling influence in distributed dynamos. On the one hand, the robust sensitivity to rotation that we have found in dK4–dM3 low-activity stars could be evidence for interface dynamos in those stars. On the other hand, in dM4 low-activity stars, the weaker evidence for statistically significant rotational sensitivity might presage the lessening of the effects of an interface dynamo. In this context, M3 might be considered to be the latest spectral sub-type to have definitive evidence for the presence of a radiative core (so that an interface dynamo is even possible). It is worth recalling that HM also concluded that at M3, something unusual happens to the rotational braking. Could the HM result, in combination with our results for the RAC slope, be a sign that the TTCC occurs between M3 and M4? This will be tested in a future study using an even finer grained spectral type sampling at about the TTCC using new data.

We suggest that in Figure 13, the striking difference between the combined sample (upwardly rising lines) and the low-activity stars only (lower lines) may be associated with the fact that the combined sample might contain two distinct regimes of dynamo operation (high and low), whereas the low-activity sample contains only a single regime (low). Suppose that the separation of dM4e stars from dM4 stars in Figure 12 is associated with two distinct dynamo regimes: if so, the attempt to fit a LSF to the combined sample of dM4+dM4e stars may involve an attempt to "force" two different types of dynamos into a single mold. Such an attempt would not be as physically meaningful as attempting to fit a truly homogeneous population (e.g., the low-activity stars alone). Analogous arguments can be made for dM3 stars (Figure 8) and dM2 stars (Figure 5). According to this argument, it may be more profitable to focus separately on the different curves of the low-activity stars and the high-activity stars respectively in Figure 13 in order to gain insight into dynamo theory.

We conclude that for the low-activity stars only, the gradient is definitely shallower than that for the samples of the low plus high-activity stars. But we also conclude that the gradient for the low-activity stars only does not vary significantly with spectral type. We also note that the differences between the slopes for the low-activity stars and for the low+high-activity stars increase drastically with increasing spectral type. This result emphasizes that the efficiency of the dynamo mechanisms increases drastically at short rotation periods, and also increases with decreasing stellar mass. We also conclude that there are no significant changes occurring in the efficiency of the dynamo mechanisms for low-activity stars as a function of stellar mass when moving from dK4 to dM4.

3.7.5. Different Dynamo Regimes Among Low Activity and High Activity Stars at the TTCC and Beyond?

In the plots that we have compiled of each RAC for our five spectral sub-types (Figures 2, 3, 5, 8, 12), we overplot the separate heteroscedastic linear LSF to the low-activity stars and to the high-activity stars for direct comparison with the heteroscedastic linear LSF to the low+high-activity samples. As we saw in the previous sections, the overplots show clearly that the linear LSF to the low+high-activity stars fails completely to reproduce the slopes of the linear LSF that we have derived both from the slow rotators and the fast (unsaturated) rotators. We show that the low+high-activity samples cannot be described by a single RAC.

In view of this, it seems to us that, to the extent that the RAC is determined by a dynamo mechanism, we need to invoke two different dynamo regimes. The first (we suggest) is at work among dK and dM stars (i.e., low-activity stars). This first regime seems rather constant from dK4 to dM4 and is therefore independent (to a first approximation) of the spectral type.

A second dynamo regime (we suggest) is at work among dKe and dMe stars. This second regime exhibits steeper RAC slopes for the spectral types dK4, dK6, and dM2, and shallower slopes for the dM3 and dM4 spectral types. The data suggest that the second regime deviates significantly from the first regime at the TTCC and beyond. The main problem is that, among the stars in our samples at spectral sub-types dM3 and dM4, there are interlopers, namely, a certain number of high-activity, relatively slow rotators and a certain number of low-activity relatively fast rotators that overlap in $P/\sin i$. These interlopers make it impossible to reproduce the entire data sets with a single RAC. Our results suggest that, whether we are considering low-activity stars alone, or the combined samples of low+high activity, the properties of the RACs undergo changes of some kind, especially at the TTCC and beyond. This conclusion is especially true for dM4 stars.

The findings we present here can be considered as providing evidence in favor of the following hypothesis: the dynamo mechanism in fully convective stars is different from the dynamo mechanisms in stars where a tachocline exists. We propose that differential rotation (probably important in the young dMe stars and less important in the older dM stars) plays an important role in defining the RACs among dM and dMe stars at the TTCC and beyond.

3.8. The RACs for Five Different Spectral Sub-types

We bring together the heteroscedastic linear fits to the low +high-activity RACs (in terms of surface fluxes) for our five spectral sub-types in Figure 14 (upper panel). In this section, we discuss two key aspects of the figure, and how they vary as a function of spectral type: (i) the absolute magnitudes of the Ca II flux and (ii) the slopes of the RAC in the unsaturated regime.

There are several striking trends in this figure. First, with increasing spectral type, the curves tend to shift downward and to the right, i.e., the overall level of chromospheric flux decreases, and the periods tend to be shorter. Important differences between the RACs of dK4, dM2, and dM4 stars have already been reported by Houdebine (2012b). Also, variations in the RAC properties at different spectral types was previously reported by Stepień (1993, 1994). He found that the $\log(R'_{\rm HK})$–$P_{\rm rot}$ relationships globally shifted toward shorter rotation periods as $(B–V)$ increases from 0.52 (dF7.5) to 1.15 (i.e., spectral type dK5, according to KH). On the other hand, in an earlier study, the opposite tendency emerged: Stepień (1989) found that the $\log(\Delta F_{\rm Ca\,II})$–$P_{\rm rot}$ relationships were globally shifted toward longer rotation periods for $(B–V)$ from 0.45 (dF6) to 0.66 (dG5) and that they stabilize for $(B–V)$ from 0.75 (dG8.5) to 1.40 (dK6). Also, Patten & Simon (1996) proposed that the projected rotation period becomes longer as one move from spectral types G1 to M2. In view of this complicated behavior, it seems that in the $F_{\rm Ca\,II}$–$P_{\rm rot}$ RACs, first the rotation period becomes longer between dF6 and dG7, then remains unchanged between dG7 and dK6, and then the period starts to become shorter between dK6 and dM4; the latter behavior persists into later spectral types.

In Figure 14, in the context of the combined samples (upper panel), one can see that the steepness of the RACs (at least in the unsaturated regime) increases noticeably as we go toward later spectral type (as already shown in Figure 13). We have not detected any saturation behavior for stars in our dK4, dK6, or dM2 stars, whereas we may observe a saturation in dM3 and dM4 stars for the most rapid rotators. Might this saturated-unsaturated behavior also point toward a different dynamo mechanism in dM3 and dM4 stars from the dynamo mechanism in dK4, dK6, and dM2 stars? We also observe that the largest Ca II surface fluxes are found in the stars with the earliest spectral types (dK4, dK6, dM2). For dM4 stars, there is a pronounced decrease in the absolute magnitudes of the surface fluxes for the fastest (unsaturated) rotators compared to dM2 stars. But even among relatively slow rotators (with periods longer than 10 days), where any effects of saturation are expected to be minimal, the Ca II surface fluxes are observed to decline by more than 100 between dK4 and dM4.

Surveying the results, we see that dK4 and dK6 stars have similar RACs, with a slightly larger gradient for the dK6 stars. Then the RAC falls to lower surface fluxes for dM2 stars and the RAC steepens. The RAC for dM3 stars is distinctly different in shape compared to that of the dM2 stars: dM3e stars exhibit saturation whereas the dM2e stars do not. Also, dM3 stars overlap in rotation periods with dM2 stars. This is due to the fact that we found (in HM) that dM3 stars possess abnormally long rotation periods for both high-activity and low-activity stars compared to the adjoining dM2 and dM4 stars. In HM, it was suggested that the anomaly of relatively long rotational periods at type M3 might be related to an empirical report (Mullan et al. 2006) that flaring loop lengths undergo an increase to larger values at dM3. In dM4 stars, the (unsaturated) RAC shape parallels that of dM3.

The trends in surface fluxes of Ca II in Figure 14 suggest that, whatever is controlling chromospheric emission in our sample stars, the mechanism is less effective (by factors of 10 or more), and leads to different RAC shapes, in dM3 and dM4 stars than in dM2, dK6, and dK4 stars.

As regards the latter stars, it might at first sight seem that we should be confident that interface dynamos are at work (e.g., Mullan et al. 2015). (Unfortunately, we cannot be absolutely confident that *only* an ID is at work in the dM2, dK6, and dK4 stars: the results of Brown et al. (2010) indicate that a DD can also operate in the convection zone of partially convective stars. If both ID and DD are in fact simultaneously operative in a certain star, current dynamo models give no quantitative results for the relative strengths of magnetic fields that would be generated by the different dynamos. Thus, although we use the words "fairly confident" in the present context, the question of the relative importance of ID and DD in a partially convective star remains ambiguous.

Could it be that the different RAC shapes in dM3 and dM4 stars might be due to the absence of an interface dynamo? If so, TTCC may be occurring between dM2 and dM3 sub-types. We also note that the changes in the RACs are progressive from dK4 to dM4, and that the fall in the fluxes begins at about dM2 and continues from dM3 to dM4. However, whatever the correct physical interpretation in terms of different dynamos eventually turns out to be, our data show that the efficiency of the dynamo mechanisms falls progressively from dK6 to dM4, and that this fall is particularly pronounced after the TTCC at spectral sub-type M4.

3.8.1. Low Activity Stars Only

In the lower panel of Figure 14, we show results of the heteroscedastic models for low-activity stars only. The most striking difference between the lower and upper panels in

Table 8
Values of $\log(L_{HK})$, $\log(L_{bol})$, R'_{HK}, and R_0 for Our Samples of dK4, dK6, dM2, dM3, and dM4 Stars

Star Name	$\log(L_{HK})$ (erg s^{-1})	$\log(L_{HK})$[a] (erg s^{-1})	$\log(L_{bol})$ (erg s^{-1})	R'_{HK}	R'_{HK}[a]	$\log(L_X)$ (erg s^{-1})	$\log(L_X/L_{bol})$	R_0
			K4					
GJ 4061	28.062	⋯	32.840	−4.778	⋯	⋯	⋯	0.1801
GJ 4322B	27.739	⋯	32.993	−5.254	⋯	28.164	−4.829	0.7267
Gl 106	28.338	⋯	32.999	−4.661	⋯	28.384	−4.615	0.4069
Gl 131	28.322	⋯	32.661	−4.338	⋯	⋯	⋯	0.6554
Gl 160.2	27.948	⋯	32.638	−4.690	⋯	27.342	−5.296	0.5172
Gl 413	27.659	⋯	32.705	−5.046	⋯	⋯	⋯	1.0236
Gl 416	28.354	⋯	32.891	−4.537	⋯	⋯	⋯	0.7809
Gl 517	28.876	⋯	32.589	−3.713	⋯	29.554	−3.035	0.0252
Gl 570A	27.940	⋯	32.971	−5.031	⋯	27.544	−5.427	0.7265
Gl 664	28.201	⋯	32.777	−4.576	⋯	27.748	−5.029	0.2794
Gl 698A	28.398	⋯	32.819	−4.421	⋯	28.041	−4.778	⋯
Gl 707	28.354	⋯	32.665	−4.312	⋯	⋯	⋯	0.3142
Gl 719AB	29.338	⋯	32.792	−3.454	⋯	29.808	−2.984	0.0833
Gl 727	28.441	⋯	33.031	−4.590	⋯	28.320	−4.711	0.4797
Gl 775	28.362	⋯	32.996	−4.634	⋯	27.813	−5.183	0.6563
Gl 818	28.280	⋯	32.829	−4.549	⋯	⋯	⋯	0.6411
Gl 820A	28.135	⋯	32.780	−4.645	⋯	27.447	−5.333	0.6712
Gl 879	28.391	⋯	32.910	−4.519	⋯	28.326	−4.584	0.2816
Gl 898	28.502	⋯	32.642	−4.140	⋯	28.107	−4.535	0.1517
MCC 266	28.310	⋯	32.963	−4.653	⋯	⋯	⋯	0.6229
MCC 522	28.966	⋯	32.960	−3.994	⋯	⋯	⋯	0.1131

Note.
[a] Corrected from metallicity effects.

(This table is available in its entirety in machine-readable form.)

Figure 14 is that the low-activity stars do not exhibit any evidence for saturated behavior. Moreover, a striking characteristic of the lower panel is that the five RACs are almost all parallel to one another (as already noted in Figure 13). These features support our claim that low-activity stars may provide us with a possible "window" into a more homogeneous sample in terms of the dynamo mechanism: it seems likely that only unsaturated dynamo operation is at work in the lower panel of Figure 14.

We note that surface fluxes for unsaturated dM4 stars are again found to be 10–100 times smaller than those in unsaturated dK4 and dK6 stars. And we also observe a similar global pattern in both panels (upper and lower): there is a trend toward shorter periods with increasing spectral type.

It is clear that the overall level of Ca II flux is diminishing as we go from K4 to M4: the b coefficient of the linear LSF to the RAC of dK4 stars is larger than the linear LSF to the RAC of dM4 stars by a factor of 25. This suggests that the dM4 stars at any given period are generating mechanical energy flux some 25 times less effectively than dK4 stars with the same rotational period. Even in the much narrower gap between dM3 and dM4, the b value for the linear LSF to the RAC has decreased by a factor of almost 10 at any particular rotational period. These results indicate that dM4 stars really are suffering from a weakening of the ability to generate mechanical energy (whether in magnetic form or in acoustic form or in a combination of both forms) compared to dM3 and earlier subtypes.

We conclude that the overall level of dynamo efficiency (as regards chromospheric heating) diminishes markedly as the stellar mass decreases. However, we also find that, as regards the low-activity stars (i.e., unsaturated dynamos), there is an almost universal dependency of the dynamo efficiency on the rotation period: i.e., the level of activity varies approximately as $\sim P/\sin i^{-0.80}$. This universal feature is missing when we attempt to analyze samples that combine stars of both low-activity and high activity. For the combined samples, our results indicate that the dynamo efficiency decreases differentially and drastically with decreasing rotation period as we move from dK4 dwarfs to M4 dwarfs.

3.9. R'_{HK} as a Function of the Rossby Number

In the spirit of searching for RACs among a variety of parameters (in case the correlations are obscured more in certain cases), we now set aside the rotation period that we have used so far, and explore how activity depends on Rossby number. Dynamo theory suggests that the dynamo efficiency, and therefore the magnetic field strength and its direct diagnostic in the chromosphere, the Ca II lines, should scale with the dynamo number (Montesinos et al. 2001) N_D given by:

$$N_D \sim \frac{1}{R_0^2}\frac{\Delta\Omega r_{cz} L}{\nu\Omega d^2} \tag{29}$$

where $R_0 = P/\tau_c$ is the Rossby number, τ_c the convective overturning time, Ω is a characteristic rotation rate in the lower convection zone, r_{cz} the radius at the base of the convection zone, L the characteristic length-scale for the differential rotation in the overshoot region just below the convection zone, ν the ratio of the diffusivities in the two layers directly below and above the overshoot region and the quantity d is given by $d \sim \sqrt{\eta\tau_c}$ where η is the turbulent diffusivity in the layer just above the overshoot region. Making reasonable assumptions for late-type stars, the dynamo number simplifies to

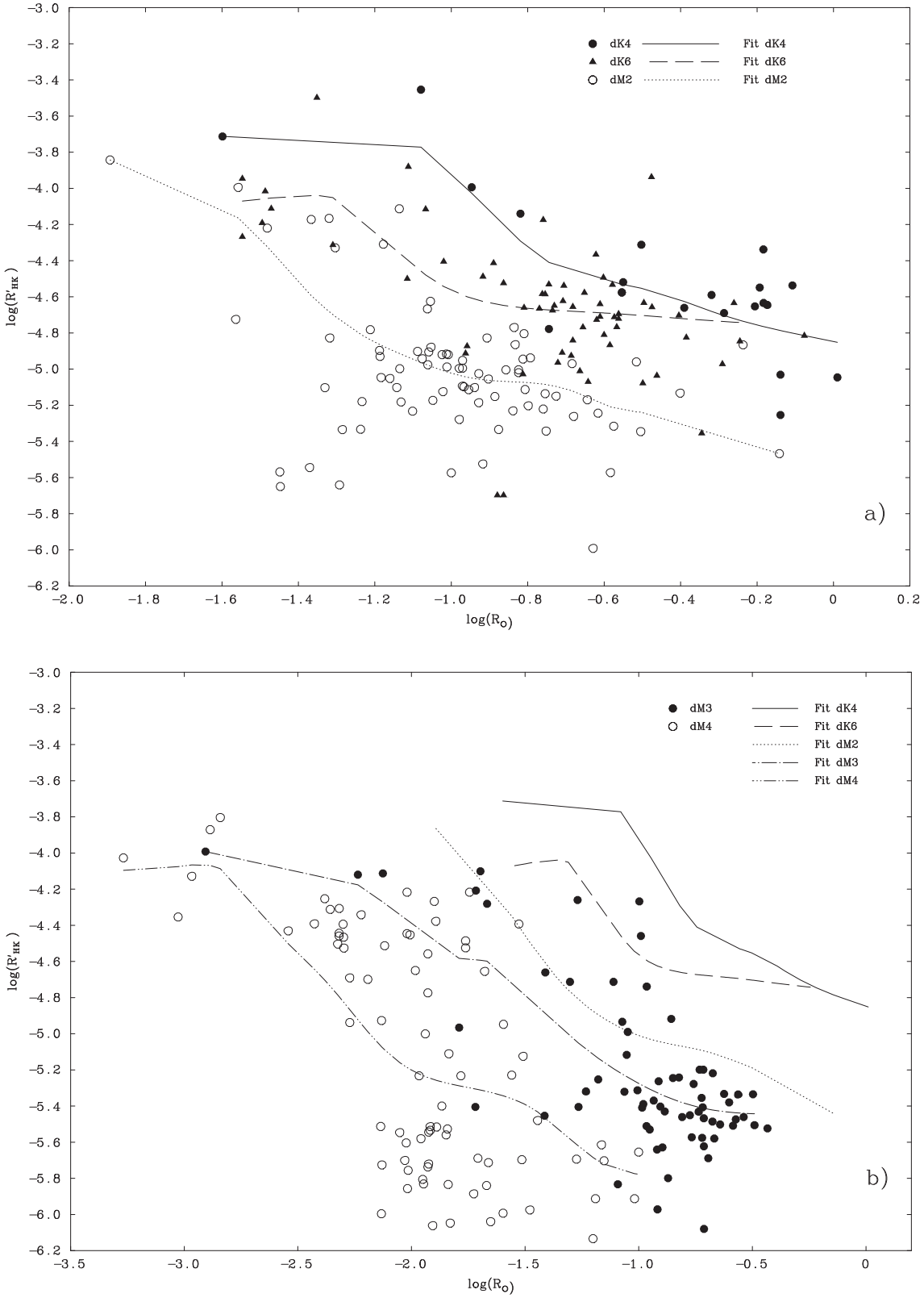

Figure 15. Upper panel: $R'_{\rm HK}$ as a function of the Rossby number, R_0. Solid line: the mean empirical relationship for dK4 stars. The data for dK4 stars is a good representation of the F, G, early K type star correlation. For dK6 stars, the mean values of $R'_{\rm HK}$ (long-dashed line) lie on average a factor of 3 below the dK4 stars. For dM2 stars, the mean values of $R'_{\rm HK}$ (dotted curve) lie a factor of about 10 below the dK4 stars. Lower panel: dM3 stars (dotted-dashed curve) and dM4 stars (double-dotted-dashed curve) lie a factor of about 20 and 90 below the dK4 stars, respectively. Our data indicate a gradual decrease in the fluxes in M dwarfs that continues into the fully convective M3 and M4 dwarfs, in agreement with our findings on the RACs based on the Ca II stellar surface fluxes (Section 3.6). This suggests a progressive change in the dynamo mechanisms from a shell dynamo to a distributive dynamo.

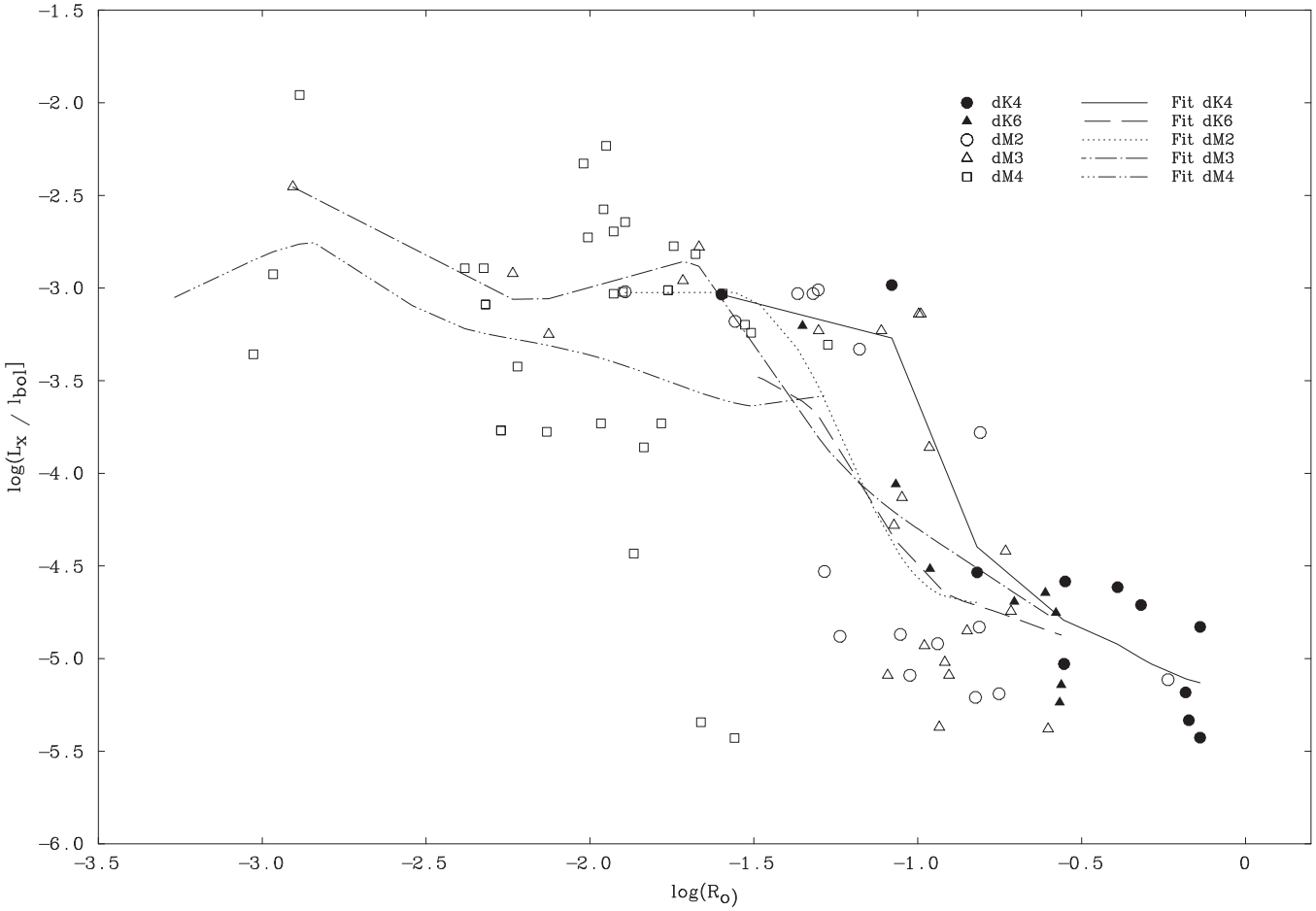

Figure 16. L_X/L_{bol} as a function of the Rossby number, R_0, for our five different spectral types. We overplot the running means for dK4, dK6, dM2, dM3, and dM4 stars. Note the important differences in the behavior of L_X/L_{bol} (this figure) compared to that of R'_{HK} (see Figure 15).

(Noyes et al. 1984, hereafter N84):

$$N_D \sim (\Omega\tau_c)^2 \sim R_0^{-2}. \quad (30)$$

Therefore, a good evaluation of the efficiency of dynamo mechanisms can be done through plotting the chromospheric indices $R'_{HK} = L_{HK}/L_{bol}$ (where L_{HK} is the luminosity in the H and K lines of Ca II) as a function of the Rossby number $R_0 = P/\tau_c$ (e.g., N84, Stepień 1989, 1994; Hempelmann et al. 1995; Patten & Simon 1996; Montesinos et al. 2001).

Montesinos et al. (2001) argue that the dimensionless factor,

$$\frac{\Delta\Omega r_{cz} L}{\nu\Omega d^2} \quad (31)$$

plays a role in the scatter of the R'_{HK} versus R_0 diagrams. This dimensionless factor depends notably on the internal differential rotation, which is mostly confined to the overshoot region just below the convection zone as well as on the turbulent magnetic diffusivities, neither of which are currently reliably known. In view of this lack of information, we shall for simplicity here assume this dimensionless factor to be constant for our samples of late-type dwarfs.

In order to evaluate Rossby numbers in the stars of our subsamples, we have adopted values of τ_c from the results of Spada et al. (2013) who gives the relationship between stellar mass $M_\star$ and τ_c. We derived a relationship between the stellar radius, $R_\star$, and τ_c using the mass–radius relationships of Spada et al. (2013) for [Fe/H] = 0. The results of Spada et al. (2013) on τ_c are in reasonably good agreement with other calculations (e.g., Kim & Demarque 1996). Recent values of τ_c agree to some extent with the values of Noyes et al. (1984) for solar masses down to $M_\star \sim 0.8\,M_\odot$ but differ substantially for lower mass stars. We compare the values of τ_c from Spada et al. (2013) and Noyes et al. (1984) for our five spectral sub-types in Paper I. The large increase in the numerical values of τ_c, which we take from Spada et al. (2013), at low masses has important consequences for the R'_{HK}/R_0 relationships in M dwarfs as we shall see below.

We use the $\tau_c/R_\star$ tabulation to derive R_0 for each star in our five samples of stars. We also computed the luminosity, L_{HK}, in the Ca II lines according to the continuum surface fluxes derived above from the models of de Laverny et al. (2012). We list the Ca II luminosities L_{HK} and R_0 for our five samples of stars in Table 8. We also computed the bolometric luminosities L_{bol} and the activity index $R'_{HK} = L_{HK}/L_{bol}$ for all our targets. We list the results in Table 8. We further computed L_{HK} and R'_{HK} corrected for metallicity effects for dM2, dM3, and dM4 stars.

Mullan & MacDonald (2001) suggest that the ratio of the X-ray luminosity created by large-scale fields $L_X(L)$ to that of the X-ray luminosity created by turbulent fields $L_X(t)$ may attain factors of 5–10. Although the case of chromospheric lines does not necessarily track the coronal X-ray emission, one might also expect a decrease in chromospheric emission when

the dynamo mechanisms change from a shell dynamo to a distributive dynamo. Note, however that in the case of the chromosphere some modeling calculations (e.g., Ulmschneider & Musielak 2003; Fawzy et al. 2002; Ulmschneider et al. 2005a, 2005b) lead one to expect a basal flux in the chromospheric lines. Such basal flux has not been observed in our data sets (e.g., this study, Papers XV and XVIII). However, some previous authors claim to have detected such fluxes for various spectral types (e.g., Wilson 1968; Schrijver 1987; Rutten et al. 1991; Strassmeier et al. 1994; Fawzy et al. 2002). Note however that M dwarfs were usually excluded from those studies. On the other hand, there do exist certain data sets for line fluxes of Mg II and Ly_{α} in inactive M dwarfs that have been found to be consistent with ab initio models of acoustically heated chromospheres (Mullan & Cheng 1993): thus, there seems to be little reason to exclude the concept of "basal" fluxes from a discussion of dM chromospheres. Here we investigate the $R'_{\rm HK} - R_0$ relationships from dK4 stars to the fully convective dM3 and dM4 stars and search for a signature of the change in the dynamo mechanisms at the TTCC.

In Figure 15, we plot $\log(R'_{\rm HK})$ as a function of $\log(R_0)$ for our five different spectral types. We found, using the values of τ_c from N84, that the mean of the measurements for dK4 stars (the dK4 data smoothed with a Gaussian of FWHM = 0.1) agree well with the correlation for F, G, and K type stars found by N84. Thus, our RAC data for dK4 stars are consistent with the N84 study and represents well a low-mass extension of the correlation for F, G, and early K type stars.

In Figure 15 (upper panel), we can see that for the dK6 stars (filled triangles), the mean values (the data smoothed with a Gaussian of FWHM = 0.1, dashed line) lies slightly below the correlation for dK4 stars, typically by a factor from 1.5 to 5.0, i.e., a factor of 3 on average. The dK6 curve crosses the dK4 curve at $\log(R_0) \sim -0.2$. There is a large scatter in the data for dK4, dK6, and dM2 stars in spite of the fact that we corrected the data for the effects of metallicity in dM2 stars (otherwise, the scatter is even larger): this is explained by the variations in radii of our stars at a given spectral sub-type, and the large variations of τ_c with radius. This scatter increases for the spectral types dM3 and dM4 Figure 15(b)) because, for these stars, there is a large increase in τ_c with decreasing stellar radius and within a small range in radius (see Spada et al. 2013).

For our dM2 stars, the situation is more striking: the data (dotted line in Figure 15(a)) now lie much lower than the dK4 curve. There is a clear and large difference between our dK4 data and our dM2 data. Over the common range in R_0, the curve for dM2 stars is roughly parallel to that of the dK4 stars, but is shifted below by a factor from 6 to 16. Our data for the dM2 stars cover a larger range in R_0 than in previous studies, notably for small values of R_0 (i.e., stars with short rotational periods). One can see that the correlation suddenly rises for $\log R_0$ less than −1.3. At small values of R_0, $\log(R'_{\rm HK})$ reaches values of about −4.0 or even larger.

Moving later in spectral sub-type, we show in Figure 15 (lower panel) the analogous data for our dM3 and dM4 stars. We note that, in this diagram, the mean data for these stars (dash-dotted line) generally lie below the correlation of dK4 stars (solid line), and also significantly below our dM2 data (dotted line). The large variations in τ_c between M2, M3, and M4 stars imply that the curves for M3 and M4 stars are systematically shifted toward lower R_0. But we emphasize that also, globally, the values of $R'_{\rm HK}$ decrease from M2 to M4 (Figure 15, lower panel). The mean curve for our dM3 stars lies significantly below the mean curve for dM2 stars. This difference is even more pronounced for the sample of dM4 stars. At $\log(R_0) = -1.2$, we find that the dM3 curve lies a factor of 20 below that of the dK4 stars, and that the dM4 curve lies a factor of about 100 below the dK4 curve (Figure 15, lower panel). The curves for dM2, dM3, and dM4 stars are more or less parallel (except at very low values of R_0 for dM3 and dM4 stars, where there are only a few data points). This highlights the consistency of the decreases in the $R'_{\rm HK}$–R_0 curves when going from mid-K type stars to the fully convective dM4 stars.

The decrease from dM2 to dM3 stars is typically a factor of 2 (at $\log(R_0) = -1.0$, whereas the decrease from dM3 to dM4 stars is typically a factor of 4 (taken at $\log(R_0) = -1.5$).

Christian et al. (2011) have reported a saturation (or even "super-saturation") phenomenon in the chromospheric emission for fast rotators in young clusters at about $\log(R'_{\rm HK}) = -4.08$ but with a significant scatter (±0.5 in the log-transformed data). In our stellar samples, we do not have enough very fast rotators to confirm the existence of super-saturation. However, we note that $R'_{\rm HK}$ measures generally lie below −3.8 for all our samples of late-K and M dwarfs. We also find that this high level of activity is attained for different values of R_0 that depend on the spectral type. For dK4 stars, this high level of activity is attained at about $\log(R_0) \sim -1.0$, whereas for dM4 stars, it is attained at about $\log(R_0) \sim -2.7$.

Our data sets suggest that M dwarfs (especially M3 and M4) generally do not follow the same relationship as F, G, and K dwarfs. This had not been noted previously because the M dwarf data sample was too sparse. If this difference is due to a difference in dynamo mechanisms, then the change in dynamo mechanisms seems to be progressive, as is illustrated by our dK6 and dM2 data sets. Therefore, we cannot conclude from the results in Figure 15 that there is any abrupt change at the TTCC (if this occurs no later than M4): instead, there seems to be a gradual decrease in the efficiency of the dynamo mechanisms that may start as early as spectral type dK6. This gradual change was suggested by Mullan & MacDonald (2001). The efficiency of an interface (shell) dynamo may fall off between dK4 and dM2 as the radiative core occupies an increasingly small proportion of the stellar radius (Mullan et al. 2015), and the present data suggest that this decrease continues at least as far as M4. The latter point is strengthened by our results in Paper XV, which showed a *progressive* change from high fluxes (large radii M2 dwarfs, partially convective) to very low fluxes (M2 subdwarfs, fully convective). The $R'_{\rm HK}$–R_0 diagram may be one of the most sensitive tests for detecting changes occurring in the dynamo mechanisms. However, the results from these RAC relationships have to be compared with the other magnetic activity indicators we study here. Note that with the present data there is evidence in the $R'_{\rm HK}$–R_0 diagrams that gradual changes in the dynamo efficiency are occurring all the way to M4. Other magnetic activity diagnostics, including the mean fluxes (Section 3.8), also point to a continued change from K4 to M4.

The results in Figure 15 strongly suggest that, as far as chromospheric heating is concerned, there may be a gradual decrease in dynamo efficiency in M dwarfs compared to F, G,

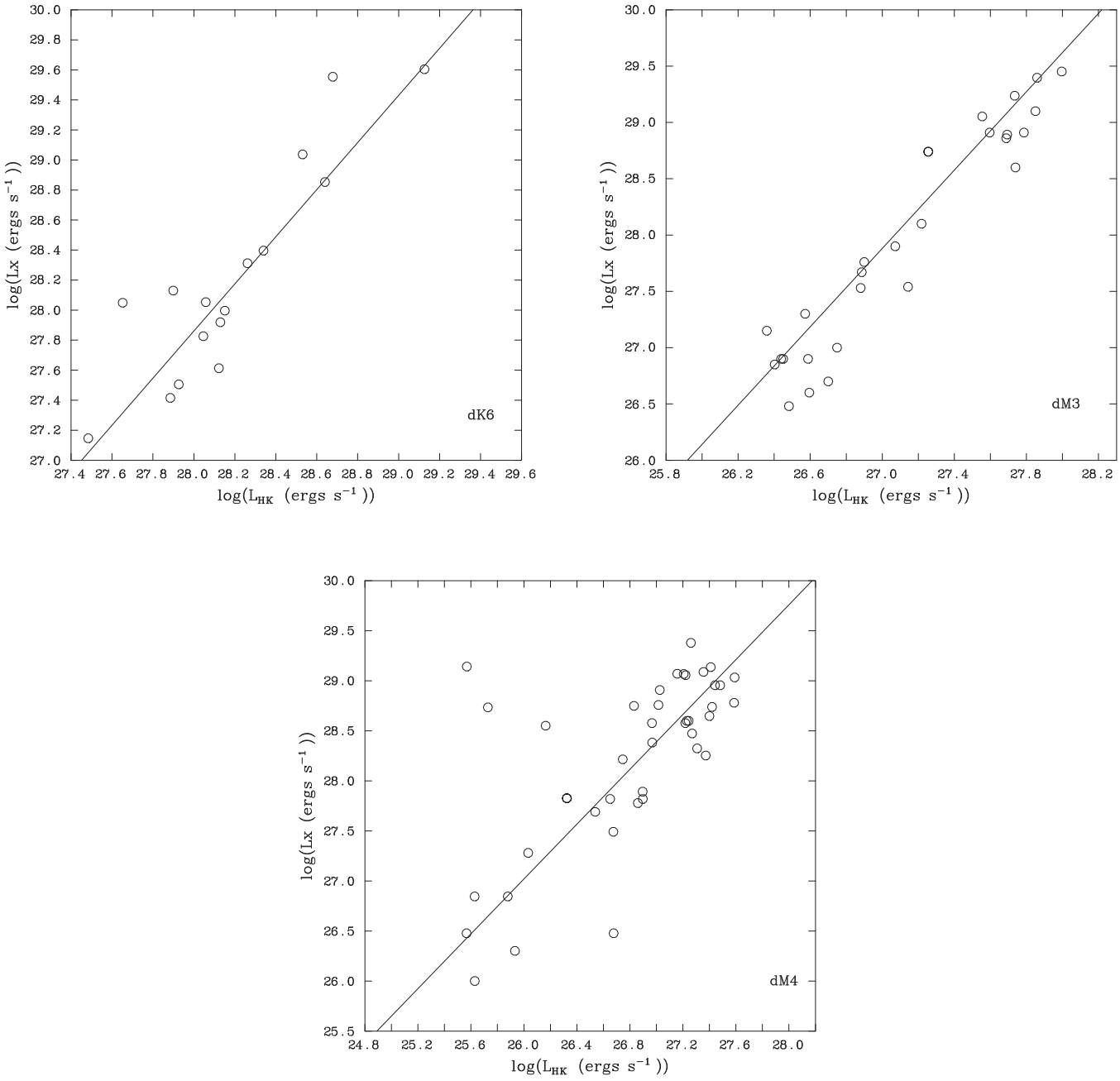

Figure 17. L_X vs. L_{HK} for the stars in our dK6, dM3, and dM4 samples for which *ROSAT* X-ray data are available. As regards the empirical correlations (solid lines), the slopes are very similar: 1.54, 1.74, and 1.37 for dK6, dM3, and dM4 stars, respectively. Note the differences in the *scales* on both axes for the different panels: for a given value of chromospheric emission, the dM4 stars have a much larger coronal emission than the dK6 stars.

and K dwarfs. It is generally believed that an α–Ω type of dynamo dominates in F, G, and K dwarfs. In early M dwarfs, an interface dynamo is probably still operating (Mullan et al. 2015), although eventually, in fully convective M dwarfs (beyond the TTCC), the dynamo mechanism is expected to behave differently. The most striking conclusion of the present section is that, as regards chromospheric heating, there are almost two orders of magnitude decrease in going from dK4 to dM4. This further strengthens our previous findings (see Figure 14) that, in the context of chromospheric heating, the mechanical fluxes decrease by a factor of order 100 as we go from dK4 to dM4.

3.10. The Coronal RAC: L_X/L_{bol} as a Function of the Rossby Number

Now we turn to the corona, where deposition of mechanical heating manifests itself in the form of X-ray luminosity L_X. Mullan & MacDonald (2001) found that, in a sample of some 40 *ROSAT* measures of dMe stars by Fleming et al. (1993), L_X/L_{bol} was found to remain essentially invariant over the spectral range from early M to at least M7, at least for the most active stars (see also Browning et al. 2010). This result, which implies that coronal heating efficiency in the most active stars remains unchanged at the TTCC, now appears worth re-examining in the context of our findings (see Figure 15) of changes in

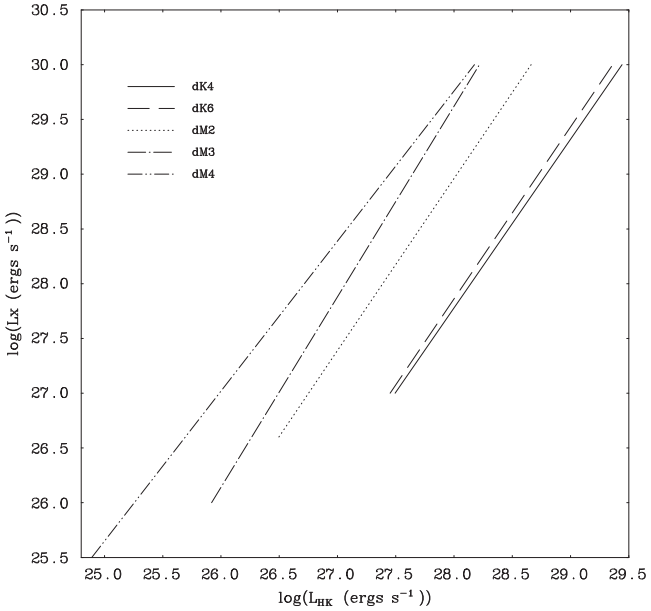

Figure 18. L_X as a function of L_{HK} for all five of our spectral sub-types. The gradients of the empirical correlations are similar for the five spectral types. But the more pronounced aspect of this figure is that, at a given chromospheric flux, the coronal flux increases toward later spectral types. For instance, for a chromospheric Ca II luminosity of $10^{27.5}$ erg s^{-1}, the X-ray luminosity increases by a factor of 110 from spectral type dK4 to dM4.

chromospheric heating before and near the TTCC. Our sample is now several times larger than that of Fleming et al. (1993). We therefore investigate here the behavior of L_X/L_{bol} as a function of R_0 for our five different spectral sub-types, to see if we can identify any signature of the TTCC in the coronal data.

In order to illustrate the sensitivity of coronal heating to rotation, in Figure 16 we plot L_X/L_{bol} as a function of R_0 for our five different spectral sub-types. We also plot in this diagram the running mean curves for our dK4, dK6, dM2, dM3, and dM4 stars. The differences between the behaviors of R'_{HK} (Figure 15) and L_X/L_{bol} (Figure 16) are significant. For dK4, dK6, and dM2 stars, L_X/L_{bol} rises slowly as R_0 decreases for the slow rotators ($\log(R_0) = 0$ to -1.0), and suddenly rises abruptly for the rapid rotators ($\log(R_0) < -1.0$). For the fast rotators ($\log(R_0) < -1.5$), L_X/L_{bol} seems to saturate at a level of about $10^{-3.0}$–$10^{-2.5}$. Patten & Simon (1996) also observed a similar behavior among their samples of stars in young clusters (IC 2391, α Persei, Pleiades, Hyades, and main-sequence stars in the field). They also observed a saturation at $L_X/L_{bol} \sim 10^{-3.0}$ for $\log(R_0) < -0.6$. On the other hand, they did not observe a plateau-like of behavior from $-3.0 < \log(R_0) < -1.3$ such as our dM2, dM3, and dM4 star data display in Figure 16. Instead they observe a strong rise in L_X/L_{bol} from $10^{-6.5}$to $10^{-3.0}$, more like the behavior of our data from $-1.3 < \log(R_0) < 0.3$ in Figure 16. Overall, our impression is that all stars in our five sub-samples follow a more or less similar correlation and show evidence for saturation for $\log(R_0) < -1.3$.

We should emphasize that our L_X data (taken from Hunsch et al. 1999) are severely biased toward the most active stars because of the limited sensitivity of *ROSAT*. Therefore, our samples of measures for the least active stars ($\log R_0 > -1.3$) are inevitably biased in a negative sense, and may not be dependable when we calculate the means of L_X/L_{bol} as a function of R_0.

3.11. Comparison and Contrast between Chromospheric and Coronal Heating Rates

In order to facilitate comparison of Figure 15 (lower panel; chromosphere) and Figure 16 (corona), we use similar notation for the lines that illustrate average values of the quantities at different spectral sub-types. Thus, in Figure 15 (lower), the dM3/dM4 stars (dotted line) lie lowest in the figure, whereas in Figure 16, the same stars lie at about the same levels as other spectral sub-types in the figure. For purposes of the present discussion, let us suppose that dM3 and dM4 stars may be labelled as at, or later than, the TTCC; we refer to these stars by the shorthand notation TTCC+. Stars at spectral types dM2 and earlier are referred to as TTCC-. In terms of this notation, our results indicate that, in terms of the chromosphere, TTCC+ stars are definitely weaker emitters than TTCC- stars (see Figure 14 lower panel). On the other hand, in terms of the corona, TTCC+ stars have similar emissions to those from TTCC- stars.

Thus, when we compare stars on different sides of the TTCC, the trend in coronal activity does not behave in the same way as the trend in chromospheric activity.

In order to explore this difference between activity at the chromospheric and coronal levels of M dwarf atmospheres, we turn now to investigate how L_X varies as a function of L_{HK}, and also as a function of spectral type.

3.11.1. L_X as a Function of L_{HK}

In a previous study, Schrijver et al. (1992) reported on the inter-relation between L_X and L_{HK} with nearly simultaneous observations of a sample of 26 F5–K3 main-sequence stars. Schrijver et al. (1992) obtained a good correlation over three orders of magnitude in L_{HK} and over four orders of magnitude in L_X. They found that L_X increased faster than L_{HK}: $L_X \propto L_{HK}^{1.50\pm0.20}$. In the present study, we compiled L_{HK} and L_X for our five different spectral subtypes. We find that the LSF to our samples give:

$$L_X = 4.57\ 10^{-16}\ L_{HK}^{1.54\pm0.29}\ \text{erg s}^{-1} \quad (32)$$

for our dK4 stars,

$$L_X = 7.94\ 10^{-17}\ L_{HK}^{1.57\pm0.21}\ \text{erg s}^{-1} \quad (33)$$

for our dK6 stars,

$$L_X = 1.00\ 10^{-15}\ L_{HK}^{1.57\pm0.17}\ \text{erg s}^{-1} \quad (34)$$

for our dM2 stars,

$$L_X = 7.94\ 10^{-20}\ L_{HK}^{1.74\pm0.11}\ \text{erg s}^{-1} \quad (35)$$

for our dM3 stars, and

$$L_X = 2.51\ 10^{-9}\ L_{HK}^{1.37\pm0.12}\ \text{erg s}^{-1} \quad (36)$$

for our dM4 stars.

The correlations are in all cases highly significant (see Table 1). The only exception occurs in the dK6 stars: this is because in this sample we have only few high-activity stars. Since the slope for dK6 stars is the same as for dK4 and dM2 stars, we believe the dK6 correlation is relevant for comparison to other sample correlations. Perhaps the smaller range of L_X values among dK6 stars also contributes to low significance. In Figure 17, we show the L_X versus L_{HK} correlations we found for our dK6, dM3, and dM4 stellar samples.

Including late-K and M dwarfs of all five sub-types, we find an average slope of 1.56 in our $\log(L_X)-\log(L_{HK})$ relationships. This is essentially identical to the value reported by Schrijver et al. (1992) for F5–K3 stars. Therefore, the same slope seems to prevail for all main-sequence stars from F5 to M4. This result emphasizes that, in low mass stars, it is a general result that the coronal emission grows faster than the chromospheric emission, from low-activity stars to high-activity stars. It is interesting to note that, when investigating *IUE* spectra of F to K type stars, Ayres et al. (1981) found also a power law slope of about 1.5 between the 10^5 K line fluxes and the Mg II line fluxes. However, in their correlation between the soft X-rays and Mg II fluxes, they found a larger slope.

However, what is more striking than the similarity in gradients found for these correlations, is the multiplicative coefficients in the correlations. We find that this factor changes from 4.47×10^{-16} for dK4 stars to 2.51×10^{-9} for dM4 stars. This large difference indicates that the empirical correlations differ greatly from one spectral sub-type to another even if the gradients are comparable. To illustrate this, we plot the LSF of L_X versus L_{HK} in Figure 18 for our five spectral sub-types. In all cases, it is apparent that the correlations have slopes that do not differ greatly. But the absolute values of fluxes from the chromospheres differ greatly. E.g., dK4 and dK6 stars have L_{HK} values mainly in the range $10^{27.5-29.5}$ erg s^{-1}, whereas the chromospheres of dM4 stars emit mainly in a much lower range, $10^{25-27.5}$ erg s^{-1}. On the other hand, emissions from the *coronae* of dK4 and dM4 stars overlap in the range $10^{27.5-28}$ erg s^{-1}.

As a result, at any given chromospheric emission level, the coronal emission strongly increases as we consider later spectral sub-types. E.g., for a chromospheric Ca II luminosity of $10^{27.5}$ erg s^{-1}, the X-ray luminosity increases by a factor of at least 110 between dK4 and dM4. Therefore, in the case of M dwarfs, the situation is quite different from that of earlier F, G, and K spectral types (e.g., Schrijver et al. 1992): stars from F to G to K all follow a common correlation between L_X and L_{HK}. In a similar vein, the large differences we observe among M dwarfs explains the large scatter observed in the L_X–L_{HK} correlation reported by Panagi & Mathioudakis (1993) for K and M dwarfs.

It is natural to inquire at this point, what makes M dwarfs so different from F-G-K dwarfs as regards the ratio of coronal to chromospheric emission? One possibility has been suggested by Mullan (1984). Coronal heating depends ultimately on tapping into the reservoir of mechanical energy associated with convective motions. In the context of electrodynamic coupling, the efficiency with which energy contained in that reservoir can be conveyed to the corona depends on two timescales, τ_c for convection, and τ_A for the coronal loops in which the energy is to be deposited. In the Sun, these timescales differ by factors of order 100. This large difference explains why the coronal energy flux from the Sun amounts to only 1% or less of the mechanical energy flux in convection. But Mullan (1984) predicted that, as one goes down the main sequence, there could come a point where the two timescales τ_c and τ_A could be comparable. This would occur by reduction in τ_c due to smaller convection cells, and increases in τ_A due to longer coronal loops. By making some assumptions, the prediction was made that $\tau_c \approx \tau_A$ would occur among stars with $T_{eff} \approx 3400$ K (see Mullan 1984: Section VI). What spectral type does this correspond to? According to Rajpurohit et al. (2013), the corresponding *I*–*J* color is 1.2–1.3, and the spectral type is M3. Moreover, $I-J = 1.2$ corresponds to $V-I$ color $= 2.2$, which is also the color at which coronal loops become longer (Mullan et al. 2006).

At the spectral type where $\tau_c \approx \tau_A$, the coronal loops would reach a resonance in their efficiency to tap into the convective reservoir. As a result, the efficiency of coronal heating in dM3 stars would be larger than in the Sun by 80–170. This range overlaps with the excess by factors of order 110 reported in Figure 18 above. Because a resonant process is at work in this model, the increase in coronal heating efficiency is expected to build up in spectral types as these approach closer to the resonance, i.e., approaching M3. Thus, the full increase by factors of 80–170 should be realized at M3, but smaller enhancements are expected at (say) M2, K6, and K4.

It is important to note that the electrodynamic resonance works only for the corona: there is no analogous process occurring in the chromosphere. Heating of the chromosphere, whether in an F star or an M star, continues to rely on localized dissipation of acoustic waves (for the "basal" component; Mullan & Cheng 1993) and on localized dissipation of currents, via the conductivity tensor, in a partially ionized medium (for the "magnetic" contribution; e.g., Kazeminezhad & Goodman 2006).

Even if the resonant model (Mullan 1984) turns out to be incorrect, at least the empirical results explain the L_X/L_{bol}–R_0 relationships reported above. We can now interpret the L_X/L_{bol}–R_0 relationships (in Figure 16) vis-a-vis the R'_{HK}–R_0 relationships (in Figure 15). Indeed, in late-K and M dwarfs, the 110-fold increase in X-ray coronal emission from spectral sub-types K4 and M4 compensates for the 90-fold decrease in dynamo/chromospheric efficiency from the same spectral types. As a result, in Figure 16, the M dwarfs have about the same L_X/L_{bol} values as the dK4 and dK6 stars, whereas in Figure 15, we found a drop-off for dM2 stars of about a factor of 10 as regards the chromospheric heating. Note, however, that in Figure 16, there is some convergence in L_X/L_{bol} for $R_0 < -1.3$ for all spectral types.

This discussion may help us to understand why Mullan & MacDonald (2001) failed to identify any signature of the TTCC in L_X/L_{bol} data: their failure may result from one aspect of coronal properties in M dwarfs. As a result of these properties, and their variation with spectral type in the vicinity of an electrodynamic resonance that (perhaps coincidentally) overlaps with the TTCC, the coronal ratio L_X/L_{bol} is not really suited for diagnosing the changing properties of the dynamo mechanisms before and at the TTCC. In view of the data presented in the present paper, we are now disposed to believe that the chromospheric emission (e.g., the Ca II luminosity) is better suited to respond to a signature of the TTCC.

3.12. The RACs and the Mean Rotation Periods

Can the properties of the RACs discussed above explain the mean $P/\sin i$ values obtained by HM for stars ranging in spectral sub-type from dK4 to dM4 stars? In particular, can they help in understanding the HM results of unexpectedly long rotation periods for dM3 stars? To answer this, we note that the mean $P/\sin i$ values of the slow rotators tend to decrease toward later spectral types. As a matter of fact, this trend is reproduced in the lower end of the RACs (Figure 14). Therefore, the decrease in the mean $P/\sin i$ at later spectral types could be due to the fact that the dynamo mechanisms

become inefficient at a rotation period that decreases toward the later spectral type (Figure 14). However, this is not completely the case for the dM3 RAC, which extends to somewhat longer periods than the dM2 RAC. Globally, the dM3 RAC is shifted toward longer periods with respect to the dM2 RAC, such that the mean $P/\sin i$ for dM3 stars is longer than for dM2 stars (as mentioned by HM). For dM4 stars, the whole of the RAC is shifted toward shorter rotation periods compared to dM3 stars. This explains why the mean $P/\sin i$ for dM4 stars is clearly smaller than that for dM3 stars. In fact, the dynamo mechanism in dM4 stars apparently becomes so inefficient at long periods that our sample contains not a single dM4 star with $P/\sin i$ longer than 10 days (see Figure 14). This can be contrasted with the much longer $P/\sin i$ values for dM3 stars: as large as 30 days (see Figure 8). Our discovery in the present paper that the level of chromospheric emission in dM4 stars is definitely smaller than in dM3 stars (suggesting that dynamo action in dM4 stars is less effective than in dM3 stars) could explain why the mean $P/\sin i$ is much shorter at dM4 than at dM3: dM4 stars are not as good at generating magnetic fields and, as a result, they do not have access to as good a "magnetic brake" as dM3 stars. The dM4 stars just keep on spinning fast, whereas the dM3 stars are braked. This might supplement (or replace) the hypothesis of long loop lengths (cf. HM) as the reason for slow rotation at dM3.

Also among dM2 stars, there are no stars rotating as slowly as the slowest dM3 stars (see Figure 5). So dM2 stars do not have access to as good a brake as dM3 stars. And yet, their dynamo effectiveness seems to be as high as, or higher than, the dM3 stars (see Figure 14 above). In this case, the onset of increased loop lengths at dM3 (cf. HM) would help to explain why dM3 stars have access to a better magnetic brake than dM2 stars.

For the fast rotators, we found (in HM) that the trend for the mean $P/\sin i$ is to become, in general, shorter as the spectral type becomes later, except at sub-type dM3 where the mean period is found to be significantly larger. The minima of the RACs show the opposite trend, i.e., the minimum $P/\sin i$ decreases with increasing spectral type. However, only very few active stars are at the extremes of the RACs: most active stars lie at longer periods. In the case of dM3 and dM4 stars, most active stars lie in the upper part of the rising slope of the RAC (see Figures 8 and 12). We also refer to Figures 3 and 5 for dK6 and dM2 stars, respectively. Therefore, the trend observed in the active stars can be interpreted by the RACs only if one considers their locations on these curves. Nevertheless, we note again that the upper end of the RAC for dM3 stars (in its rising part) is shifted again toward periods that are clearly longer than those for dM2 and dM4 stars. This again explains at least partly the abnormally large mean $P/\sin i$ of the active dM3 stars (see HM).

In summary, we find that the properties of the RACs can explain at least partly the observed trends in the mean $P/\sin i$ and also the abnormally long $P/\sin i$ values reported for dM3 stars by HM. However, this does not exclude another explanation, possibly involving a change in loop lengths (HM), which might also contribute to the unusual rise in the mean $P/\sin i$ at dM3.

4. Comparison with Other Studies of Rotation and Activity

West & Basri (2009) investigated the rotation and activity in H_α in a sample of 14 late-type M dwarfs (M6–M7). They found that many of these objects are rotating relatively fast ($>3.5\ \mathrm{km\ s^{-1}}$) but also have H_α in absorption. These rotational velocities imply rather short rotation periods for these small objects. This confirms our observed trend (see HM), that in general among late type dwarfs, rotation periods diminish with increasing spectral type. West & Basri (2009) also derived an empirical relationship between L_{H_α}/L_{bol} and $v\sin i$ from a compilation of data: they found that L_{H_α}/L_{bol} increases typically by two orders of magnitude for a change in $v\sin i$ of only $5\ \mathrm{km\ s^{-1}}$. This implies a steep gradient in the RAC. Although our spectral range does not go to spectral subtypes that are as late as those of West and Basri, our results are not inconsistent with theirs in the sense that that the steepest slope we have found for the RAC occurs among the latest spectral type in our sample (dM4, see Table 1), which is closest to the spectral types of the West–Basri sample.

Browning et al. (2010) analyzed the rotational broadening and activity in the Ca II lines for a sample of 123 M dwarfs. Unfortunately, because of limitations on their spectral resolution, they could measure $v\sin i$ for only seven stars, namely, those in which the projected rotational speeds were $>2.5\ \mathrm{km\ s^{-1}}$. They found that the rotation was detected mostly in stars later than M3 rather than in the range M0–M2.5. This is also consistent with our findings. They also found, in agreement with our results, that there is a "gap" in the measures of $L_{Ca\ II}/L_{bol}$ between the active stellar group and the low-activity stellar group (see Figure 11 above). They found a rough relationship between $L_{Ca\ II}/L_{bol}$ and $v\sin i$. However, most of their measures lie in the saturated regime, whereas in the present work, we have chosen to perform our RAC analyses on stars that lie in the unsaturated regime (so that we may examine stars that probably have dynamos also in the unsaturated regime).

Wright et al. (2011) reported on L_X/L_{bol} as a function of R_0 for a sample of (824) stars, which is significantly larger than we have analyzed here: the Wright et al. sample is three times larger than the number we used for chromospheric RACs, and about 10 times larger than the number of stars we used for the coronal RACs (Figure 16). However, the sample of Wright et al. extends over a much broader range of spectral types than we have studied here, from spectral type F to M5. They found a correlation between L_X/L_{bol} and R_0 although there is a significant scatter among the data. Their results reveal a saturated regime and an unsaturated regime, with a break at $\log(R_0) \approx -0.1$. The saturation value of L_X/L_{bol} was found to be at a log value of ~ -3. In the non-saturated regime the power law fit between $\log(L_X/L_{bol})$ and $\log(P)$ was found to have a slope of -2.18 ± 0.16. If the unsaturated (coronal) stars in their sample are analogous to our low-activity (chromospheric) stars, then their coronal slope (-2.2) is much steeper than what we found for the chromospheric slope (-0.8) (Table 1). The increase in steepness of the coronal RAC relative to the chromospheric slope (by an amount of about 1.4 in the slope) is reminiscent of our results in Section 3.11, Equations (32)–(36) where the slopes of L_X are steeper than the slope of L_{HK} by values, which (within errors) also overlap with 1.4 (except for dM2 stars).

Rebassa-Mansergas et al. (2013) studied a sample of white dwarf/M dwarf binaries from the Sloan Digital Sky Survey (SDSS DR7). They found indications that magnetic braking is less efficient beyond the fully convective boundary. This again agrees with our results that M4 dwarfs rotate faster than early M type dwarfs. They also studied the L_{H_α}/L_{bol}–$v\sin i$ relationship

and found mostly that stars with $v \sin i = 5$ km s^{-1} are all in the saturated regime. They also found a rapid increase in L_{H_α}/L_{bol} (by 2 orders of magnitude) as $v \sin i$ increases from 2 km s^{-1} to $v \sin i = 5$ km s^{-1}. This agrees with the similar diagram of West & Basri (2009), and again suggests a steep gradient in the RAC between low-activity and high-activity late-type M dwarfs (as we have found for our samples: see Table 1).

Robertson et al. (2013) investigated the magnetic activity level in H_α for a sample of 93 K5–M5 dwarfs. They found, in agreement with our results on the RACs, that early type M dwarfs (M0–M2) tend to have higher levels of activity than later type dwarfs and that, in general, $\log(L_{H_\alpha}/L_{bol})$ continuously decreases from −3.6 to −3.95 as the spectral sub-type increases from M0 to M5. This again agrees with our global finding that the surface fluxes in the Ca II lines decrease from K4 to M4.

Recently, an important paper has been published by West et al. (2015: W15) reporting on an analysis of chromospheric RACs in a sample of 238 M dwarfs, using H_α emission as a measure of chromospheric "activity." The sample stars had originally been selected as targets for planet searches, but W15 used the photometry to search for rotation periods P for the stars themselves. Photometric periods are not subject to the $\sin i$ uncertainty that affects the $P/\sin i$ we have obtained in the present study. In constructing their RAC, W15 identified 164 stars for which values of P and H_α data were available. The P values ranged from 0.3 to 100 days. The advantage of using photometry (over spectroscopy) to obtain P values is clear: there are no observational limits imposed by attempts to extract $v \sin i$ values from spectroscopic data. As a result, photometry allows W15 to determine rotational periods for slow rotators that are beyond the capabilities that we have used here. As a result, the W15 upper limit on P is several times longer than we have been able to report on in the present paper. In order to study variations of RAC with spectral type, W15 divided their stars into two groups: M1–M4 (64 stars, mainly M3 and M4), and M5–M8 (100 stars, mainly M5 and M6). Their plots of RAC (in their Figures 7 and 8) show that the M1–M4 stars have a negative slope: a LSF yields a slope of -0.19 ± 0.036. For the M5–M8 stars, the LSF gives a formal slope of essentially zero (-0.016 ± 0.050). These results suggest that since a finite (though small in absolute value) negative slope exists for the RAC in M1–M4 stars, rotation might well play a role in the chromospheric emission in M1–M4 stars. On the other hand, since the RAC slope was found to be essentially zero for M5–M8 stars, rotation may play little or no role in determining chromospheric emission in M5–M8 stars. At first sight, this result might be considered as evidence for the suggestion of Durney et al. (1993) that there might be a change in dynamo mode between M1–M4 and M5–M8. But we would like to suggest another possible interpretation, as follows.

In view of our own results for the RAC's in M4, M3, and M2 stars, we find it a matter of interest that the slope of the chromospheric RAC determined by W15 for M1–M4 stars (-0.19 ± 0.036) is much shallower than the values we have found. For our combined samples of dM+dMe stars, we have found slopes of −1.5 to −2.5 (see Table 1). And even when we confine attention to the slow rotators, we still find slopes for M2, M3, and M4 dwarfs (−0.89 to −0.93), which are clearly significantly steeper than W15 report for their M1–M4 sample. Our results indicate that chromospheric emission in M2–M4 stars in our samples exhibit much stronger sensitivity to rotation than W15 have reported for either of their samples. Is it possible that this dichotomy arises from selection effects? We note that the data of W15 include mainly "active" stars with H_α in emission, i.e., fast rotators, whereas our samples (especially the slow rotator samples) are biased toward slow rotators (H_α not in emission). Now, fast rotators are more likely to be in the saturated regime of the dynamo (see Section 1.1): in that regime, the RAC flattens out, and takes on a slope that is close to zero. In fact, in a discussion of the systematic differences between their M1–M4 sample and their M5–M8 sample, W15 point out that "At similar rotation periods, a much larger fraction of the late-type M dwarfs [M5–M8] are active" than is the case for the M1–M4 stars. Visual inspection of Figure 6 in W15 suggests that some 65% of their M1–M4 stars are labelled "active" while almost 90% of their M5–M8 stars are "active." This is consistent with the W15 statement that a "much larger fraction" of the M5–M8 stars are in the saturated regime. This leads us to wonder if the presence of saturated behavior is contributing to the (essentially) zero slope reported by W15 for M5–M8 stars. And even among the M1–M4 stars of W15, where the fraction of active stars is admittedly smaller than in the M5–M8 sample, that fraction is by no means small: some 65% of the M1–M4 stars are "active," and therefore may, lie in the saturated regime. Suppose that 65% of the M1–M4 stars in the W15 sample lie in the saturated regime (with a slope of zero), while the remaining 35% lie in the unsaturated regime, where the slope is finite (and negative), with a value of $-a$. Then the complete W15 sample of M1–M4 stars would have an RAC with an average slope a (W15) $= (0.65 \times 0) + (0.35 \times (-a))$. For slow rotators with spectral sub-types extending from dK4 to dM4, we have found that −a can take on values in the range from −0.6 to −0.9. This leads us to predict that a(W15) could range from −0.21 to −0.32. In fact, the empirical slope reported by W15 (-0.19 ± 0.036) contains, within a 3σ range, values of a (W15) extending from −0.08 to −0.30. This overlaps extensively with our predicted range of slopes.

Thus, it is possible that (i) the existence of a small but finite negative slope obtained by W15 for M1–M4 stars is due to the presence of a minority (35%) of stars in the unsaturated regime and (ii) the change in slope in going from M1–M4 to M5–M8 is due to the larger number of stars in the saturated regime among the M5–M8 sample. In order to test these possibilities, and in order to get a more definitive test of a change in dynamo mode at the TTCC, we suggest that it would be best to concentrate on stars in the unsaturated regime. So far, our own studies have not yet reached into M5–M8 stars: it will be a matter of great interest to determine if the W15 findings of significant change in RAC slope between M4 and M5 can be replicated using unsaturated stars.

5. Conclusion

In this section, we first (Section 5.1) summarize the approach we have adopted in order to study dynamos in low-mass stars. Then we go on (Sections 5.2–5.5) to describe how we have quantitatively characterized the observational data in terms of chromospheric observations. A discussion of coronal data follows (Section 5.6). In Section 5.7, we present the major conclusions of our study in terms of three hypotheses about dynamo action in low-mass dwarf stars. Last, we discuss evidence that has a bearing on crossing the TTCC (Section 5.8).

5.1. Dynamos: Saturated and Unsaturated

In order to account for the presence of active chromospheres and coronae in low-mass stars, dynamos are believed to be operative. Dynamos may rely on rotation plus turbulence, or on turbulence alone, to generate magnetic fields that then, as a result of "magnetic activity" (of some kind) lead to heating of the chromospheric and coronal gas. It is possible that different types of dynamos are at work in stars of different masses. In this paper, we bring together observational evidence to see if it is possible to identify signatures of different types of dynamos. Our study is based on the assumption that different types of dynamos are expected to lead to different answers to the following question: how does the amount of "activity" behave as a function of "rotation"? In order to address this, we need to compile data that provide us with quantitative measures of "activity" and "rotation."

An important aspect of the present paper is that we measure rotational speeds in stars that are rotating more slowly than has been reported in previous studies. Why are we interested in slow rotators? The reason has to do with the physics of dynamos: theoretical work suggests that rotational dynamo operation can saturate when the rotational speed reaches a certain limit. It seems to us that it would be difficult to extract information from a saturated dynamo, where the activity level no longer depends on how fast the star is rotating. For this reason, in this paper, we prefer to deal with dynamos in an unsaturated condition, where an increase in rotation leads to a clear and measurable increase in activity. This is what has driven us in the present paper to undertake a concerted effort toward identifying stars with the slowest possible rotations; to do this, we rely on spectroscopic data that were obtained with the highest possible resolution.

5.2. Data being Used in this Paper

Data have been compiled on chromospheric emission and (projected) rotational periods for a sample of 418 stars (Paper I) ranging in spectral sub-type from dK4 to dM4 (42 dK4, 118 dK6, 94 dM2, 81 dM3, 83 dM4).

The analysis that we apply to our data has the goal to derive a RAC for stars in each spectral sub-type, and then see if there are any systematic variations in the RACs as the spectral sub-type approaches the limit where main-sequence stars make a TTCC. The location of the TTCC is a matter of some dispute, possibly as early as dM2, possibly as late as dM4. Our choice of spectral sub-types is meant to overlap with TTCC.

5.3. Constructing RACs at Various Spectral Sub-types: Chromospheric Data

As a quantitative measure of "activity," we use the mean surface flux $F_{\rm Ca\ II}$ of emission in the Ca II H and K lines. As a quantitative measure of "rotation," we combine the projected rotational speeds $v \sin i$ with stellar radii to obtain a "projected rotation period" $P/\sin i$. We construct an RAC for stars in each spectral sub-type by plotting (in log-log format) the surface flux versus $P/\sin i$. The RACs that we have obtained for stars in each of our five spectral sub-types can be found in Figures 2, 3, 5, 8, and 12.

5.4. Chromospheric Data: the Slopes of the RACs

A general feature of many RACs is that as rotational periods become shorter, the Ca II surface flux becomes larger, up to a point. Beyond that point, shorter periods do not lead to any increase in Ca II flux: at these shortest periods, the RAC is probably "saturated." A key aspect of the present paper is that we discuss only the unsaturated part of the RAC. In this case, we obtain least squares fits of the RAC to a function of the form $F_{\rm Ca\ II} = b\,(P/\sin i)^a$. In a log-log plot, a is the slope of the RAC, and is a negative number. The coefficient b is a measure of the amplitude of chromospheric heating.

Numerical values of the slope a, which we have obtained from least squares fitting to our data for the various spectral sub-types, are shown in Figure 13. The different curves show the results we have obtained when we group our target stars in three different ways. (i) The curve that rises monotonically from lower left to upper right refers to the combined sample of all "unsaturated" stars, both those with low activity (dK, dM) and those with high activity (dKe, dMe). (ii) The curve that runs (almost) horizontally near the lower boundary of the figure refers to stars that are confined to the low-activity sub-samples (dK, dM). (iii) The "jagged" curve extending from middle left to lower right refers to stars that are confined to the high-activity sub-samples (dKe, dMe). The results in Figure 13 will guide our discussion of dynamos in the final sub-section.

5.5. Chromospheric Data: the Amplitude of Chromospheric Heating

As a second step in obtaining RACs, we consider, not the slopes, but the overall level of chromospheric heating in terms of the ratio of $L_{\rm HK}$ to $L_{\rm bol}$. Based on this ratio, we have obtained RACs based on a more physically relevant parameter (the Rossby number R_o). These RACs (see Figure 15) show that, at the longest rotation periods ($\log(R_o) = -1.2$) in our data set, chromospheric heating in dM3 stars is less effective by a factor of about 20 than in dK4 stars. Our results suggest that the chromospheric heating efficiency in dM4 stars is less effective by a factor of about 100 than in F-G-K type stars. We also observe a progressive decline in the location of the RACs as we go from dK4 to dM4: dK6 stars lie slightly below (a factor of 3) the RAC of F, G, and K type stars, while dM2 stars lie a factor of 10 below the RAC of F, G, and K type stars. The data point to a conclusion that we consider reliable: the efficiency of chromospheric heating decreases progressively between dK4 and dM4. The amplitude of the overall decrease is 20–90. This also implies that the overall efficiency of the dynamo mechanisms also decreases by the same factors when moving from K4 to M4 dwarfs.

5.6. Coronal Data

Turning now to the RAC associated with coronal emission, we find a very different behavior from the chromospheric data (Figure 16). The coronal emission $L_{\rm X}/L_{\rm bol}$ does not decrease significantly as we go from dK4 to dM4. The lack of decrease is especially marked when we compare the coronal emission to the chromospheric emission (see Figure 18): for a given value of $L_{\rm HK}$ (say $10^{27.5}$ erg s^{-1}), the value of $L_{\rm X}$ in dM4 stars is larger by a factor of order 100 compared to $L_{\rm X}$ in dK4/dK6 stars. Thus, while the chromospheric heating efficiency is decreasing as we go from dK4 to dM4 (by a factor of

up to 100), the coronal heating efficiency is simultaneously increasing (by a factor of 100 or so).

In terms of a dynamo interpretation, this raises the question: which part of a stellar atmosphere should we study in order to obtain more reliable information about dynamo efficiency in M dwarfs, the chromosphere or the corona? The behaviors are so different that it is not clear that the same information about the dynamo will emerge from both data sets. We have argued (Section 3.11) that it may be preferable to concentrate on the chromosphere.

In view of this, we now present some conclusions that, in our opinion, help to bring order to the chromospheric data that have been analyzed in the present paper.

5.7. Hypotheses about Two Distinct Dynamos in Low-mass Stars

Inspection of Figure 13 leads us to offer the following hypotheses.

(i) In the case of low-activity stars, we see that the RAC slope *a* is essentially unchanged as we go from dK4 to dM4. To the extent that a particular RAC slope is associated with a particular dynamo mechanism, our results indicate that low-activity stars have essentially the same dynamo at work in stars that range in spectral sub-type from dK4 to dM4. Such a dynamo must have something to do with a physical property that is present in all low mass stars from dK4 to dM4, i.e., on both sides of the TTCC. What property is common to all such stars? The answer is: all of them have a deep convective envelope in which turbulence provides a ready supply of energy to drive a distributed dynamo (DD), i.e., a dynamo that could be described by either an α^2 model or an $\alpha^2\Omega$ model. This leads us to Hypothesis (A): low-activity stars from dK4 to dM4 may be dominated by a turbulent (DD) dynamo.

(ii) In the case of the RAC for high-activity stars, the aspect of Figure 13 that is most likely to catch the eye is probably the "jagged" behavior at early spectral types. But we would like to draw attention first to a different aspect of the RACs: namely, the values of the slopes a at the latest spectral types (dM3e and dM4e). In these cases, our results indicate that the RAC slopes for high-activity stars are essentially the same as for the low-activity stars. Once again relying on a putative association between an RAC slope and a dynamo mechanism, these results suggest that, at spectral types dM3 and dM4, the dynamo mechanism in low- and high-activity stars are actually the same. It has already been suggested (see (i)) that a DD is at work in all low-activity stars. This leads us to Hypothesis (B): in the high-activity stars at the latest sub-types in our samples (dM3e and dM4e), a DD is at work. This is not a surprising conclusion: dM3e and dM4e stars are completely convective (CC), so they also have access to DD operation in the form of either an α^2 dynamo model or an α^2–Ω dynamo model.

(iii) Moving now to high-activity stars at earlier spectral types (dK4e, dK6e, and dM2e), we see in Figure 13 that the RAC slopes are very different from the slopes of the low-activity stars. This suggests that high-activity stars in the range dK4e–dM2e have access to a different kind of dynamo from the type (DD) that may dominate in low-activity stars. What might give rise to a non-DD type of dynamo in stars with spectral types in the range dK4–dM2? The answer is surely related to the fact that such stars have interfaces between the outer convective envelope and an inner radiative core. This leads to Hypothesis (C): in high-activity stars at the earliest spectral types in our samples, an interface dynamo (ID) is at work. It seems probable that such a dynamo could be described by an α–Ω dynamo model. To be sure, dK4e–dM2e stars also have deep convective envelopes: therefore a DD is probably also at work. But the clear difference in RAC slopes between low-activity stars in the range dK4–dM2 and high-activity stars in the range dK4e–dM2e indicates that the DD (with its shallow RAC slope) is not playing a dominant role in dK4e–dM2e stars.

(iv) If our hypotheses have any validity, we can conclude that the primary quantitative difference between ID and DD is this: the RAC slopes are steeper (by up to 1.5 units) among the ID stars than the DD stars. Thus, the ID stars are much more sensitive to rotation than the DD stars. Specifically, if we compare two stars that differ in rotation by a factor of (say) 10, two stars where ID operates will differ in activity level by a factor that is 30 times larger than the difference in activity level of two stars where DD operates.

(v) The conclusion in item (iv) is reminiscent of a suggestion that was made by Durney et al. (1993): the RAC in a star with ID should depend sensitively on period, but the RAC in a star with DD should not. The results in Figure 13 are at least partially consistent with Durney et al.: ID stars (as we identify them) are definitely more sensitive to rotation than DD stars (as we identify them). Admittedly, we have not found that the DD has zero slope for its RAC: but we have found that the slope is at least smaller than in the ID stars.

The fact that the DD stars have an RAC with a non-zero slope suggests that rotation Ω does have some effect on the activity level in these stars. In terms of the two options that we have proposed in Hypotheses A and B above, it might be preferable to conclude that the dominant dynamo model in DD stars may be the α^2–Ω model.

Finally, we make a point about the overall methodology that has been ultimately responsible for this paper. The opening sentence in item (i) above, which provides a start to our three hypotheses, would not have been possible if we did not have access to a large sample of low-activity stars. Such stars are slow rotators. Therefore, if the lead author of this study (E.R.H.) had not paid attention to extracting the lowest possible values of $v/\sin i$ (of order $1\,\mathrm{km\,s^{-1}}$) in as many stars as possible, our sample of low-activity stars might have been so small as to prevent us from drawing statistically significant conclusions.

5.8. Any Evidence for Crossing the TTCC?

The theoretical concept that main-sequence stars undergo a TTCC at a particular mass (in the vicinity of spectral types M2–M4) has been in the literature for 50 years or more. Nevertheless, the search for an empirical signature that might support this concept has yielded no definitive evidence. For example, Mullan & MacDonald (2001) sought such evidence in X-ray data, but were unable to identify any signature of the TTCC. Also, in our own coronal data (Figure 16), we see no definitive sign of a transition. Neither could we find evidence for the TTCC in the RACs of chromospheric data when we combined low- and high-activity stars (Figure 13), monotonically rising line from lower left to upper right. Nor could we find any evidence of TTCC when we confined our attention to the chromospheric RACs of low-activity stars (lowest lying line in Figure 13.

However, in one particular sample, our study has led to what we believe is a potentially valuable signature. Specifically, in our sample of high-activity stars between dK4e and dM4e, the slopes of the chromospheric RAC (Figure 13, "jagged" line) consists of two distinct regimes. In one regime, the slopes overlap with the (shallow) slopes of low-activity stars. In the other regime, the slopes are found to be much steeper. We interpret the transition between the two regimes as evidence for a transition between dynamo modes. The transition occurs between dM2e and dM3e. We suggest that this cross-over from steep to shallow RAC slopes may provide empirical evidence that the TTCC has been crossed.

We have shown how empirical information about rotation and chromospheric emission may contribute to understanding some aspects of dynamo mechanisms in cool dwarfs. Data for M dwarfs with spectral types later than M4, and also for L and T dwarfs, would be of great interest to complete our view on the dynamo mechanisms in low-mass stars. For example, is there any evidence that the efficiency of coronal heating actually decreases after we pass though the electrodynamic resonance that is expected to occur around dM3–dM4? It would also be of interest to investigate the variations of rotational and chromospheric properties by using finer grained samples of stars near the TTCC, i.e., using samples of stars all of which are confined to spectral types of dM2.5, dM3.5, and dM4.5 stars. This could contribute to better understanding of the behavior of possible changes in the dynamo mechanism(s) at the TTCC.

This research has made use of the SIMBAD database, operated at CDS, Strasbourg, France. D.J.M. is supported in part by the NASA Space Grant program. This study was based on data obtained from the ESO Science Archive Facility and the Observatoire de Haute Provence SOPHIE database. This research made use of Astropy,[9] a community-developed core Python package for Astronomy. We also used the tutorial developed by Paletou & Zolotukhin (2014).[10] This research was achieved using the POLLUX database (http://pollux.graal.univ-montp2.fr) operated at LUPM (Université Montpellier-CNRS, France) with the support of the PNPS and INSU. This research has made use of the VizieR catalog access tool, CDS, Strasbourg, France. The original description of the VizieR service was published in A&AS 143, 23.

Appendix
Quadratic Heteroscedastic Regression Models

This appendix is devoted to classical mathematical results on stochastic linear regression models. Our purpose is to show how to better take into account the measurement errors of $P/\sin i$ in order to explain the variability of Ca II surfaces fluxes. In the previous literature, only linear or quadratic homoscedastic LSF were investigated in order to explain this variability. Our strategy is slightly different as we propose to make use of linear or quadratic heteroscedastic LSF in order to better explain this variability.

More precisely, consider one of our five groups of dK4, dK6, dM2, dM3, or dM4 stars, for example dM2. Let $n > 3$ be the total number of the dM2 stars under study. For each dM2 star, denote by x_k the $\log(P/\sin i)$ associated measure and by $\sigma_k > 0$ the measurement error of $\log(P/\sin i)$. Moreover, let Y_k be the log(Ca II Flux) measure of this dM2 star. Then, we shall deal with the linear or quadratic heteroscedastic regression models, respectively given, for $k = 1, \ldots, n$, by

$$Y_k = a + bx_k + \sigma_k \varepsilon_k, \tag{37}$$

and

$$Y_k = a + bx_k + cx_k^2 + \sigma_k \varepsilon_k, \tag{38}$$

where a, b, and c are unknown parameters and the random noise (ε_k) is a standard Gaussian white noise with mean zero and unknown variance τ^2. The important point is the crucial role played by the error term σ_k. The variance of the additive noise clearly depends on the explanatory variable x_k as it is given by $\sigma_k^2\tau^2$ where σ_k is the measurement error associated with x_k. We shall only focus our attention on the quadratic heteroscedastic regression model given by (38) inasmuch as the linear regression model (37) is a particular case of (38).

The quadratic heteroscedastic regression model (38) can be rewritten into the matrix form

$$Y = X\theta + \Gamma^{1/2}\varepsilon, \tag{39}$$

where the vector of observations Y, the vector of unknown parameters θ, and the vector containing the random noises ε, are respectively given by

$$Y = \begin{pmatrix} Y_1 \\ \vdots \\ Y_n \end{pmatrix}, \qquad \theta = \begin{pmatrix} a \\ b \\ c \end{pmatrix}, \qquad \varepsilon = \begin{pmatrix} \varepsilon_1 \\ \vdots \\ \varepsilon_n \end{pmatrix}.$$

In addition, the heteroscedastic matrix $\Gamma = \mathrm{diag}(\sigma_1^2, \sigma_2^2, \cdots, \sigma_n^2)$ and the design matrix X is given by

$$X = \begin{pmatrix} 1 & x_1 & x_1^2 \\ 1 & x_2 & x_2^2 \\ \vdots & \vdots & \vdots \\ 1 & x_n & x_n^2 \end{pmatrix}.$$

On the one hand, the least squares estimator (LSE) of θ is the value $\tilde{\theta}$ that minimizes the strictly convex function $\widetilde{\Delta}(\theta) = \|Y - X\theta\|^2$. Straightforward calculation leads to

$$\tilde{\theta} = (X^tX)^{-1}X^tY.$$

However, this estimator does not taken into account the heteroscedasticity of model (39). On the other hand, the weighted least squares estimator (WLSE) of θ is the value $\hat{\theta}$, which minimizes the strictly convex function

$$\widehat{\Delta}(\theta) = (Y - X\theta)^t\Gamma^{-1}(Y - X\theta).$$

It is not hard to see that

$$\hat{\theta} = (X^t\Gamma^{-1}X)^{-1}X^t\Gamma^{-1}Y. \tag{40}$$

We immediately deduce from (39) and (40) that

$$\hat{\theta} = \theta + (X^t\Gamma^{-1}X)^{-1}X^t\Gamma^{-1/2}\varepsilon.$$

Consequently, as ε is a n-dimensional Gaussian vector $\mathcal{N}(0, \tau^2 I)$ where I stands for the identity matrix of order n, we

[9] http://www.astropy.org/ and http://astroquery.readthedocs.org/en/latest/.
[10] http://www.astropy.org/

obtain that $\hat{\theta}$ is a three-dimensional Gaussian vector,

$$\hat{\theta} = \begin{pmatrix} \hat{a} \\ \hat{b} \\ \hat{c} \end{pmatrix} \sim \mathcal{N}(\theta, \tau^2 (X^t \Gamma^{-1} X)^{-1}). \quad (41)$$

Hereafter, the linear least squares fit (LSF) is the line

$$y = \hat{a} + \hat{b}x, \quad (42)$$

while the quadratic LSF is the curve

$$y = \hat{a} + \hat{b}x + \hat{c}x^2. \quad (43)$$

Furthermore, denote by H the hat matrix

$$H = X(X^t \Gamma^{-1} X)^{-1} X^t \Gamma^{-1} \quad \text{and} \quad L = I - H.$$

It follows from (39) to (40) that $\hat{Y} = HY = X\hat{\theta}$, which implies that HY has an $\mathcal{N}(X\theta, \tau^2 H\Gamma)$ distribution and $LY = Y - \hat{Y}$ has an $\mathcal{N}(0, \tau^2 L\Gamma)$ distribution. Hence, as $\mathrm{rank}(L) = n - 3$, we obtain that the sum of squared errors (SSE) has a chi-squared distribution,

$$\|\Gamma^{-1/2}(Y - \hat{Y})\|^2 \sim \tau^2 \chi^2 (n - 3). \quad (44)$$

The SSE is a way to evaluate the discrepancy between the data Y and its estimate $\hat{Y}$ and a small value of the SSE indicates a tight fit of our model to the data. Let us recall the celebrated decomposition of total sum of squares, which is in fact a direct application of Pythagoras's theorem

$$\|\Gamma^{-1/2} Y\|^2 = \|\Gamma^{-1/2}\hat{Y}\|^2 + \|\Gamma^{-1/2}(Y - \hat{Y})\|^2.$$

Finally, a natural estimator of the variance τ^2 is

$$\hat{\tau}^2 = \frac{\|\Gamma^{-1/2}(Y - \hat{Y})\|^2}{n - 3}. \quad (45)$$

It is not hard to see that the random vector $\hat{\theta}$ and $\hat{\tau}^2$ are independent. Consequently, we deduce from (41) that for any real number x,

$$(\hat{a} - a) + (\hat{b} - b)x + (\hat{c} - c)x^2 \sim \mathcal{N}(0, \tau^2 \xi(x))$$

where

$$\xi(x) = \begin{pmatrix} 1 \\ x \\ x^2 \end{pmatrix}^t (X^t \Gamma^{-1} X)^{-1} \begin{pmatrix} 1 \\ x \\ x^2 \end{pmatrix}.$$

Dividing on both sides by $\hat{\tau}$, the ratio has a Student distribution,

$$\frac{(\hat{a} - a) + (\hat{b} - b)x + (\hat{c} - c)x^2}{\hat{\tau}\sqrt{\xi(x)}} \sim t(n - 3). \quad (46)$$

References

Ayres, T. R., Marstad, N. C., & Linsky, J. L. 1981, ApJ, 247, 545
Baliunas, S. L., Donahue, R. A., Soon, W. H., et al. 1995, ApJ, 438, 269
Barnes, S. A. 2003, ApJ, 586, 464
Brandenburg, A., & Subramanian, K. 2005, PhR, 417, 1
Brown, B. P., Browning, M. K., Brun, A. S., Miesch, M. S., & Toomre, J. 2010, ApJ, 711, 424
Browning, M. K., Basri, G., Marcy, G. W., West, A. A., & Zhang, J. 2010, AJ, 139, 504
Browning, M. K., Weber, M. A., Chabrier, G., & Massey, A. P. 2016, ApJ, 818, 189
Chabrier, G., & Baraffe, I. 1997, A&A, 327, 1039
Chabrier, G., & Kuker, M. 2006, A&A, 446, 1027
Christian, D. J., & Mathioudakis, M. 2002, AJ, 123, 2796
Christian, D. J., Mathioudakis, M., Arias, T., Jardine, M., & Jess, D. B. 2011, ApJ, 738, 164
Cram, L. E., & Mullan, D. J. 1979, ApJ, 234, 579
de Laverny, P., Recio-Blanco, A., Worley, C. C., & Plez, B. 2012, A&A, 544, A126
Delfosse, X., Forveille, T., Perrier, C., & Mayor, M. 1998, A&A, 331, 581
Dobler, W., Stix, M., & Brandenburg, A. 2006, ApJ, 638, 336
Donati, J.-F., Morin, J., Petit, P., et al. 2008, MNRAS, 390, 545
Dorman, B., Nelson, L. A., & Chau, W. Y. 1989, ApJ, 342, 1003
Duncan, D. K., Vaughan, A. H., Wilson, O. C., et al. 1991, ApJS, 76, 383
Durney, B. R., De Young, D. S., & Roxburgh, I. W. 1993, SoPh, 145, 207
Fawzy, D., Ulmschneider, P., Stepien, K., Musielak, Z. E., & Rammacher, W. 2002, A&A, 386, 983
Feiden, G. A., & Dotter, A. 2013, ApJ, 765, 86
Fekel, F. C. 1997, PASP, 109, 514
Fleming, T. A., & Giampapa, M. S. 1989, ApJ, 346, 299
Fleming, T. A., Giampapa, M. S., Schmitt, J., & Bookbinder, J. A. 1993, ApJ, 410, 387
Giampapa, M. S., & Liebert, J. 1986, AJ, 305, 784
Giampapa, M. S., Cram, L. E., & Wild, W. J. 1989, ApJ, 345, 536
Gizis, J. E., Reid, I. N., & Hawley, S. L. 2002, AJ, 123, 3356
Hawley, S. L., Gizis, J. E., & Reid, I. N. 1996, AJ, 112, 2799
Hempelmann, A., Schmitt, J. H. M. M., Schultz, M., Rudiger, G., & Stepien, K. 1995, A&A, 294, 515
Herbst, W., & Miller, J. R. 1989, AJ, 97, 891
Houdebine, E. R. 1992, IrAJ, 20, 213
Houdebine, E. R. 2008, MNRAS, 390, 1081
Houdebine, E. R. 2009a, MNRAS, 400, 238
Houdebine, E. R. 2009b, MNRAS, 397, 2133
Houdebine, E. R. 2010a, MNRAS, 407, 1657
Houdebine, E. R. 2010b, MNRAS, 509, 65
Houdebine, E. R. 2011a, MNRAS, 416, 2233
Houdebine, E. R. 2011b, MNRAS, 411, 2259
Houdebine, E. R. 2012a, MNRAS, 421, 3180
Houdebine, E. R. 2012b, MNRAS, 421, 3189
Houdebine, E. R., & Doyle, G. J. 1994a, in Proc. ASP Conf. Ser. 64, Eigth Cambridge Workshop on Cool Stars, Stellar Systems and the Sun, ed. J. P. Caillault (San Fransisco, CA: ASP), 423
Houdebine, E. R., & Doyle, J. G. 1994b, A&A, 289, 169
Houdebine, E. R., & Doyle, J. G. 1994c, A&A, 289, 185
Houdebine, E. R., Doyle, J. G., & Koscielecki, M. 1995, A&A, 294, 773
Houdebine, E. R., & Stempels, H. C. 1997, A&A, 326, 1143
Houdebine, E. R., & Mullan, D. J. 2015, ApJ, 801, 106
Houdebine, E. R., Butler, C. J., Garcia-Alvarez, D., & Telting, J. 2012, MNRAS, 426, 1591
Houdebine, E. R., Mullan, D. J., Paletou, F., & Gebran, M. 2016, ApJ, 822, 97
Houdebine, E. R., Mullan, D. J., & Paletou, F. 2017, ApJ, submitted
Hunsch, M., Schmitt, J. H. M. M., Sterzik, M. F., & Voges, W. 1999, A&AS, 135, 319
Isaacson, H., & Fischer, D. 2010, ApJ, 725, 875
Jeffries, R. D., Totten, E. J., & James, D. J. 2000, MNRAS, 316, 950
Kamper, K. W., Kim, K. M., & Thomson, J. R. 1997, BaltA, 6, 111
Kazeminezhad, F., & Goodman, M. L. 2006, ApJS, 166, 613
Kenyon, S. J., & Hartmann, L. 1995, ApJS, 101, 117
Kim, Y.-C., & Demarque, P. 1996, ApJ, 457, 340
Kraft, R. P. 1967, ApJ, 150, 551
Krause, F., & Radler, K. H. 1980, Mean Field Electrodynamics and Dynamo Theory (Oxford: Pergamon)
Lawson, N., Strugarek, A., & Charbonneau, P. 2015, ApJ, 813, 95
Leggett, S. K. 1992, ApJS, 82, 351
Limber, D. N. 1958, ApJ, 127, 387
Mann, A. W., Feiden, G. A., Gaidos, E., Boyajian, T., & Von Braun, K. 2015, ApJ, 804, 64
Marcy, G. W., & Chen, G. H. 1992, ApJ, 390, 550
Marilli, E., Catalano, S., & Trigilio, C. 1986, A&A, 167, 297
Mamajek, E. E., & Hillebrand, L. A. 2008, ApJ, 687, 1264
Mohanty, S., & Basri, G. 2003, ApJ, 583, 451
Montesinos, B., Thomas, J. H., Ventura, P., & Mazzitelli, I. 2001, MNRAS, 326, 877
Morales, J. C., Ribas, I., & Jordi, C. 2008, A&A, 478, 507
Morin, J., Donati, J.-F., Petit, P., et al. 2008, MNRAS, 390, 567
Morin, J., Donati, J.-F., Petit, P., et al. 2010, MNRAS, 407, 2269
Mullan, D. J. 1984, ApJ, 282, 603

Mullan, D. J. 2009, Physics of the Sun: A First Course (Boca Raton, FL: CRC Press)
Mullan, D. J., & Cheng, Q. Q. 1993, ApJ, 412, 312
Mullan, D. J., & MacDonald, J. 2001, ApJ, 559, 353
Mullan, D. J., & MacDonald, J. 2003, ApJ, 598, 560
Mullan, D. J., Mathioudakis, M., Bloomfield, D. S., & Christian, D. J. 2006, ApJS, 164, 173
Mullan, D. J., Houdebine, E. R., & MacDonald, J. 2015, ApJL, 810, L18
Noyes, R. W., Hartmann, L. W., Baliunas, S. L., Duncan, D. K., & Vaughan, A. H. 1984, ApJ, 279, 763
Pace, G. 2013, A&A, 551, L8
Palacios, A., Gebran, M., Josselin, E., et al. 2010, A&A, 516, A13
Paletou, F., & Zolotukhin, I. 2014, arXiv:1408.7026
Pallavicini, R., Golub, L., Rosner, R., et al. 1981, ApJ, 248, 279
Panagi, P. M., & Mathioudakis, M. 1993, A&AS, 100, 343
Parker, E. N. 1955, ApJ, 122, 293
Parker, E. N. 1975, ApJ, 198, 205
Parker, E. N. 1979, Cosmical Magnetic Fields: Their Origin and Their Activity (Oxford: Clarendon Press)
Patten, B. M., & Simon, T. 1996, ApJS, 106, 489
Phan-Bao, N., Lim, J., Donati, J.-F., Johns-Krull, C. M., & Martín, E. L. 2009, ApJ, 704, 1721
Pizzolato, N., Maggio, A., Micela, G., Sciortino, S., & Ventura, P. 2003, A&A, 397, 147
Racine, E., Charbonneau, P., Ghizaru, G., Bouchat, A., & Smolarkiewicz, P. K. 2011, ApJ, 735, 46
Rajpurohit, A. S., Reylé, C., Allard, F., et al. 2013, A&A, 556, A15
Ramirez, I., & Melendez, J. 2005, ApJ, 626, 465
Rauscher, E., & Marcy, G. W. 2006, PASP, 118, 617
Rebassa-Mansergas, A., Schreiber, M. R., & Gansicke, B. T. 2013, MNRAS, 429, 3570
Reiners, A., Basri, G., & Browning, M. 2009, ApJ, 692, 538
Reiners, A., Joshi, N., & Goldman, B. 2012, AJ, 143, 93
Roberts, P. H., & Stix, M. 1972, A&A, 18, 453
Robertson, P., Endl, M., Cochran, W. D., & Dodson-Robinson, S. E. 2013, ApJ, 764, 3
Rodriguez-Lopez, C., MacDonald, J., Amado, P. J., Moya, A., & Mullan, D. J. 2014, MNRAS, 438, 2371
Rosner, R. 1980, in Cool Stars, Stellar Systems and the Sun, ed. A. K. Dupree (Cambridge: SAO), 389
Rutten, R. G. M. 1987, A&A, 177, 131
Rutten, R. G. M., Schrijver, C. J., Zwaan, C., Duncan, D. K., & Mewe, R. 1989, A&A, 219, 239
Rutten, R. G. M., Schrijver, C. J., Lemmens, A. F. P., & Zwaan, C. 1991, A&A, 252, 203
Schrijver, C. J. 1987, A&A, 172, 111
Schrijver, C. J., Coté, J., Zwaan, C., & Saar, S. H. 1989, ApJ, 337, 964
Schrijver, C. J., Dobson, A. K., & Radick, R. R. 1992, A&A, 258, 432
Skumanich, A., Smythe, C., & Frazier, E. N. 1975, ApJ, 200, 747
Soderblom, D. R. 1982, ApJ, 263, 239
Soderblom, D. R., Duncan, K. D., & Johnson, D. R. H. 1991, ApJ, 375, 722
Spada, F., Demarque, P., Kim, Y.-C., & Sills, A. 2013, ApJ, 776, 87
Stauffer, J. R., & Hartmann, L. W. 1986, ApJS, 61, 531
Stassun, K. G., Hebb, L., Covey, K., et al. (Cambridge: Cambridge Univ. Press) 2011, in ASP Conf. Ser. 448 16th Cambridge Workshop on Cool Stars, Stellar Systems, and the Sun, ed. C. M. Johns-Krull et al. (Cambridge: Cambridge Univ. Press), 505
Stefani, F., & Gerberth, G. 2003, PhRvE, 67, 027302
Stepień, K. 1989, A&A, 210, 273
Stepień, K. 1993, in Proc. IAU Symp. 157, The Cosmic Dynamo, ed. F. Krause, K. H. Radler, & R. Gunther (Cambridge: Cambridge Univ. Press), 141
Stepień, K. 1994, A&A, 292, 207
Strassmeier, K. G., Handler, G., Paunzen, E., & Rauth, M. 1994, A&A, 281, 855
Ulmschneider, P., & Musielak, Z. E. 2003, in ASP Conf. Ser. 286, Current Theoretical Models and High Resolution Solar Observations: Preparing for ATST, ed. A. A. Pevtsov & H. Uitenbroek (San Fransisco, CA: ASP), 363
Ulmschneider, P., Fawzy, D., Musielak, Z. E., & Stepien, K. 2005a, ApJL, 559, L167
Ulmschneider, P., Rammacher, W., Musielak, Z. E., & Kalkofen, W. 2005b, ApJL, 631, L155
Vaughan, A. H., Baliunas, S. L., Middelkoop, F., et al. 1981, ApJ, 250, 276
Vilhu, O. 1984, A&A, 133, 117
Vogt, S. S., Soderblom, D. R., & Penrod, G. D. 1983, ApJ, 269, 250
Walkowicz, L. M., & Hawley, S. L. 2009, AJ, 137, 3297
Ward-Duong, K., Patience, J., De Rosa, R. J., et al. 2015, MNRAS, 449, 2618
West, A. A., & Basri, G. 2009, ApJ, 693, 1289
West, A. A., Weisenburger, K. L., Irwin, J., et al. 2015, ApJ, 812, 3
Wilson, O. C. 1968, ApJ, 153, 221
Wright, C. O., Egan, M. P., Kraemer, K. E., & Price, S. D. 2003, AJ, 125, 359
Wright, N. J., Drake, J. J., Mamajek, E. E., & Henry, G. W. 2011, ApJ, 743, 48
Young, A., Skumanich, A., Stauffer, J. R., Harlan, E., & Bopp, B. W. 1989, ApJ, 344, 427